POLITECNICO DI TORINO

DAUIN - Dipartimento di Automatica e Informatica

Master's degree in Mechatronic Engineering

M.Sc. Thesis

Ad hoc tool for massive data analysis of photovoltaic generators: experimental validation and energy assessment of a high efficiency module

Supervisors:

Prof. Filippo Spertino
Prof. José Vicente Muñoz Díez
Prof. Slawomir Gulkowski
Ing. Gabriele Malgaroli

Candidate:

Matteo Alessio Magnetti

28th July 2020

"Scientists discover the world that exists;
engineers create the world that never was."
— Theodore von Karman

Acknowledgement

In questa pagina voglio ringraziare tutti quelli che mi hanno supportato durante la mia esperienza universitaria.

En primer lugar, quiero agradecer a mi Profesor José Vicente Muñoz Díez por el apoyo durante el desarrollo de este trabajo de fin de máster en la Escuela Politécnica Superior de la Universidad de Jaén. Un cordiale ringraziamento va al Professor Filippo Spertino, mio relatore presso il Politecnico di Torino, che mi ha proposto questo lavoro di tesi e mi ha guidato nella sua realizzazione. Un peculiare ringraziamento è d'obbligo per l'Ing. Gabriele Malgaroli che mi ha seguito e aiutato con estremo impegno in questi mesi. Finally, I would like to thank professor Slawomir Gulkowski from Politechnika Lubelska for his help in the analysis of the results.

Un particolare ringraziamento va ai miei genitori e ai miei zii che mi hanno supportato in questi anni di università. Grazie a loro, che mi hanno sostenuto moralmente ed economicamente, ho potuto portare a termine la mia carriera universitaria. Sono sicuro che darò loro una grande soddisfazione laureandomi.

Un altro ringraziamento va ai miei amici e amiche che in questi anni mi sono stati vicini e mi hanno aiutato. In particolare, Martina, che mi ha aiutato nella realizzazione del tool, Viktoria, which helped me identify errors and test the correct behavior of the tool, e Roberta, che mi ha aiutato a rileggere e correggere la grammatica inglese.

Uno speciale ringraziamento è per la mia fidanzata Angela che in questi mesi mi ha sopportato e mi ha aiutato a superare gli imprevisti che si sono presentati durante la stesura di questo lavoro di tesi.

Finalmente, quiero agradecer a España y a sus ciudadanos por darme una cálida bienvenida a este nuevo país. En particular a mis compañeros de piso Miguel, Pilar y Victoria que me acogieron cariñosamente.

Matteo Alessio

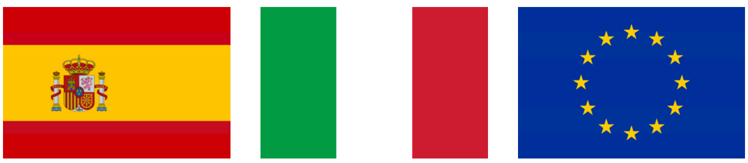

Abstract

The performance of photovoltaic generators can be described by an equivalent circuit. This thesis focuses on the experimental validation of an innovative technique to predict the circuit parameters in any operating condition. This work is divided in two activities: in the first part of the thesis, an ad hoc Graphical User interface (GUI) is developed in MATLAB ambient to perform a massive analysis of a wide dataset of experimental measurements. This analysis consists of four steps: the preprocessing of the dataset; the numerical extraction of the circuit parameters starting from experimental current-voltage (*I*-*V*) curves; the identification of equations to describe the parameters dependence with respect to irradiance and cell temperature; and the prediction of the produced photovoltaic energy during the experimental campaign using the previous equations or theoretical models. In the second part of the thesis, the GUI is applied to experimental data of a high efficiency Heterojunction with Intrinsic Thin layer (HIT) module with rated power of 240 W. The tool analyzes a wide dataset including experimental *I*-*V* curves that are acquired during a year at the Universidad de Jaén (Spain). Regarding the parameters extraction, two numerical algorithms (Levenberg-Marquardt, LM, and Simulated Annealing/Nelder Mead, SA/NM, optimizations) are employed to solve the most common circuit model (single diode model). Thus, the equations describing the parameters dependence with respect to irradiance and cell temperature are identified starting from the results of LM and SA/NM parameters extraction. Finally, the photovoltaic energy is predicted with previous equations and the most common theoretical model (Osterwald Model, OM): the LM equations exhibit the lowest deviation with respect to measurements (3,4%), while the error increases up to 3,6% and 5,5%, respectively, for the SA-NM equations and the OM.

Table of Contents

Abstract ... 1

Table of Contents ... 3

List of Figures ... 7

List of Tables ... 11

Glossary of Acronyms ... 13

Glossary of Symbols ... 15

Table of Constants ... 18

Introduction ... 19

Chapter 1 Introduction to solar energy ... 21

1.1. Photovoltaic generation of energy in Europe ... 21

Chapter 2 Photovoltaic module ... 25

2.1. Main photovoltaic module technology ... 25

2.1.1. Monocrystalline silicon technology ... 26

2.1.2. Polycrystalline silicon technology ... 26

2.1.3. Heterojunction with Intrinsic Thin Layer (HIT) silicon technology . 27

2.1.4. Passive Emitter and Rear Cell (PERC) silicon technology ... 27

2.1.5. Thin film technology ... 28

2.2. Solar cell and module manufacturing process ... 29

2.3. Photovoltaic effect and energy gap ... 31

2.4. Solar cell *I-V* curve ... 33

2.5. Series and parallel connections of photovoltaic cells ... 36

2.6. Standard Test Conditions (STC) ... 38

2.7. Nominal Operating Cell Temperature (NOCT) ... 39

2.8. Single diode model with five-parameters ... 39

2.9. Analytical description ... 41

Chapter 3 Optimization algorithms 43
3.1. Levenberg-Marquardt algorithm 44
3.2. Simulated Annealing algorithm 45
3.3. Nelder-Mead algorithm 46
Chapter 4 Automatic data acquisition system 49
4.1. *I-V* curve measurement principle 49
4.1.1. Capacitive load 50
4.2. Description of the measurement systems 51
4.2.1. Global description of the two systems 52
4.2.2. LabVIEW program 55
4.2.3. Weather station measurement sensors 57
4.2.4. Tracker system details 62
4.2.5. Fixed system details 64
4.3. Evaluation of uncertainty on measure 65
Chapter 5 Processing of experimental data (GUI) 67
Chapter 6 Data preprocessing 69
6.1. Graphical interface for data preprocessing 69
6.1.1. Import and export settings 70
6.1.2. Implemented data preprocessing for UJA (automatic system) 72
6.2. Software operation for data preprocessing 74
6.2.1. Load the CSV files 74
6.2.2. Sunny days filter 82
6.2.3. Irradiance, temperature, wind speed, check bits and monotonicity of short circuit current ranges filters 84
6.2.4. Mismatch detector filter 84
6.2.5. Save the data inside “mat” files 87
Chapter 7 Parameters extraction 91
7.1. Graphical interface for parameters extraction 91

7.1.1. Parameters extraction GUI settings 92
7.1.2. Parameters extraction result Graphical Interface 94
7.2. Software for parameters extraction 94
7.2.1. Equations for five parameters extraction 95
7.2.2. Evaluation of initial conditions 97
7.2.3. Calculation of deviation from experimental data 100
Chapter 8 Parameters Correlations 103
8.1. Graphical interface for correlations 103
8.2. Equation for parameters correlations 104
8.2.1. Photogenerated current correlation 104
8.2.2. Saturation current correlation 105
8.2.3. Ideality factor correlation 105
8.2.4. Series resistance correlation 106
8.2.5. Shunt resistance correlation 106
8.2.6. Normalized Root Mean Square Error (*NRMSE*) 107
Chapter 9 Power and Energy computation 109
9.1. Graphical interface for energy 109
9.2. Equation for Power and Energy computation 110
Chapter 10 Experimental data acquisition campaign 115
Chapter 11 Analysis of obtained results 119
11.1. Parameters extraction results 119
11.2. Parameters correlations results 122
11.3. Power validation and Energy computation results 134
Chapter 12 Conclusions 139
Annex A Technical datasheet of measurement equipment 141
A.1 Technical datasheet Agilent 34411A Multimeters 142
A.2 Technical datasheet Agilent 34970A Datalogger 145

A.3 Technical datasheet Agilent 34901A 20-Channel General Purpose Multiplexer 147
A.4 Technical datasheet Agilent 34907A Digital Multifunction Module 148
A.5 Technical datasheet Kipp and Zonnen CMP11 Pyranometer 149
A.6 Technical datasheet Kipp and Zonnen CHP1 Pyrheliometer 150
A.7 Technical datasheet Eko MS-700 Spectroradiometer 151
A.8 Technical datasheet Tri-band Spectro-Heliometer IES-UPM ICU-3J24... 152
A.9 Technical datasheet Young 05305VM anemometer 153
A.10 Technical datasheet Young 41382VC Relative Humidity and Temperature Probe 154
A.11 Technical datasheet Vaisala BAROCAP PTB110 barometer 155
A.12 Technical datasheet BSQ D150/6 Solar 2-axes tracker 156
Annex B Evaluation of tolerance on measure 157
B.1 Uncertainty on voltage measure 157
B.2 Uncertainty on current intensity measure 158
B.3 Uncertainty on irradiance measure 159
B.4 Uncertainty on module temperature measure 161
Annex C Datasheet of Sanyo HIT-240HDE4 module 163
Annex D Additional 3D plot of the parameters correlations results 167
References 171

List of Figures

Figure 1.1: Fuel mix in Gross Inland Consumption [1] ... 22
Figure 1.2: Photovoltaic capacity connected in the European Union in 2019 [2] ... 23
Figure 2.1: Champion module efficiencies [6] ... 25
Figure 2.2: Detail of a monocrystalline module [7] ... 26
Figure 2.3: Detail of a polycrystalline module [8] ... 26
Figure 2.4: Detail of a HIT cell's layer [9] ... 27
Figure 2.5: Detail of a PERC cell's layer [10] ... 28
Figure 2.6: Detail of a thin film module [11] ... 28
Figure 2.7: Structure details of a photovoltaic module [12] ... 30
Figure 2.8: Energy gap in different materials [13] ... 31
Figure 2.9: Best Research- Cell Efficiencies [14] ... 33
Figure 2.10: HIT cell *I-V* curve ... 34
Figure 2.11: Dependence of the *I-V* curve on temperature ... 35
Figure 2.12: Dependence of the *I-V* curve on irradiance ... 35
Figure 2.13: Series and parallel of equal *I-V* curves ... 36
Figure 2.14: Series connection of cells with different *I-V* characteristics [15] ... 37
Figure 2.15: Hot spots [16] [17] ... 37
Figure 2.16: Bypass and blocking diodes [18] ... 38
Figure 2.17: Five-parameters circuit model ... 40
Figure 2.18: Dependence of the *I-V* curve on the parallel and series resistances ... 41
Figure 4.1:Basic schematic of *I-V* curve measurement system ... 49
Figure 4.2: Charging transient of a capacitor connected with a PV module ... 50
Figure 4.3: Global scheme of the measurement systems ... 52
Figure 4.4: Scheme of the switching units ... 53
Figure 4.5: Picture of the multiplex board of each module ... 53
Figure 4.6: Picture of the join board [26] ... 54
Figure 4.7: LabVIEW graphical user interface of tracker system (*I-V*-curve tab) ... 55
Figure 4.8: LabVIEW measurement control software flowchart ... 56
Figure 4.9: Picture of the Pt100 probe to record the PV module temperature ... 57
Figure 4.10: Picture of the Kipp and Zonnen CMP11 pyranometer ... 58
Figure 4.11: Picture of the Kipp and Zonnen CHP1 pyrheliometer ... 59
Figure 4.12: Spectral irradiance distribution measured by EKO MS-700 ... 59

Figure 4.13: Picture of Eko MS-700 spectroradiometer 60
Figure 4.14: Picture of Tri-band spectro-heliometer from IES-UPM [27] 60
Figure 4.15: Picture of Young 05305VM anemometer 61
Figure 4.16: Picture of Young 41382VC temperature and relative humidity probe 61
Figure 4.17: Picture of Vaisala BAROCAP PTB110 barometer 61
Figure 4.18: Picture of tracker system (on the left the external part, on the right the internal equipment) 62
Figure 4.19: View of the inside of the capacitive load 63
Figure 4.20: Electrical scheme of the tracker system 63
Figure 4.21: Picture of fixed system (on the left the external part, on the right the internal equipment) 64
Figure 5.1: Flowchart of the four step of the GUI 67
Figure 5.2: MATLAB App Designer useful components 68
Figure 6.1: Picture of the graphical user interface tab for the preprocessing task 69
Figure 6.2: Picture of the graphical user interface for the preprocessing task-import and export settings 70
Figure 6.3: Picture of the window for selecting the saving properties 70
Figure 6.4: Example of ranges division 71
Figure 6.5: Picture of the module datasheet in Excel. The data are for the Sanyo HIT module s/n POHA8FA28569 from the 2011 CIEMAT calibration 71
Figure 6.6: Picture of the graphical user interface for the preprocessing task- UJA (automatic system) 72
Figure 6.7: Picture of the irradiance and temperature manual selection 73
Figure 6.8: Flowchart of the data preprocessing 74
Figure 6.9: Flowchart of the loading process 75
Figure 6.10: Extraction of the electrical quantities (in blue) from raw data (in orange). 76
Figure 6.11: Comparison between an original *I-V* curve (red) and the dynamic reduced one (blue). The two curves overlap except in the section near the OC point. 80
Figure 6.12: Sample of the struct of one "Measurement" cell 81
Figure 6.13: Sunny days filter: analysis for two different days. Sunny day upper and non-sunny day lower 83
Figure 6.14: Sample of a measure with mismatch. *I-V* curve on top and *P-V* curve on bottom. 85
Figure 6.15: Working principles of the mismatch filter on the *I-V* curve. 87
Figure 6.16: Saving data flowchart 89
Figure 7.1: Picture of the graphical user interface tab for the parameters extraction 91

Figure 7.2: Picture of the “Parameters extraction result GUI” 94
Figure 7.3: Flowchart of the parameters extraction procedure 95
Figure 7.4: Evaluation of initial conditions flow chart 97
Figure 8.1: Picture of the graphical user interface tab for the parameters correlation . 103
Figure 9.1: Picture of the graphical user interface tab for the power and energy computation 109
Figure 9.2: Computation of the integration time 112
Figure 10.1: Density distribution of the main four environment conditions for HIT module. 116
Figure 10.2: Irradiances during the year 117
Figure 10.3: Temperatures during the year 117
Figure 10.4: Irradiance and temperature of the *I-V* curves for parameters extraction . 118
Figure 11.1: *I-V* curves experimentally measured (dots) and trend estimated with the LM parameters 120
Figure 11.2: Distribution of the error at MPP for curves traced with LM method 121
Figure 11.3: Distribution of the error at MPP for curves traced with SA-NM method 121
Figure 11.4: Average time to extract the five parameters 122
Figure 11.5: Iph tendency with irradiance (LM algorithm) 123
Figure 11.6: Iph tendency with irradiance (SA-NM method) 124
Figure 11.7: $I0$ tendency with temperature (LM algorithm) 125
Figure 11.8: $I0$ tendency with temperature (SA-NM method) 126
Figure 11.9: n tendency with irradiance and temperature (LM algorithm) 127
Figure 11.10: n tendency with irradiance and temperature (SA-NM method) 128
Figure 11.11: Rs tendency with irradiance and temperature (LM algorithm) 129
Figure 11.12: Rs tendency with irradiance and temperature (SA-NM method) 130
Figure 11.13: Rsh tendency with irradiance (LM algorithm) 131
Figure 11.14: Rs tendency with irradiance (SA-NM method) 132
Figure 11.15: *NRMSE* for each parameters correlation 133
Figure 11.16: *I-V* curves experimentally measured (dots) and trend estimated with the correlation (LM method) 134
Figure 11.17: Comparison of power estimation for one day. LM and SA-NM model are overlapped 135
Figure 11.18: Power at different irradiance, experimental value vs the three models (Osterwald in blue, LM in orange, SA-NM in green) 136
Figure 11.19: *NRMSE* values on estimated power at MPP (division by day type) 137
Figure 11.20: *NRMSE* values on estimated power at MPP (division by irradiance) 137

Figure 11.21: Percentage error on estimated energy 138

List of Tables

Table 2.1: Energy gap of the major material used for photovoltaics cells........................ 31
Table 4.1: Resume of the worst case uncertainty 65
Table 10.1: Specifications of the HIT module. 115
Table 10.2: Temperature coefficients of the HIT module.. 115
Table 11.1: Correlation coefficients for the Sanyo HIT module 133

Glossary of Acronyms

Acronyms	Meaning
CIEMAT	"Centro de Investigaciones Energéticas, Medioambientales y Tecnológicas" in Madrid
AM	Air Mass
ADC	Analog-to-Digital Converter
APE	Average Photon Energy
CIS	Copper and Indium diselenide
DAC	Digital-to-Analog Converter
DNI	Direct Normal Irradiance
7P	Double diode seven parameters model
FF	Fill Factor
GHI	Global Horizontal Irradiance
GNI	Global Normal Irradiance
GTI	Global Tilted Irradiance (Global on-plane Irradiance)
GUI	Graphical User Interface
IDEA	Grupo de Investigación y Desarrollo en Energía Solar y Automática
HIT	Heterojunction with Intrinsic Thin Layer
LM	Levenberg-Marquardt algorithm
MPP	Maximum Power Point
MPPT	Maximum Power Point Tracking
NM	Nelder-Mead algorithm
NOCT	Nominal Operating Cell Temperature ($G_{NOCT} = 800\ Wm^{-2}, T_{c,NOCT} = 20\ °C, WS_{NOCT} = 1\ ms^{-1}$)
$NRMSE$	Normalized Root Mean Square Error
NaN	Not a Number value
OC	Open Circuit
PERC	Passive Emitter and Rear Cell
PV	PhotoVoltaic

Acronyms	Meaning
PoliTO	Politecnico di Torino
RTD	Resistance Temperature Detector
SC	Short Circuit
SA	Simulated Annealing algorithm
5P	Single diode five parameters model
STC	Standard Test Condition ($G_{STC} = 1000\ Wm^{-2}$, $T_{c,STC} = 25\ °C$, AM 1,5)
TRC	Temperature Coefficient of Resistance
Pt100	Temperature sensor ("Pt" platinum, "100" resistance in Ω at 0 °C)
UJA	Universidad de Jaén
I-*V*	Voltage and current characteristics of photovoltaic generator
P-*V*	Voltage and power characteristics of photovoltaic generator

Glossary of Symbols

Symbols	Meaning	Units
χ	Adimensional empirical coefficient of the diode saturation current	-
RH	Ambient air Relative Humidity	%
T_a	Ambient air temperature	°C
p_{atm}	Ambient pressure	hPa
APE	Average Photon Energy	eV
C	Capacitor Capacitance	F
t_c	Capacitor charging time	s
I	Current	A
I_{model}	Current (estimated from model)	A
I_{exp}	Current (experimental value)	A
I_j	Current in the diode (5P model)	A
I_{sh}	Current in the parallel resistance (5P model)	A
I_{MPP}	Current point at MPP	A
$I_{0,STC}$	diode saturation current at STC	A
B or DNI	Direct Normal Irradiance	$\mathrm{W \cdot m^{-2}}$
E_{model}	Energy (estimated from model)	J
E_{exp}	Energy (experimental value)	J
E_g	Energy gap	J
$E_{g,STC}$	Energy gap at STC	J
E	Energy in the considered period	kWh
E_{ph}	Energy of the photon	J
X_{cor}	Estimation from correlation parameter X value	-
X_{exp}	Experimental parameter X value	-
FF	Fill Factor	%
ν	Frequency	Hz
G_h or GHI	Global Horizontal Irradiance	$\mathrm{W \cdot m^{-2}}$
G	Global on-plane Irradiance	$\mathrm{W \cdot m^{-2}}$

Symbols	Meaning	Units
$G_{I_{sc}}$	Global on-plane irradiance from SC current	$\mathrm{W \cdot m^{-2}}$
b	Ideality factor correlation effect in irradiance	$\mathrm{W^{-1} \cdot m^{2}}$
c	Ideality factor correlation effect in temperature	$\mathrm{C^{-1}}$
a	Ideality factor correlation intercept	-
n	Ideality factor of the diode (5P model)	-
$i(t)$	Instantaneous current	A
$v(t)$	Instantaneous voltage	V
T_c	Module (or cell) temperature	°C
$T_{c,NOCT}$	Module (or cell) temperature from NOCT equation	°C
$T_{c,V_{oc}}$	Module (or cell) temperature from OC voltage	°C
$NOCT$	Nominal operating cell temperature	°C
$NRMSE$	Normalized Root Mean Square Error	%
$NRMSE_X$	NRMSE for parameter X	%
$NRMSE_I$	NRMSE on the current (parameters extraction)	%
$NRMSE_{P_{MPP}}$	NRMSE on the power at MPP	%
N_p	Number of cells in parallel	-
N_s	Number of cells in series	-
N_{ph}	Number of incident photons (5P model)	$\mathrm{m^{-2} \cdot s^{-1}}$
N_{points}	Number of points	-
V_{oc}	Open circuit voltage	V
$V_{oc,STC}$	Open circuit voltage at STC	V
$\beta_{V_{oc}}$ or β	Open circuit voltage temperature coefficient	$\mathrm{°C^{-1}}$
Err_E	Percentage error on the energy	%
Err_{maxP}	Percentage error on the maximum power point	%
I_{ph}	Photogenerated current	A
$I_{ph,STC}$	Photogenerated current at STC	A
P_{MPP}	Power at Maximum Power Point (MPP)	W
$P_{MPP,model}$	Power at MPP (estimated from model)	W
$P_{MPP,exp}$	Power at MPP (experimental value)	W
P_{STC}	Power at MPP at STC	W
$P_{Osterwald}$	Power at MPP by the Osterwald method	W

Symbols	Meaning	Units
γ	Power thermal coefficients	$(\% \cdot \mathrm{K}^{-1}$
A	Proportionality factor for capacitor charging time	-
R_0	Pt100 sensor resistance at 0 °C	Ω
R_{100}	Pt100 sensor resistance at 100 °C	Ω
I_o	Reverse saturation current of the diode (5P model)	A
R_s	Series resistance (5P model)	Ω
$R_{s,STC}$	Series resistance at STC	Ω
λ_{R_s}	Series resistance correlation empirical coefficient	-
I_{sc}	Short circuit current	A
$I_{sc,STC}$	Short circuit current at STC	A
$\alpha_{I_{sc}}$ or α	Short circuit current temperature coefficient	$°\mathrm{C}^{-1}$
R_{sh}	Shunt (or parallel) resistance (5P model)	Ω
$R_{sh,STC}$	Shunt resistance at STC	Ω
$F(\lambda)$	Spectral irradiance at wavelength λ	$\mathrm{W} \cdot \mathrm{m}^{-2} \cdot \mu\mathrm{m}^{-1}$
$\Phi(\lambda)$	Spectral photon flux density at wavelength λ	$\mathrm{m}^{-2} \cdot \mathrm{nm}^{-1} \cdot \mathrm{s}^{-1}$
S	Surface of the cell	m^2
V_t	Thermal voltage (5P model)	V
V	Voltage	V
V_{exp}	Voltage (experimental value)	V
V_j	Voltage on the diode (5P model)	V
V_{MPP}	Voltage point at MPP	V
λ	Wavelength	μm
WD	Wind Direction	deg
WS	Wind Speed	ms^{-1}

Table of Constants

Symbols	Meaning	Value	Units
$T_{a,NOCT}$	Air temperature in NOCT	25	°C
k_B	Boltzmann constant	$1{,}38 \cdot 10^{-23}$	$\mathrm{J \cdot K^{-1}}$
q_e	Electron charge	$1{,}602 \cdot 10^{-19}$	C
G_{NOCT}	Module (or cell) irradiance in NOCT	800	$\mathrm{Wm^{-2}}$
G_{STC}	Module (or cell) irradiance in STC	1000	$\mathrm{Wm^{-2}}$
$T_{c,STC}$	Module (or cell) temperature in STC	25	°C
h	Plank constant	$6{,}626 \cdot 10^{-34}$	$\mathrm{J \cdot s}$
α_{Pt100}	Pt100 temperature coefficient	0,00385	$\Omega \cdot \Omega^{-1} \cdot \mathrm{K^{-1}}$
c	Speed of light in vacuum	$2{,}998 \cdot 10^{8}$	$\mathrm{m \cdot s^{-1}}$

Introduction

The performance of photovoltaic generators can be described by an equivalent circuit with a variable number of parameters, which are, generally, assumed constant. However, the knowledge of their dependence with respect to irradiance and cell temperature permits to predict the generated power of photovoltaic arrays in any weather condition. Moreover, the knowledge of the parameters in any condition allows to trace the current-voltage (*I-V*) characteristic curve of the photovoltaic generators. This information may be used in future works to evaluate the state of health of photovoltaic arrays by investigating the shape of the *I-V* curve and the values of circuit parameters, predicted in any environmental condition.

This thesis focuses on the experimental validation of an innovative technique to predict the parameters of the equivalent circuit in any weather condition. This work is a part of a joint activity between Politecnico di Torino and the Universidad de Jaén (Spain): the first part of the thesis has been performed in Politecnico di Torino, while the second activity of the thesis has been developed in Universidad de Jaén.

In the first part of the thesis, an ad hoc Graphical User interface (GUI) is developed in MATLAB ambient to permit the massive analysis of a wide dataset of experimental data. In particular, the tool allows to perform four operations: the preprocessing of the dataset; the extraction of the circuit parameters; the identification of equations, aiming at describing the dependence of each parameter with respect to irradiance and cell temperature; and the comparison between experimental energy and the predicted value with several methods. Experimental data may be affected by measurements errors or the photovoltaic generators may work in mismatch conditions due to shadowing or other issues. However, the present analysis requires experimental measurements of photovoltaic generators correctly operating: thus, the preprocessing step removes problematic measurements integrating ad hoc filters. Firstly, experimental data with measurement errors are filtered by comparing the irradiance and the temperature detected by the sensors: in case of high deviations among the measured quantities, the empirical data are excluded. Then, measurements obtained on cloudy/partly cloudy days with abrupt irradiance variations or *I-V* curves under mismatch are removed.

The parameters extraction step is the core of the tool: in this step, the parameters are numerically determined starting from the filtered measurements. The GUI permits to identify the circuit parameters using up to two circuit models and three numerical algorithms. The third step of the analysis regards the identification of the dependence of circuit parameters with respect to cell temperature and irradiance. In particular, the most common equations in literature are used and a nonlinear optimization of specific coefficients is performed. Finally, the generated energy during the experimental campaign is compared to the predicted value by several methods. The GUI permits to estimate expected energy using theoretical models and the optimized equations: starting from the knowledge of the parameters, the *I-V* curve is traced at each time step and the corresponding maximum power is identified.

In the second part of this thesis, the GUI is applied to a high efficiency Heterojunction with Intrinsic Thin layer (HIT) module with rated power of 240 W. The experimental campaign under analysis lasted twelve months. Moreover, the single diode model, which is the most common circuit model in literature, is used. Regarding the numerical algorithms, the Levenberg Marquardt and Simulated Annealing/Nelder Mead algorithms are adopted. Finally, the results of energy prediction are compared between experimental data, the optimized equations and the Osterwald model (the most common theoretical model in literature to estimate photovoltaic power).

Chapter 1

Introduction to solar energy

In this chapter the European commitment to the climate front and the future targets are presented. The photovoltaic sector is playing a decisive role to achieve the goals of 2050.

1.1. Photovoltaic generation of energy in Europe

The document "A Clean Planet for all. A European strategic long-term vision for a prosperous, modern, competitive and climate neutral economy" [1] of 2018 reaffirms the European commitment to act on the climate front with a long-term strategy. In particular, it indicates the route of EU climate and energy policies to achieve the targets set for 2030. Recently, Europe has been showing the negative consequences of excessive human activities through extreme temperature manifestations and adverse climatic events as floods. Acting on the climate front is necessary to avoid economic, public health, as well as environmental damage. An important point of this strategy aiming to reach the zero net emissions quota regards renewable energies. Large-scale electrification based on renewable energy is expected to limit dependence on fossil fuels by the middle of the century. After the transition to clean energy, an energy system is envisaged in which primary energy will come largely from renewable sources, thereby significantly improving security of supply and internal employment. The numerical data provided by the document indicate that in 2018 the energy imported from Europe is 55% (including oil and gas), thus pointing out a strong foreign dependence. Some scenarios predict a drop in fossil fuel imports of more than 70% by 2050, with a drastic reduction in spending in this sector. Moreover, it is expected that by 2050 the share of electricity in the final energy demand will double, reaching 53%, and electricity production will increase substantially up to two and a half times the current levels. Transformation of electricity production in Europe represents a substantial progress. Today more than half of Europe's electricity supply does not involve the release of greenhouse gas emissions and by 2050 over 80% will come from renewable sources. Besides, the competitive distribution of electricity from renewable sources also offers an important opportunity for the decarbonization of other sectors, such as heating, transport and industry. To move on to a largely decentralized and renewable energy system, it is necessary to make it more "intelligent" and flexible, focusing on these features: consumer participation, greater interconnectivity, better large-scale energy storage, demand management and digitalization. of management practices.

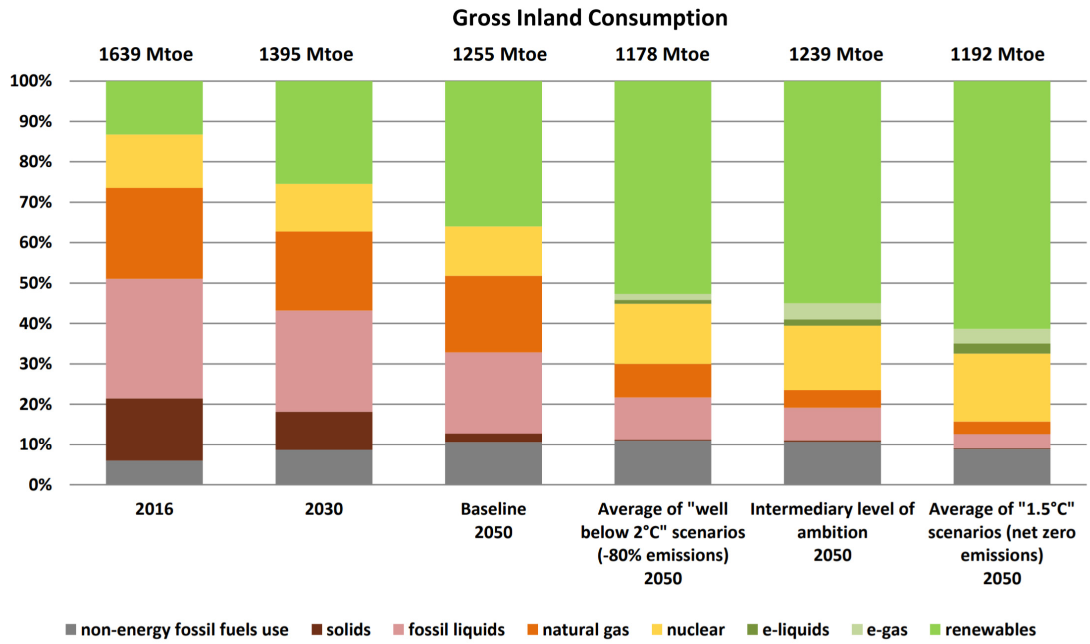

Figure 1.1: Fuel mix in Gross Inland Consumption [1]

Nowadays, the photovoltaic solar generation plays an important role in the achievements of the next removable energy target. In fact, an installation peak was expected in 2020, before the Covid-19 crisis [2]. In 2019 Germany and Italy were the European countries leader for photovoltaic installations, respectively with 49,016 and 20,864 GW in cumulated capacity. Other important data show the recovery of the sector in Spain with the European record for installed capacity in 2019 of 3,992 GW.

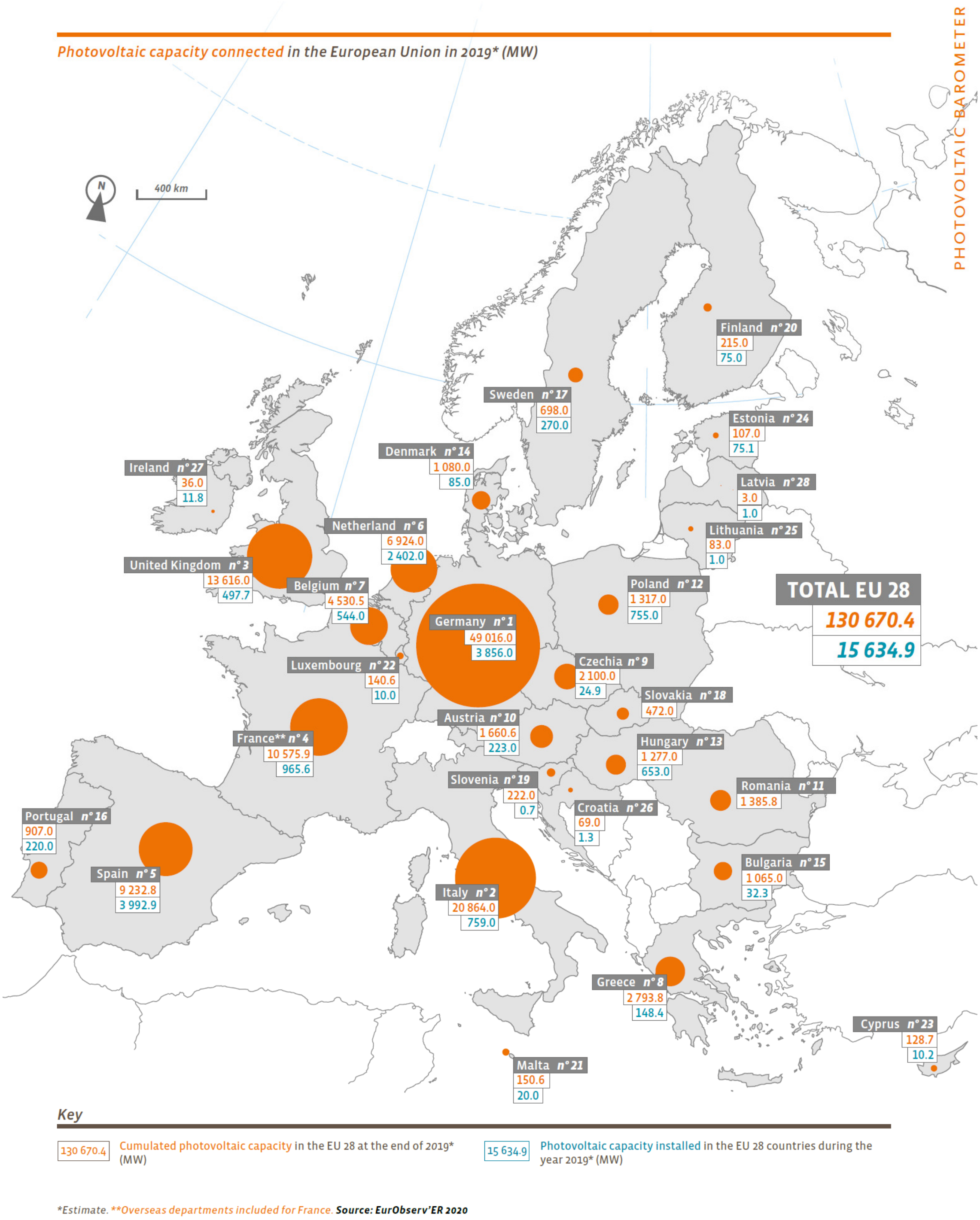

Figure 1.2: Photovoltaic capacity connected in the European Union in 2019 [2]

The data in these documents indicate that the photovoltaic market is growing more and more and, in this scenario, research in the photovoltaic sector is promising. With this thesis I try to give a small contribution to this sector.

Chapter 2

Photovoltaic module

Some generical concepts about the electric generation from solar energy are reported in this chapter [3], [4], [5]. Firstly, the main commercial module technology and its manufacturing process are described. Then, the photovoltaic effect is explained. The remaining paragraphs focus on the description of the solar cells, the elementary units of photovoltaic technology.

2.1. Main photovoltaic module technology

There are several technologies currently on the market that differ in performance, construction technology and price. The Figure 2.1, updated to 2020, shows the best modules on the market in terms of efficiency.

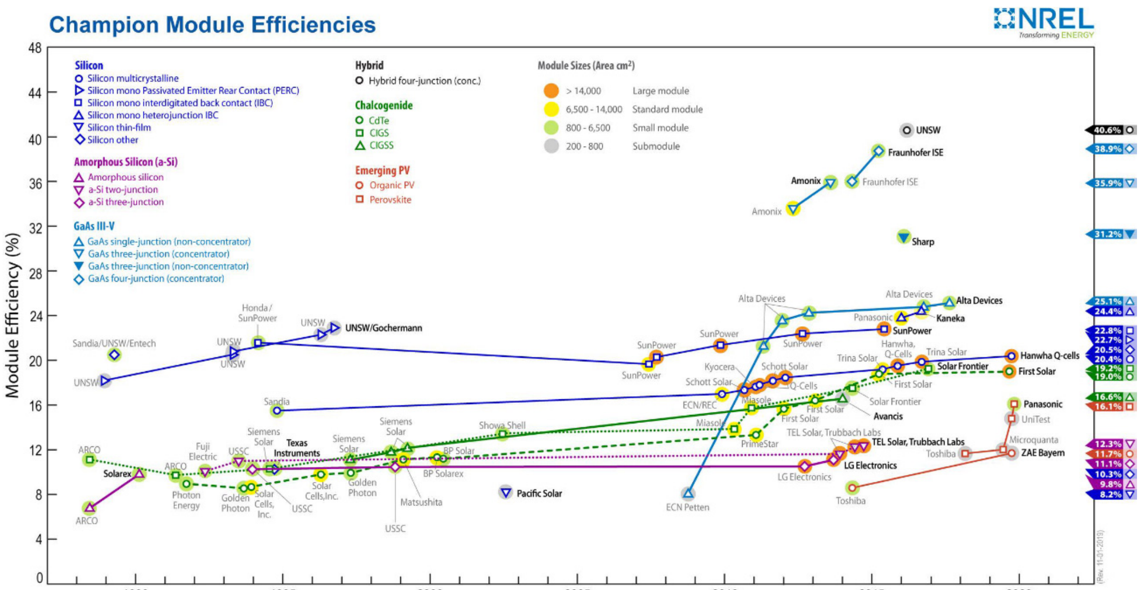

Figure 2.1: Champion module efficiencies [6]

These data confirm the growth of interest in the photovoltaic sector. Research has led to a dramatic improvement in performance over the past 10 years. Some technologies of interest are here analyzed.

2.1.1. Monocrystalline silicon technology

The monocrystalline silicon features are its high purity and a regular structure consisting of a single crystal. The manufacturing process is slow and, moreover, expensive: in fact, it is one of the most high-priced technology on the market. But, due to its cost, the efficiency of a monocrystal cell is high, around 26%, whereas the module around 24% as in Figure 2.1 and Figure 2.9 below. The cells are square-shaped with round corner. Their typical colors are dark blue and black, as in Figure 2.2.

Figure 2.2: Detail of a monocrystalline module [7]

2.1.2. Polycrystalline silicon technology

The polycrystalline silicon has a structure with regular zones. In fact, each area is a single-crystal, separated from the others by grain boundaries that reduce the overall efficiency. The performance of a polycrystalline technology is around 24% for the cell and around 20% for the module. The manufacturing process is simpler and cheaper than the monocrystalline silicon. As in monocrystalline technology, the shape of a cell is square. Here cells are generally blue with lighter reflections.

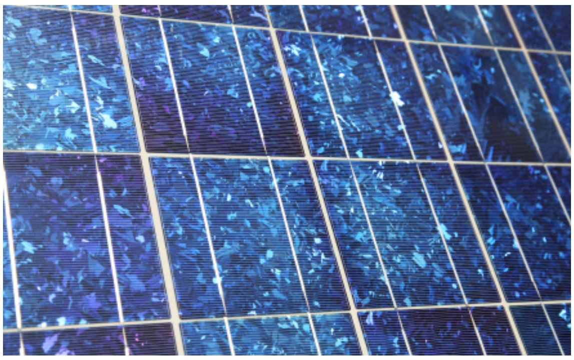

Figure 2.3: Detail of a polycrystalline module [8]

2.1.3. Heterojunction with Intrinsic Thin Layer (HIT) silicon technology

The solar cell based on Heterojunction with Intrinsic Thin layer (HIT) technology is an evolution of the standard monocrystalline cell. A thin monocrystalline layer inside two ultra-thin amorphous silicon layers are distinguishable in the Figure 2.4. Conventional photovoltaic cells experience losses in energy generation due to faulty areas in their internal structure. The union of the two materials reduces the faulty areas and consequently the performance of the panels increases. These modules are characterized by an excellent temperature coefficient. The temperature coefficient measures the reduction of photovoltaic cells' energy power when the temperature of the cells increases (due, for example, to high heat).

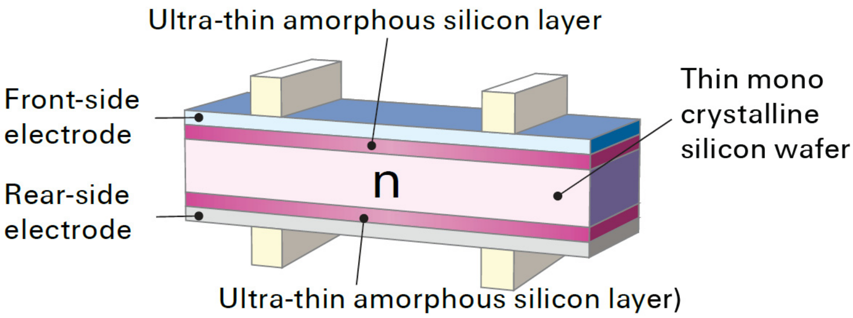

Figure 2.4: Detail of a HIT cell's layer [9]

2.1.4. Passive Emitter and Rear Cell (PERC) silicon technology

The modules with Passive Emitter and Rear Cell (PERC) technology are an evolution of the standard monocrystalline cell. A monocrystalline cell with the passiveness of the back layer is illustrated in detail in the Figure 2.5. This structure allows a better photon recombination due to an increase in reflection inside the junction. The absorbed solar spectrum increases, with an efficiency improvement of about 1% compared to a conventional monocrystalline cell.

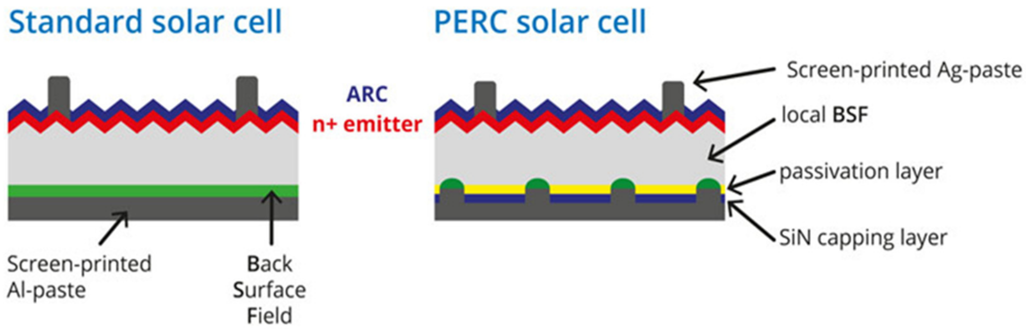

Figure 2.5: Detail of a PERC cell's layer [10]

2.1.5. Thin film technology

Thin film family technology involves the use of a very thin layer of conductive material on surfaces of other materials, such as glass, plastic or metal. The semiconductor materials used in this technology are mainly amorphous silicon, CdTe, CIGS and CIS. The efficiency of this technology is significantly lower, in the order of 5-6,8% and it is subject to a decay of its performance in the first month of life.

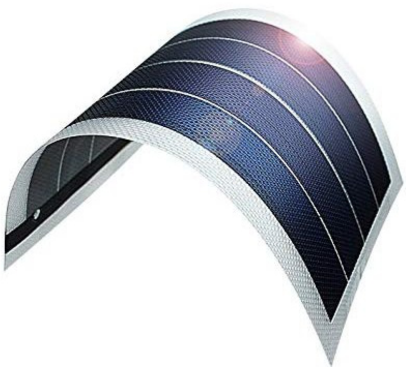

Figure 2.6: Detail of a thin film module [11]

CIS technology is here analyzed because this type of module is present in the Spanish laboratory. The acronym CIS indicates the elements which it is composed of: copper (Cu), indium (I) and selenium (S). This technology can be compared to the silicon one. On the one hand, one of the CIS main advantage is the better energy yield in case of partial or problematic lighting. In fact, in conditions of non-optimal irradiation or shading, a silicon panel proves to be less efficient than a CIS model, up to 10%. Besides CIS panels are also more flexible and resistant to critical atmospheric conditions and bad weather. On the other hand, the main disadvantage is the dimension of the modules, considerably large compared to common silicon installations, which occupy less space with equal power.

2.2. Solar cell and module manufacturing process

The technology of making silicon-based modules will be now analyzed. Silicon is the most widely used material to produce photovoltaic cells due to its abundance in the terrestrial cortex in the form of both SiO_2 and silicate minerals. A silicon with impurity level in the rank of parts per millions can be obtained, starting from natural silicon mineral, with the following steps:

1. Reduction of SiO_2 to Si of low purity with C using electric arc furnace (EAF)
2. Transformation into an intermediate chemical compound such as trichlorosilane ($HSiCl_3$)
3. Purification with distillation or other technique
4. Reduction of the intermediate compound to Si with low impurities
5. Crystal growth with additional purification

The monocrystals (crystalline silicon) or crystal conglomerates ingots (polycrystalline silicon) are obtained during the crystallization process. These ingots of monocrystalline or polycrystalline material are cut into wafers with the thickness of the cell (300 µm). Up to 20% of the ingot is wasted with this process. The following steps are required to manufacture a conventional cell from a wafer:

1. Cleaning: the wafers are cleaned to eliminate the metal and organic remains of the previous phases. Acids with the ability to dissolve metals (HCl, NO_3H) are used.
2. Pickling: the wafers are immersed in 30% NaOH hot solution at 90°C. This step eliminates irregularities and surface defects caused by wafer cutting.
3. Texturization: this procedure consists of creating micro pyramids on the surface that are intended to reduce losses for reflection. This process applies only to Si monocrystal wafers. For the polycrystalline these losses are reduced with anti-reflective layers.
4. Cleaning: this process eliminates SiO_2 surface oxide formed in previous steps (contact with HF).
5. Predisposition of doping material: the wafers are of type p (doped with Boron). The p-n junction is formed by diffusion of n-type dopant (Phosphorus) in the front face of the wafer. In this step, the n-type dopant is deposited on the wafer. There are various methods to do so (screen printing, centrifuge, solid source, liquid, or gas)

6. Formation of the p-n junction by diffusion. The wafers are inserted with n-type material predisposed in high-temperature ovens (up to 1000 °C).
7. Cleaning the remnants of the diffusion.
8. Formation of rear metal contact by screen printing.
9. Formation of the front metal contact.
10. Isolation of n and p zones.
11. Deposition of the anti-reflective layer. This cover is a thin transparent material that adapts the silicon and glass refraction indices.
12. Back surface field. A p-p+ union is created on the back to form an electric field that decreases the recombination of minority carriers in the back surface.
13. Passivation with hydrogen (only polycrystalline case). This process consists of the hydrogen neutralization of a large number of defects and dislocations by increasing the lifetime of minority carriers.

The resulting photovoltaic cells are arrayed in order to obtain photovoltaic modules and to achieve adequate operation power. The steps of the process are:

1. Welding: strips of stagnated copper are welded on the main busbars of the front face of each cell. The busbars collect the photogenerated current and they "bring the current outside".
2. Interconnection: the cells are interconnected by joining the copper strips of the front face to the back face of the other cell.
3. Lamination: a process in which the encapsulating (EVA), Tedlar and Glass are compacted.
4. Framing and connection case: insertion of the aluminum frame, which has different functions: firstly, protection from blows and moisture; secondly, making the module manageable; finally it is a sort of junction box and of the junction box with three terminals and the bypass diode.

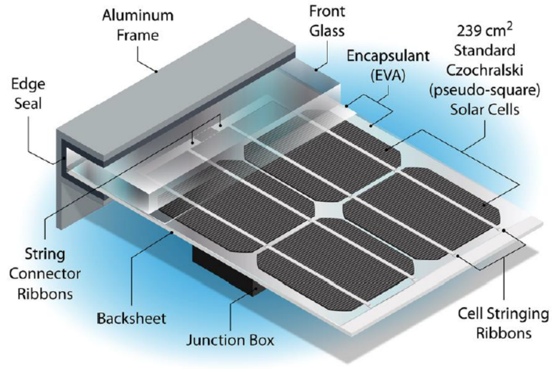

Figure 2.7: Structure details of a photovoltaic module [12]

2.3. Photovoltaic effect and energy gap

The photovoltaic generation of energy is the direct conversion of the solar energy, coming to the earth as an electromagnetic radiation, into an electrical energy. This energy can be used directly in the form of direct current or transformed into alternating current. This type of electrical generation is made thanks to the semiconductor materials inside the photovoltaic module. The energy conversion takes place inside the solar cells, i.e. the elementary units of photovoltaic technology.

The energy gap physical principle is useful to understand the operation of the solar cell. The energy gap is the amount of energy that an electron must receive to move from the valence band to the conduction band. All materials can be catalogued according to their energy gap, as reported in Table 2.1. This gap is low for conductors and very high for insulants. Besides, semiconductors are in an intermediate situation. When an electron receives sufficient energy, it can switch from the valence band to the conduction band.

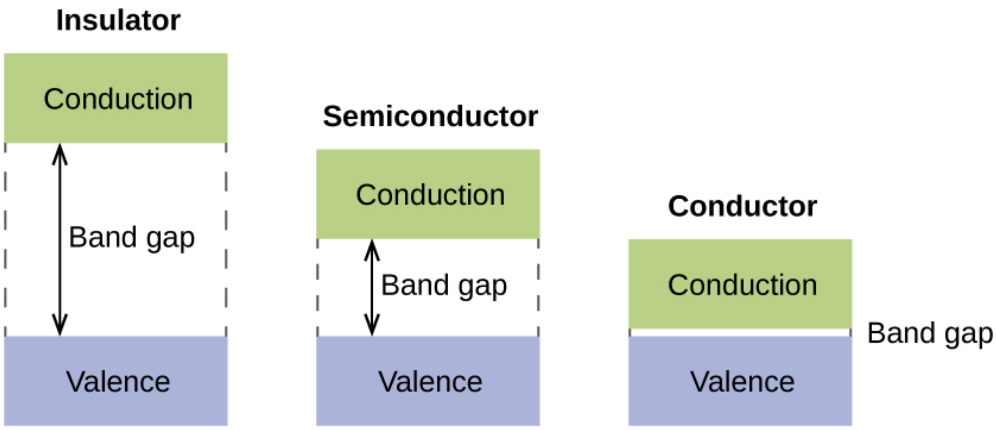

Figure 2.8: Energy gap in different materials [13]

Material	Energy gap (eV) @ 300 K
Crystalline silicon (c-Si)	1,12
Amorphous silicon (a-Si)	1,75
Germanium (Ge)	0,67
Gallium Arsenide (GaAs)	1,42
Iridium Phosphide (InP)	1,34
Copper Indium Diselenide ($CuInSe_2$)	1,05
Cadmium Telluride (CdTe)	1,45
Cadmium Sulfide (CdS)	2,40

Table 2.1: Energy gap of the major material used for photovoltaics cells

The physical phenomenon in which electricity is produced from solar radiation is the photovoltaic effect. This conversion is possible thanks to the properties of the semiconductors such as silicon. The photovoltaic effect is precisely the transition of an electron from the valence band to the conduction band. This phenomenon occurs when this equation is verified:

$$E_{ph} = h \cdot \nu = h \cdot \frac{c}{\lambda} \geq E_g \quad (2.1)$$

Where:

- E_{ph} is the energy of the photon (J)
- h is the Plank constant ($6{,}626 \cdot 10^{-34}$ J · s)
- ν is the frequency (Hz)
- λ is the wavelength (m)
- c is the speed of light in vacuum ($2{,}998 \cdot 10^{8}$ m · s^{-1})
- E_g is the energy gap (J)

Each photon from the Sun can release only one electron. If the received energy is not sufficient, the electron does not pass to the excited state. In this case, the energy received from the solar radiation is absorbed by the crystal structure of the silicon in the form of heat. However, if the received energy is greater than the energy gap, the electron passes to the conduction band. Each electron that passes to the conduction band creates a hole in the valence band. In the undoped silicon, when the electron loses its energy, it falls back into the valence band recombining with the hole previously created. When this happens, the energy previously received (i.e. from solar radiation) is dissipated in the form of heat and it can no longer be converted into useful electrical power. An electric field is necessary to separate the electrons and holes and prevent them from recombining. This electric field causes both particles to circulate in opposite directions by giving rise to a current with the same direction as the electric field.

In conventional solar cells this electric field is obtained by the union of two regions of a semiconductor crystal. On the one hand, in the case of silicon, one region is drugged with phosphorus (5 valence electrons, one more than silicon). The result is a region with a concentration of more electrons than holes. This is the so-called n-type region. On the other hand, the second region is drugged with boron (3 valence electrons, one less than silicon). The result is opposite to the previous one: a region with a concentration of more holes than electrons. This is the so-called p-type region. The union of the two regions is known as p-n junction. The large difference in the concentration of electrons and holes creates an electric field orientated with the p-type region. This field separates the electrons and the holes when the cell receives the light. Therefore, the photovoltaic current is generated, and it is mainly proportional to the irradiance.

2.4. Solar cell *I-V* curve

The solar cell is the basic unit of a photovoltaic module. The cells are made up of semiconductor material: PhotoVoltaic (PV) conversion takes place inside them. A PV cell has an open circuit voltage of 0,6 V and a short circuit current that depends on the cell surface. Therefore, a single cell has a small output power (i.e. 3 or 4 W for modern high efficiency cells). The Figure 2.9, updated to 2020, shows the best research cell in terms of efficiency.

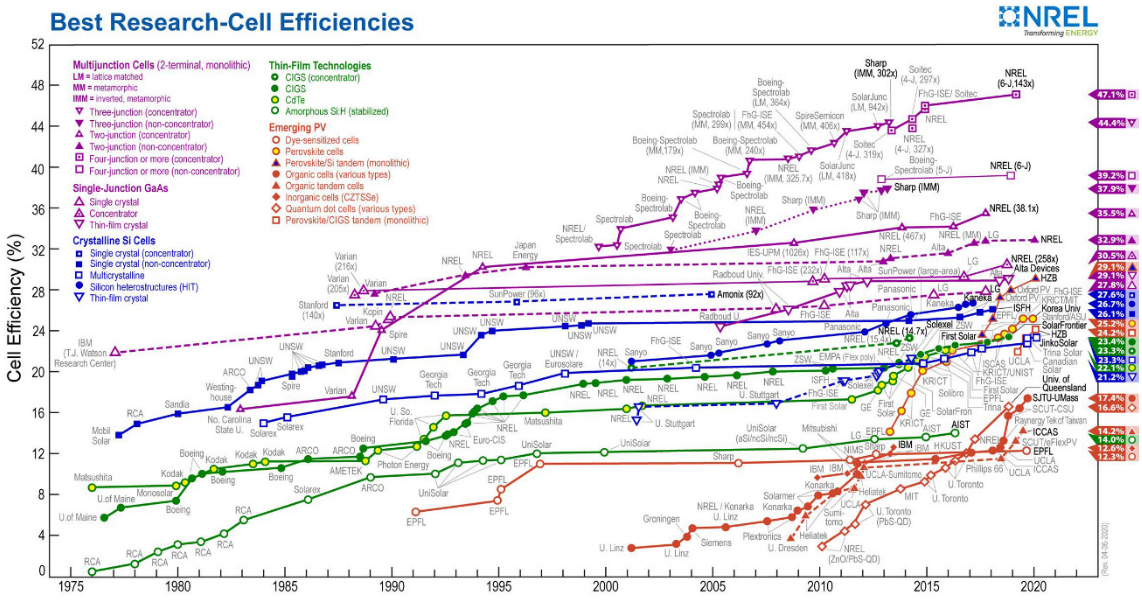

Figure 2.9: Best Research- Cell Efficiencies [14]

The electrical behavior of a solar cell is described with an *I-V* curve. The correct acquisition of this characteristic curve is described in 4.1.

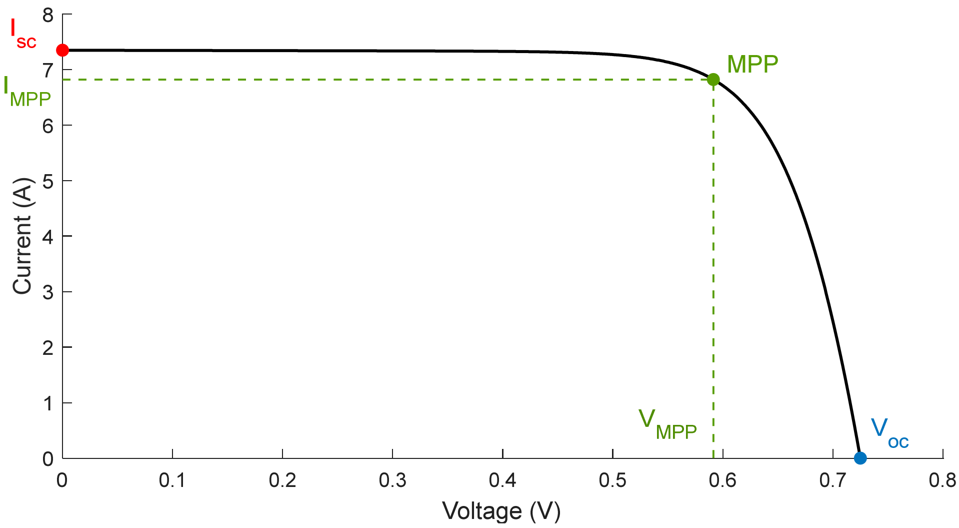

Figure 2.10: HIT cell *I-V* curve

These characteristic points can be identified:

- V_{oc} is the open circuit voltage (V)
- I_{sc} is the short circuit current, the maximum current at zero voltage (A)
- P_{MPP} is the point of maximum power produced by the cell (W). This power is the ideal operating point. The current and voltage values that correspond to P_{MPP} are called maximum power current I_{MPP} and maximum power voltage V_{MPP}, respectively.

There are four basic properties of the *I-V* curve connected with V_{oc} and I_{sc}. The first is that tension increases logarithmically with irradiation. V_{oc} decreases as the temperature increase. These dependencies are translated into the following simplified formula. In fact, dependence on irradiance does not appear.

$$V_{oc}(T_c) = V_{oc,STC} \cdot \left(1 + \beta_{V_{oc}} \cdot (T_c - T_{c,STC})\right) \tag{2.2}$$

Where:

- $V_{oc,STC}$ is the open circuit voltage in STC conditions (see 2.6) (V)
- $\beta_{V_{oc}}$ is the OC voltage temperature coefficient (°C^{-1})
- T_c is the cell temperature (°C)
- $T_{c,STC}$ is the cell temperature in STC (see 2.6) (°C)

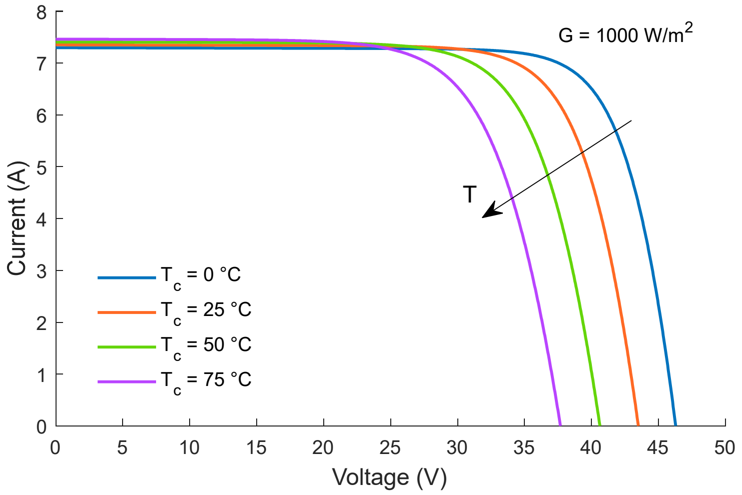

Figure 2.11: Dependence of the *I*-*V* curve on temperature

The third is that current is directly proportional to radiation. I_{sc} increases slightly as the temperature rises.

$$I_{sc}(G,T_c) = I_{sc,STC} \cdot \frac{G}{G_{STC}} \cdot \left(1 + \alpha_{I_{sc}} \cdot \left(T_c - T_{c,STC}\right)\right) \tag{2.3}$$

Where:

- $I_{sc,STC}$ is the short circuit current in STC conditions (see 2.6) (A)
- G is the incident irradiance ($\mathrm{W \cdot m^{-2}}$)
- G_{STC} is the incident irradiance in STC (see 2.6) ($\mathrm{W \cdot m^{-2}}$)
- $\alpha_{I_{sc}}$ is the SC current temperature coefficient ($\mathrm{°C^{-1}}$)

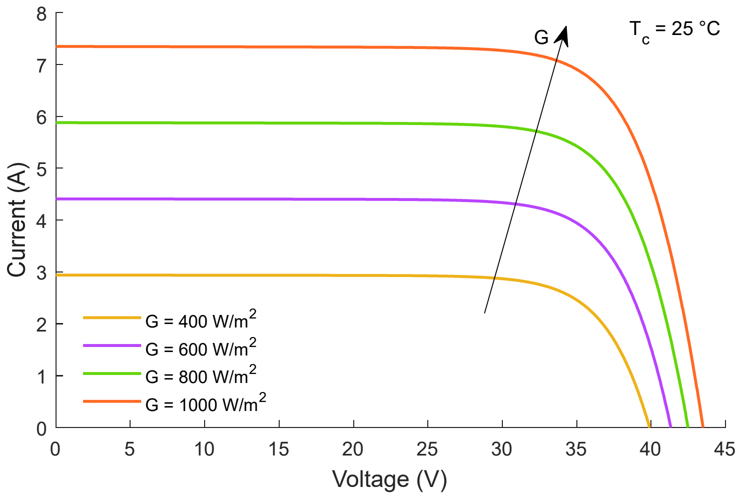

Figure 2.12: Dependence of the *I*-*V* curve on irradiance

2.5. Series and parallel connections of photovoltaic cells

The power of one cell is not sufficient for commercial application. Consequently, the solution is connecting the cells in series and/or in parallel in order to form a PV module. However, if the power provided by a PV module is not sufficient for a given application, the modules can be connected in series and parallel to form a PV generator. When the cells are connected in series, they are crossed by the same current and the resulting voltage is the sum of the voltages of each cell. When cells are connected in parallel, they are characterized by the same voltage and the resulting current is the sum of the currents of each. Figure 2.13 shows how to graphically obtain the curve of a module or a PV generator with the connections in series and parallel.

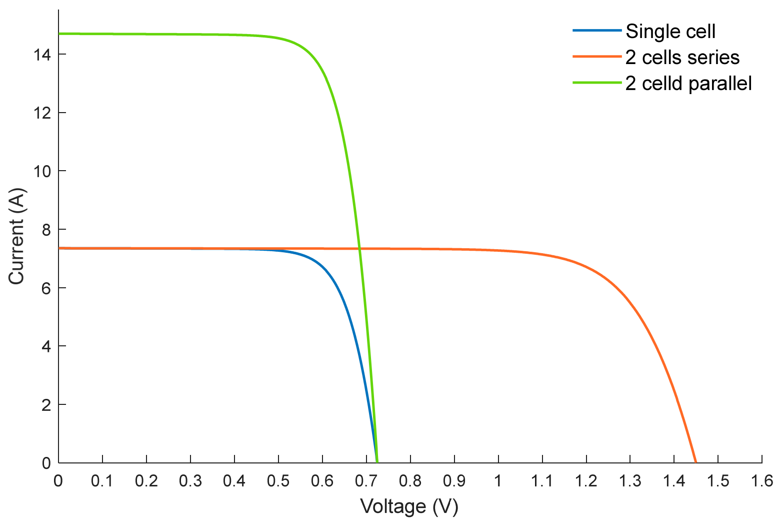

Figure 2.13: Series and parallel of equal *I*-*V* curves

These curves are obtained assuming that the cells (and their *I*-*V* curve) are perfectly equal. Otherwise mismatch effects are produced. Mismatch can occur due to shading or construction defects. The procedure for obtaining an *I*-*V* curve of different cells is the same as in the case of equal cells. Therefore, on the one hand, a series link of two different cells have an *I*-*V* curve that has a total voltage equal to the sum of the corresponding cell voltages for each current value. On the other hand, a parallel link of two different cells have an *I*-*V* curve that for each voltage value has a total current equal to the sum of the corresponding currents of the cells.

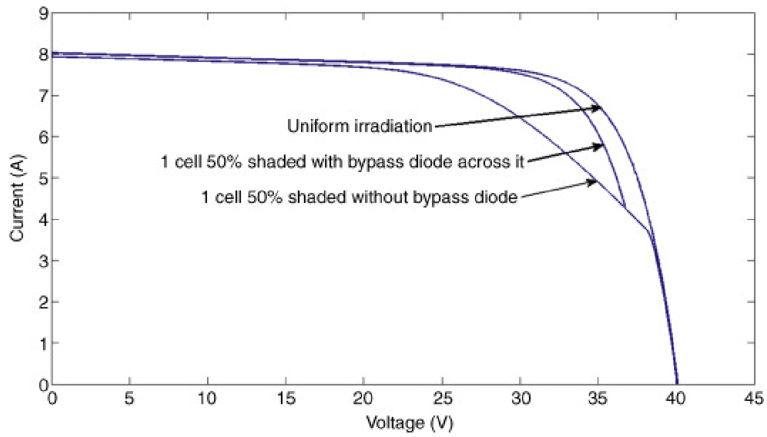

Figure 2.14: Series connection of cells with different *I-V* characteristics [15]

The series connection of cells with different *I-V* characteristics causes a module power lower than the sum of the power of each single cell, as can be seen from Figure 2.14. This problem is known as mismatch leaks. The most critical consequence is in the case of significant connection mismatch, when some "defective" cells dissipate the power produced by the other cells. This dissipation occurs in the form of heat with the consequent creation of hot spots, as in Figure 2.15. Also, the mismatch can cause irreversible damage to the cell.

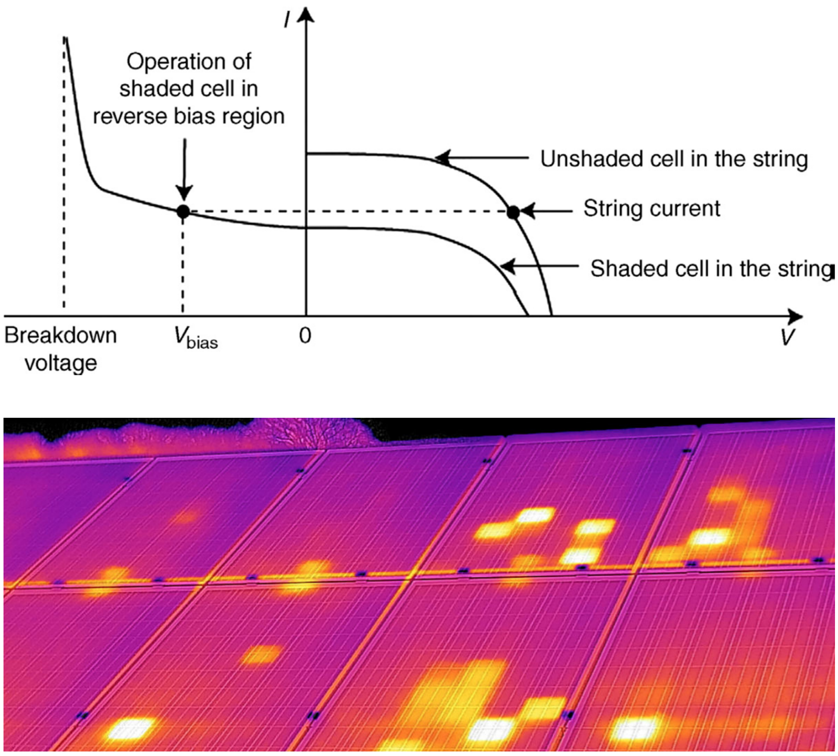

Figure 2.15: Hot spots [16] [17]

The insertion of bypass diodes into the modules prevent these problems (mismatch and hot-spot losses). These diodes are placed in the junction box. In fact, the diodes offer an alternative path to the current when there is a defective or shaded cell in the circuit. Under normal conditions the diodes are polarized inversely, and they do not lead current.

A similar phenomenon occurs when many cells are connected in parallel. To prevent hot-spots and current recirculation between distinct branches, block diodes are inserted in series to the cells.

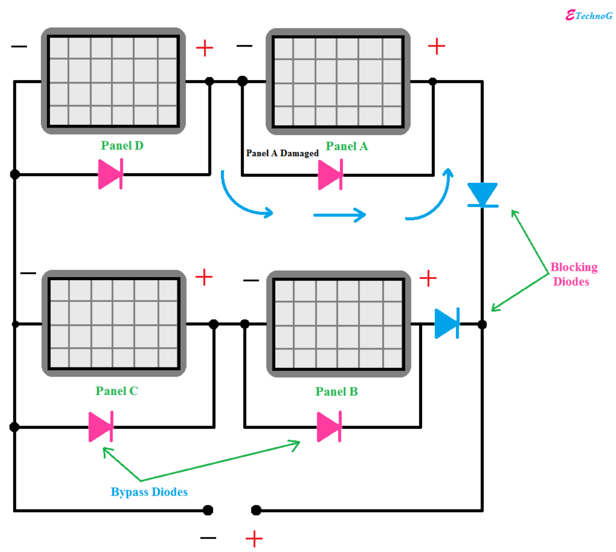

Figure 2.16: Bypass and blocking diodes [18]

2.6. Standard Test Conditions (STC)

The Standard Test Conditions (STC) are defined in the IEC/EN60904 to ensure that the modules are tested under the same conditions. The legislation requires that, during tests for the characterization of electrical parameters and performance of the module, the STC conditions are met. The STC conditions consist of:

- Irradiance of 1000 $W \cdot m^{-2}$
- Cell Temperature of 25 $°C$
- Air Mass AM 1,5

2.7. Nominal Operating Cell Temperature (NOCT)

The standard Nominal Operating Cell Temperature (NOCT) is defined in the IEC/EN60904. The NOCT is the temperature at which the module stabilizes when working under open circuit conditions in the following environment circumstances:

- Irradiance of 800 $W \cdot m^{-2}$
- Wind speed of 1 $m \cdot s^{-1}$
- Air temperature of 20 °C

In fact, the NOCT establishes the following relation between the ambient air temperature and the cell temperature

$$T_c = T_a + \frac{NOCT - T_{a,NOCT}}{G_{NOCT}} \cdot G \tag{2.4}$$

Where:

- T_c is the cell temperature (°C)
- T_a is the air temperature (°C)
- $T_{a,NOCT}$ is the air temperature at NOCT (°C)
- G is the irradiance ($\mathrm{W \cdot m^{-2}}$)
- G_{NOCT} is the irradiance at NOCT

2.8. Single diode model with five-parameters

The behavior of a photovoltaic cell can be schematized from an electrical point of view with an equivalent circuit composed of a current generator, which represents radiation, and of an antiparallel diode. The ideal current generator produces a current proportional to the irradiance received by the cell. The diode (D) represents the straightening effect of the electric field generated by the p-n junction. In the absence of radiation, the equivalent circuit is simply a diode. Two resistances are added to this basic circuit:

- R_{sh} is the parallel resistance due to the non-ideality of the p-n junction and the impurities close to the junction.
- R_s is the series resistance due mainly to the strength of the volume of the material, interconnections and the resistance between metal contacts and semiconductors.

The circuit obtained is the 5-parameters model, represented in Figure 2.17.

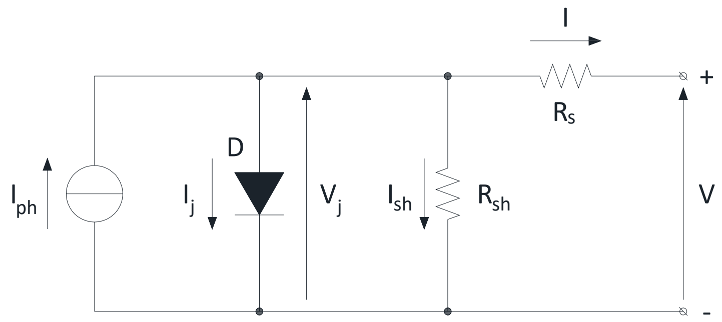

Figure 2.17: Five-parameters circuit model

An important parameter for defining the cell is introduced. The fill factor, FF, is a measure of the quality of the p-n junction and the cell resistances.

$$FF = \frac{V_{MPP} \cdot I_{MPP}}{V_{oc} \cdot I_{sc}} \tag{2.5}$$

Where:

- The numerator defines the point of maximum power (W)
- V_{MPP} is the MPP voltage (V)
- I_{MPP} is the MPP current (A)
- V_{oc} is the open circuit voltage (V)
- I_{sc} is the short circuit current (A)

The FF improves for high values of R_{sh} and for low values of R_s. On the one hand, the parallel resistance is related to the slope of the *I-V* curve around I_{sc}. The series resistance, on the other hand, is related to the pendant in V_{oc}. The higher the value that the fill factor assumes, the better the cell quality. In this case, R_s and R_{sh} have a not very significant influence. The influence of the resistances on the *I-V* curve can be seen graphically in Figure 2.18.

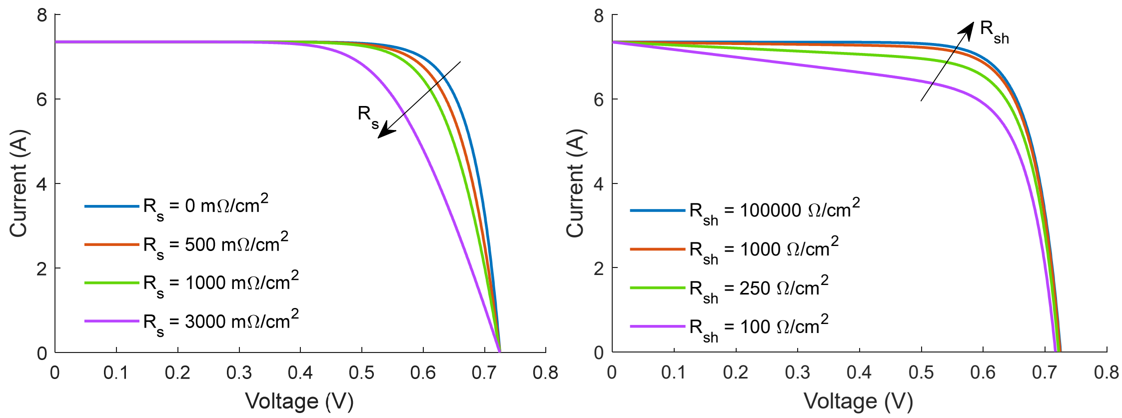

Figure 2.18: Dependence of the *I-V* curve on the parallel and series resistances

2.9. Analytical description

The circuit shown in the Figure 2.17 can be solved with respect to current and with respect to voltage.

In the first case the following calculation is obtained.

$$I = I_{ph} - I_j - I_{sh} \tag{2.6}$$

Where:

- I is the cell output current (A)
- I_{ph} is the photogenerated current (A)
- I_j is the current in the diode (A)
- $I_{sh} = \frac{V_j}{R_{sh}}$ is the current in the parallel resistance (A)

$$I_{ph} = q_e \cdot N_{ph} \cdot S \tag{2.7}$$

Where:

- $q_e = 1{,}602 \cdot 10^{-19}$ C is the charge of the electron
- N_{ph} is the number of incident photons in $(\mathrm{m}^{-2} \cdot \mathrm{s}^{-1})$
- S is the surface of the cell (m^2)

$$I_j = I_o \cdot \left(e^{\frac{q_e \cdot V_j}{n \cdot k_B \cdot T_c}} - 1 \right) \tag{2.8}$$

Where:

- I_o is the reverse saturation current of the diode (A)

- V_j is the voltage on the diode (V)
- n is the ideality factor of the diode
- $k_B = 1{,}38 \cdot 10^{-23}\ \mathrm{J \cdot K^{-1}}$ is the Boltzmann constant
- T_c is the p-n junction temperature (K)

The formula (2.9) is obtained by combining the previous ones.

$$I = I_{ph} - I_o \cdot \left(e^{\frac{q_e \cdot V_j}{n \cdot k_B \cdot T}} - 1 \right) - \frac{V_j}{R_{sh}} \tag{2.9}$$

Tension can be expressed with the following formulas.

$$V = V_j - R_s \cdot I \tag{2.10}$$

Where:

- V is the cell output voltage (V)

Obtaining V_j from (2.8) and replacing in (2.10)

$$V = \frac{n \cdot k_B \cdot T}{q_e} \cdot ln \left(\frac{I_{ph} + I_o - I - I_{sh}}{I_o} \right) - R_s \cdot I \tag{2.11}$$

The open circuit voltage is obtained when $I = 0$

$$V_{oc} = \frac{n \cdot k_B \cdot T}{q_e} \cdot ln \left(\frac{I_{ph} - I_{sh} + I_o}{I_o} \right) \tag{2.12}$$

Voltage and current equations can be combined substituting (2.10) in (2.9)

$$I = I_{ph} - I_o \cdot \left(e^{\frac{q_e \cdot (V + R_S \cdot I\,)}{n \cdot k_B \cdot T_c}} - 1 \right) - \frac{V + R_s \cdot I}{R_{sh}} \tag{2.13}$$

The short circuit current is obtained when $V = 0$

$$I_{sc} = I_{ph} - I_o \cdot \left(e^{\frac{q_e \cdot R_S \cdot I}{n \cdot k_B \cdot T_c}} - 1 \right) - \frac{R_s \cdot I}{R_{sh}} \tag{2.14}$$

Chapter 3

Optimization algorithms

Some generical concepts about the optimization are reported in this chapter. These concepts are useful to understand the bases on which the parameters extraction takes place.

Optimization algorithms aim to find a good approximation to the optimal value of a function in a large search space. This optimal value is called "global optimum". These research methods are meta-heuristic, so they use a tool to find out something with a strategy. There are two types of algorithms for solving optimization problems, based on deterministic methods or probability methods.

Firstly, in deterministic methods, the search strategy is identified by precise rules without random components. There are various techniques such as:

- Exhaustive search, where the number of solutions is known and it is possible to calculate all of them with a reasonable computation time;
- Branch and Bound techniques, where the number of solutions is known and it is possible to limit the number of calculated solutions by eliminating the cases that lead to worsening solutions;
- Iterative improvement, the strategy proceeds along a trajectory with subsequent changes until the procedure provides other changes;
- Tabu search, the strategy allows for finding a solution some solutions as "tabu moves" so as to avoid reaching them in a number of steps in the search process.

Secondly, in probabilistic methods, research evolves on the basis of random choices. There are various methods such as:

- Simulated annealing, simulation of the annealing process in which a melting metal is slowly cooled until it is solidified in its minimum energy state;
- Genetic algorithms, application of the principles of genetic evolution with reproduction by selection of the fittest elements, crossover and mutation;
- Honey bee optimization, inspired by bees behavior;
- Plant growth simulation, simulation of the effects of rapid plant growth towards the optimal direction of the light source

3.1. Levenberg-Marquardt algorithm

The Levenberg-Marquardt algorithm was discovered in 1944 [19] [20]. The Levenberg-Marquardt method (LM) is an indirect deterministic optimization algorithm. It is used for solving problems in the form of nonlinear least squares; LM commonly finds applications in curve fitting problems. LM is an iterative algorithm that strongly depends on the values of the initial parameters. In fact, the evaluation of the initial parameters is a fundamental step to determine the convergence or non-convergence of the algorithm. The iterative process aims to reduce the sum of the squares of the error between the (measured) points and the estimated function.

This method involves an interpolation between The Gradient Descent Method and The Gauss-Newton method which are two minimization methods. The former generates a variation of the parameters in the opposite direction with respect to the gradient, in order to minimize the objective function. The latter derives in turn from Newton's method, which develops an algorithm to meet approximations of the roots of a real function and therefore the minimum of a function. For nonlinear least square estimation problems, the Newton approach may be modified to originate a simple iterative algorithm. Unlike Newton's method, the Gauss – Newton algorithm does not need the second derivatives. The principle is based on a first-order Taylor series approximation of the nonlinear regression function, which is replaced in the nonlinear model. Therefore, a linear approximation which minimize a sum of squared function values is obtained.

The Levenberg-Marquardt undergoes a change of behaviors according to the context: on the one hand, it behaves more as the steepest-descent method if the parameters are distant from the global minimum, on the other hand, it behaves more as the Gauss-Newton method if the parameters are close to the global minimum.

The characteristic equation of the Levenberg Marquardt method is:

$$[J(p)^T J(p) + \lambda I]\delta = J(p)^T \cdot \big(y - \hat{y}(p)\big) \tag{3.1}$$

Where:

- J it is the Jacobian matrix
- p is the vector of n parameters (variables to be optimized for the algorithm)
- λ damping parameter
- I it is the identity matrix
- δ is the length of the calculated step
- y indipendent variable

- $\hat{y}(p)$ model curve

The λ factor is a control parameter because it determines the behavior of the algorithm. A low value of λ corresponds to a behavior close to the Gauss-Newton method, whereas a high value corresponds to moving the solution in a direction roughly opposite to the gradient, consequently with a behavior more similar to the method of descending the gradient. The value of λ is adapted to each iteration, increasing it if the previous iteration produced a limited reduction in the objective function, or diminishing it in case of rapid decrease.

3.2. Simulated Annealing algorithm

This method is inspired by the annealing process for steel and ceramic, a technique that consists in heating and then slowly cooling the material to vary its physical properties [21]. Heat causes atoms to increase their energy that can therefore move from their initial positions (a minimum local energy). Slow cooling offers atoms greater possibilities to recrystallize in configurations with less energy than the initial one (global minimum).

The Simulated Annealing algorithm (SA) is a probabilistic method based on an iterative process with two cycles, one external and one internal. The external cycle depends on a control parameter called c whose initial value is c_0.The iterations start from the known initial value f_{P_0} of the objective function aiming at a better configuration than that found up to that moment. At iteration m the control parameter decreases with a process given by $c_m = \alpha \cdot c_{m-1}$with the cooling rate α between 0 and 1. The typical values of this parameter vary between 0,95 and 0,98 because the algorithm requires a sufficiently slow variation.

Each iteration of the internal loop has the best configuration of the previous iteration as its initial configuration. At the end of the cycle a new configuration is obtained which becomes the new reference configuration, if it minimizes the objective function. The most considerable advantage of this method is that it allows you to perform a global optimization without being trapped in only paths that lead to local lows. This is achieved by ensuring that not only the configurations that leading to an improvement in the objective function are accepted, but also, with a probability to be defined, configurations that lead to a worsening of the objective function. Starting from the worse configurations, the new iterations are hoped to obtain others not otherwise achievable, which objective function is lower than the minimum found up at that moment. Accepting an increase in the objective function during the iterative process implies trying to get out of the local minimum condition and then converging into another local minimum, which is the absolute minimum for the system in question (in the luckiest of cases).

In summary, the configuration X_j^m, obtained at step j of the iteration m, is always accepted if the objective function $f_P^{'}$ is less than the minimum f_P^m obtained up to that point or it can be accepted even if it leads to a worsening $\Delta f_P = f_P^{'} - f_P^m$ in the objective function if a random number r, extracted from a uniform probability distribution in the interval (0,1), verifies the condition:

$$e^{\left(-\frac{\Delta f_P}{c^m}\right)} > r \tag{3.2}$$

From analyzing the formula, it can be observed that the probability of acceptance of a worsening decreases, assuming that the same value of r has been extracted, as the control parameter decreases, consequently contributing to the convergence of the method. Two criteria are used to establish the end of an iteration, which set the maximum values for the number of configurations accepted during the iteration (M_C)and analyzed (M_A). As a stopping criterion, the whole algorithm ends when the objective function does not change for a predefined number of successive iterations.

3.3. Nelder-Mead algorithm

The Nelder-Mead method (NM) [22] also known as the simplex method, is a direct deterministic optimization algorithm. This method has the purpose of minimizing the objective function in a multidimensional space. The method does not use derivatives and is based on the concept of simplex, a particular type of polytope with $n + 1$ vertices in an n-dimensional space. Polytope is a generic geometric unit with "flat" sides connected each other to form a closed line. Examples of simplexes are a segment in a straight line, a triangle in the plane, a tetrahedron in space.

At the iteration of m, the algorithm examines a new polytope obtained from the previous iteration of $m - 1$. In this analysis, the behavior of the objective function is evaluated at each point of the domain at the vertices of the simplex. The algorithm then chooses the point at which the objective function takes the worst value. This point is replaced with a new point. The simplest case is to replace the farthest point from the optimum with the center of gravity of the remaining n points: if the evaluation in the new point is better than the current point, the search goes on with an exponential trend in the direction identified by the point, otherwise it is sought in the direction of a point that provides a better rating. The method approximates the local optimum point of a problem in n variables when the objective function is smooth and unimodal. Like other optimization algorithms, Nelder-Mead sometimes gets stuck at the local minimum (an area that is a minimum function compared to the surrounding points, but it is thought that there is a better minimum elsewhere). The algorithm takes note and restarts with a new simplex having the best value found as initial configuration. The stop criterion used by Nelder and Mead is the sample standard deviation of the values of the function of the current simplex. If the value obtained is lower than the set tolerance, the cycle stops. In this case, the optimal point returned by the analysis is the lowest point of the simplex. In the case of a very flat function, the solution is very sensitive to the tolerance set: in fact, it is possible to have almost equal function values on the domain.

There are several variations of the method, depending on the nature of the problem to be solved. A common technique involves the use of a small simplex of constant amplitude which roughly follows the direction of the gradient (which represents the direction of maximum variation of the function).

Chapter 4

Automatic data acquisition system

The way in which the *I-V* curve of the PV modules under study was measured is going to be explained and described in this chapter. Firstly, the *I-V* curve measurement principle will be described. Then, the measurement system adopted will be explained in detail and the evaluation of the measurement uncertainty will be computed in the last section.

4.1. *I-V* curve measurement principle

In principle, to record the *I-V* curve of a photovoltaic generator is necessary to connect the PV module under study to a variable load [23]. For example, this variable load could be implemented by a variable resistor. This one must be variable due to the necessity of measuring different working points, assuming PV module as a current generator. Another way to force the variation of the output impedance connected to the PV module is obtained thanks to the charging transient propriety of a capacitor. Also, one voltmeter and one ammeter are necessary to measure the voltage and current at the output terminals of the PV module, respectively. In Figure 4.1 a simple schematic of a basic measurement system is represented.

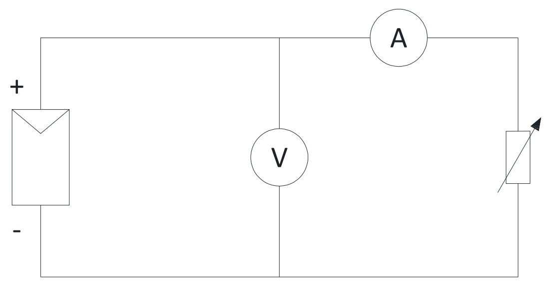

Figure 4.1:Basic schematic of *I-V* curve measurement system

According to technical specification generally recognized, the proper tracking of an appropriate *I-V* curve implies measuring at least 100 points *I-V* in a process lasting a time ranged between 20 and 100 ms [23]. In this way, the variation in weather conditions does not affect the measure of the *I-V* curve.

4.1.1. Capacitive load

An alternative solution is the usage of a capacitor that avoids the issue of sinking the heat generated by the resistor during the test. Then, the capacitor can manage a wide range of voltage, current and power signals, because the signals last for short time: the transient charge lasts usually for less than 1 s. The charging transient of a capacitor is the simplest method that can be used to trace the *I-V* curve [24]. In fact, the charging time of the capacitor can be defined by the following differential equation:

$$i(t) = C \cdot \frac{dv(t)}{dt} \tag{4.1}$$

Where:

- $i(t)$ is the current (A) flowing in the capacitor
- C is the measured capacitance (F)
- $v(t)$ is the voltage (V) across the capacitor

Supposing that the capacitor is totally discharged, the voltage and current evolve from short circuit condition into open circuit condition when the switch is closed. The charging time (t_c) could be defined as the time for a voltage sweep from 0 up to the 99,33% of the V_{oc} , which represents the final charging voltage. Current and voltage at terminals of the capacitor are represented as function of time, as shown in Figure 4.2.

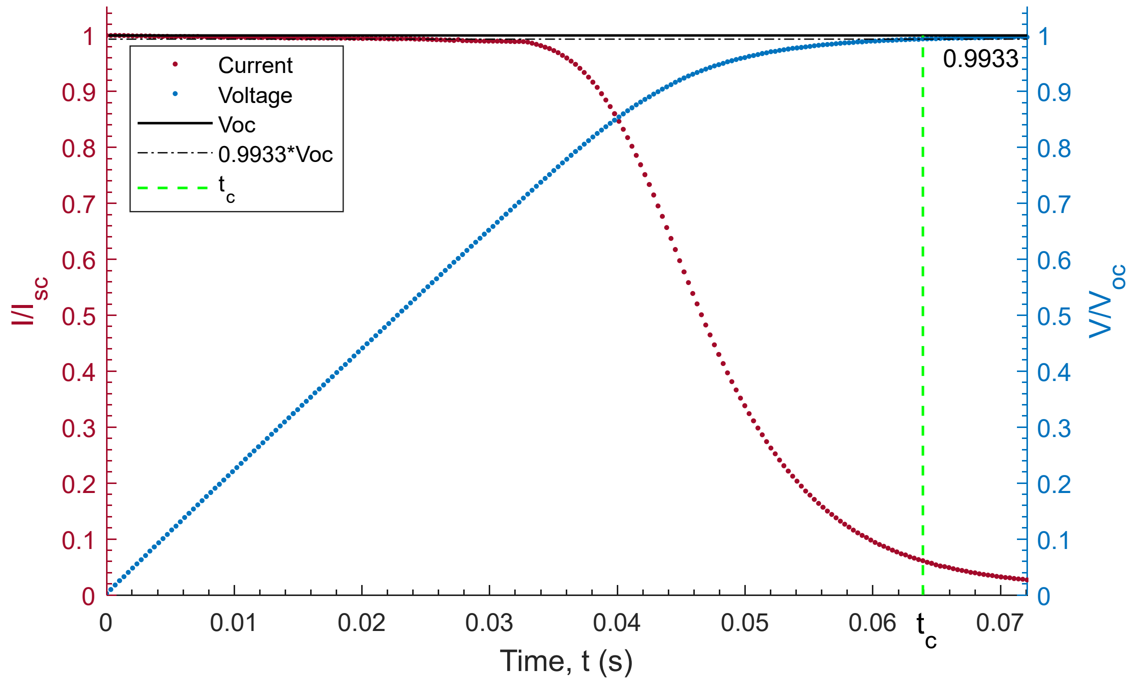

Figure 4.2: Charging transient of a capacitor connected with a PV module.

The charging time of the capacitor is mainly related to the module irradiance and temperature. As can be seen in [25], the charging time can be evaluated looking at the short circuit current and open circuit voltage with the following expression:

$$t_c = \frac{C}{A} \cdot \frac{V_{oc} \cdot N_s}{I_{sc} \cdot N_p} \tag{4.2}$$

Where:

- t_c is the charging time of the capacitor (s)
- $A = 0{,}55$ is the proportionality factor (-)
- V_{oc} is the open circuit voltage (V)
- I_{sc} is the short circuit current (A)
- N_s is the number of cells in series (-)
- N_p is the number of cells in parallel (-)

The charging time is the most difficult and essential parameter to estimate because it determines the correct synchronization of the multimeters and it allows to properly set the reading rate. Therefore, the charging time has to be estimated before acquiring the *I-V* curve. This estimation may be performed from the measure of the module irradiance and temperature. These two weather conditions influence the short circuit current and the open circuit voltage, respectively.

4.2. Description of the measurement systems

The measurement systems used to acquire the data for this thesis, are located on the roof of the laboratory of solar energy in the "Escuela Politécnica Superior - Universidad de Jaén". The laboratory is equipped with two different systems having similar configuration. On one hand, the description in this chapter involves both because the Graphical User Interface (GUI) is developed to work with both systems. On the other hand, the data analyzed in this thesis come only from one measurement system. The main difference between the two systems is the placement of PV module. They are called respectively "Tracker system" and "Fixed system" because the former uses a 2-axes tracker and the latter uses a fixed structure. Their task is to collect *I-V* curves in long experimental campaigns. Meanwhile, meteorological parameters are gathered in the same file. The *I-V* curves are recorded automatically every few minutes during all year, following the user's settings (e.g. 5 min). The behavior of photovoltaic modules under outdoor conditions can be analyzed using this information. In the following section the working principle of the measurement systems will be explained. Firstly, the common features are presented, then, the details of each system will be clarified.

4.2.1. Global description of the two systems

The systems are designed to sequentially acquire the *I-V* curve from four different modules and the weather conditions. This is important to conduct experimental campaigns when more than one module has to be measured at the same time. The schematic of the two measurement systems is illustrated in Figure 4.3. The common characteristics are represented in light blue while the peculiar characteristics are marked in violet for the tracker system and in orange for the fixed system, respectively. Both systems adopt a capacitive load to trace the curve, the tracker system uses a handmade one while the fixed system adopts a commercial equipment. Also, the external trigger used to synchronize the multimeters is different. This signal comes from the Agilent 34970A datalogger for the tracker system while it comes from an Agilent 33220A signal generator for the fixed system.

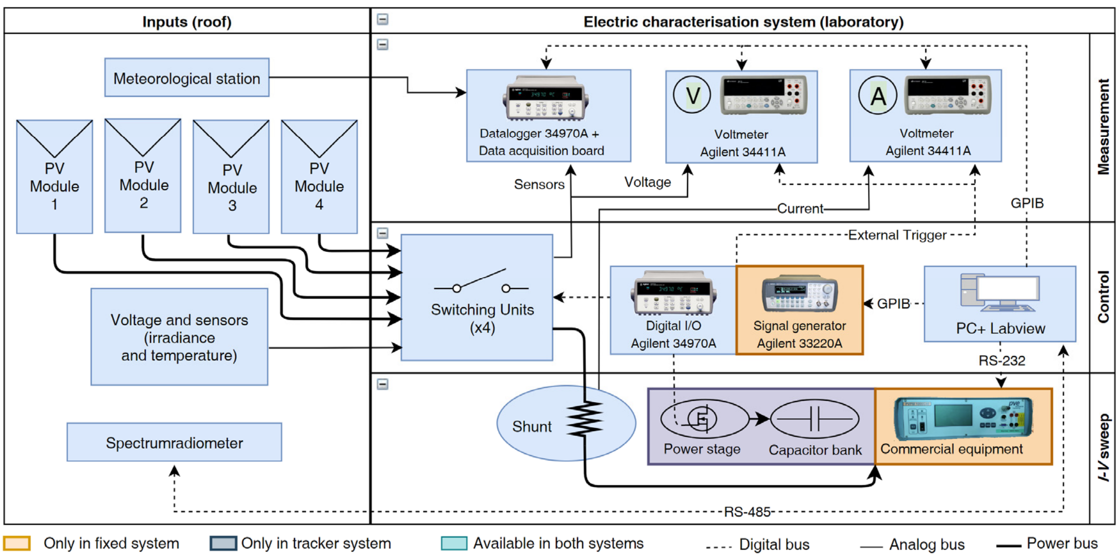

Figure 4.3: Global scheme of the measurement systems

The systems are physically divided into two sections, as in Figure 4.3. The first portion is located outside, on the roof just over the laboratory. Whereas the second one is located inside the laboratory.

Firstly, the roof portion mainly includes the PV module, the holding structure, the sensors and five connection boxes. The first four boxes are containers, one for each module, named "module boxes". An additional "join box" is responsible for merging the cable coming from the module boxes, as in Figure 4.4.

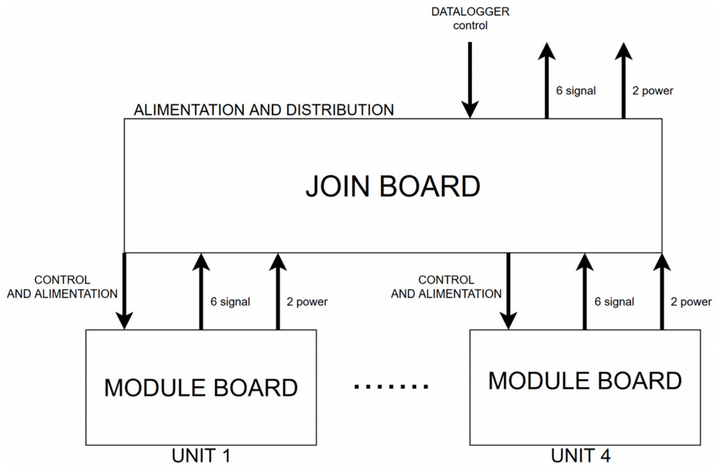

Figure 4.4: Scheme of the switching units

An electronic board is installed inside each module box, as shown in Figure 4.5. That component was designed by the IDEA research group of the University of Jaén. The connection of the module and the temperature probe to the measurement instrumentation is the main purpose of control. This board consists essentially of relays with the control circuit, that enables the connection to the instruments in the laboratory. The board has two "power" connections as input to link the module to the load (capacitor or electronic), one for the positive pole and the other for the negative one. Moreover, the circuit has four inputs, used to connect the Pt100 temperature sensor for a 4-wires resistance measure. Also, the electronic board has two inputs to directly acquire the voltage from the module terminals. This is necessary to avoid the influence of voltage drop due to the wires' resistance. Likewise, the control signal and the power supply from the equipment placed in the laboratory are received as inputs.

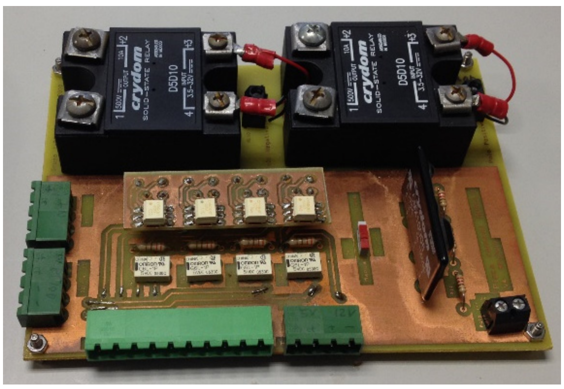

Figure 4.5: Picture of the multiplex board of each module

The electronic board in Figure 4.6 is mounted inside the "join box". This electronic circuit firstly receives the wires from the four "module boxes" and, secondly, it merges them with the line that goes down in the laboratory. This electrical link is made by two power cables, which carry the generated current to the load, and one 18-wire cable, for the signal and control.

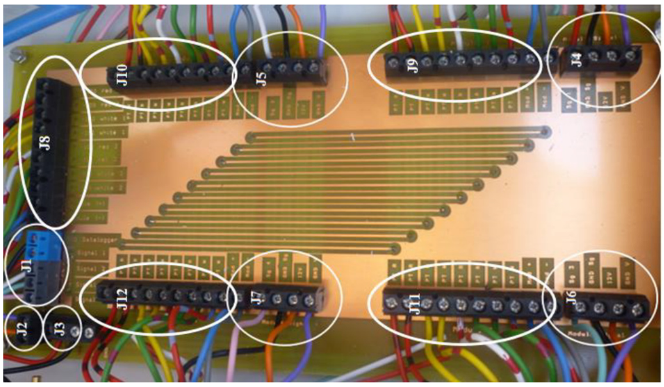

Figure 4.6: Picture of the join board [26]

Secondly, the other section of the system is placed in the laboratory where the measurement equipment is located. There are two Agilent 34411A multimeters in the systems: one measures the voltage coming from the module terminal and the other measures the voltage drop across a shunt resistor to calculate the current. The shunt resistor is a KAINOS 10A-150mV of [1]class 0,5. These two multimeters are controlled by a trigger signal to synchronize the acquisition of voltage and current. The source of the trigger signal varies according to the two measurements systems. Also, a datalogger Agilent 34970A is used to control the system and acquire measures on weather condition. It is relevant to mention that this device has three slots: one of them is equipped with an Agilent 34907A while the other two slots are equipped with the Agilent 34901A cards. The Agilent 34907A Digital Multifunction Module provides the control signal and selects the module under measure. On top of that, the two Agilent 34901A cards are composed of 20 measuring channel each and are included to acquire the analogical signal from the weather sensors.

[1] The class of a resistor is the deviation of the resistive value with respect to the nominal one. In this case, class 0,5 means 0,5% of deviation.

4.2.2. LabVIEW program

The entire system is managed with an ad-hoc LabVIEW software on a dedicated PC. The devices are attached to the PC through GPIB connections, except for the spectroradiometer that needs a RS485-RS232 serial connection.

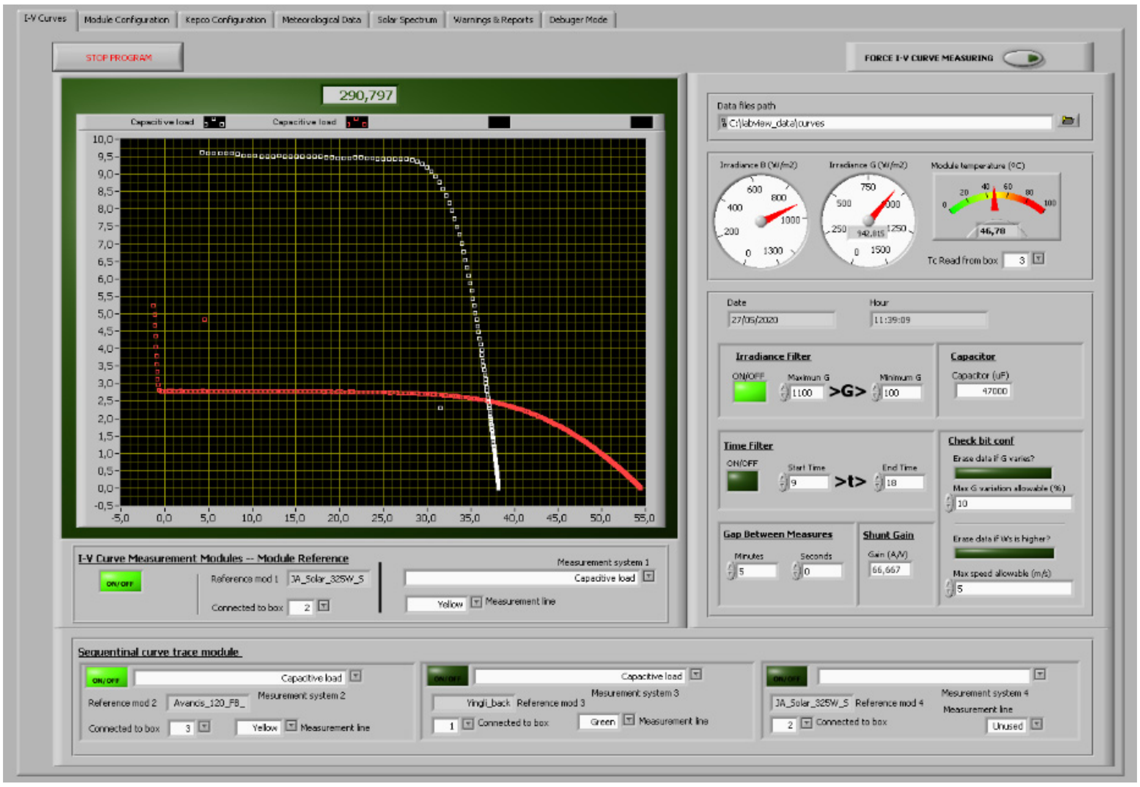

Figure 4.7: LabVIEW graphical user interface of tracker system (*I-V*-curve tab)

The LabVIEW software operation is represented in the flowchart Figure 4.8. Moreover, the software is designed to provide the user with extra facilities to configure the measurement process. In addition, the graphical interface shows in real time the acquired data such as the *I-V* curves, the value of irradiance and temperature or the shape of the solar spectrum. A snapshot of the software's user interface is shown in Figure 4.7. The program saves as output the data from different sensors and instruments in one "CSV" file for each acquisition. The output CSV file is structured with one column for each measured quantity. All columns contain 1500 values, forming a matrix. All 1500 values are equal in case of a physical quantity with a single point (i.e. temperature, irradiance, etc.).

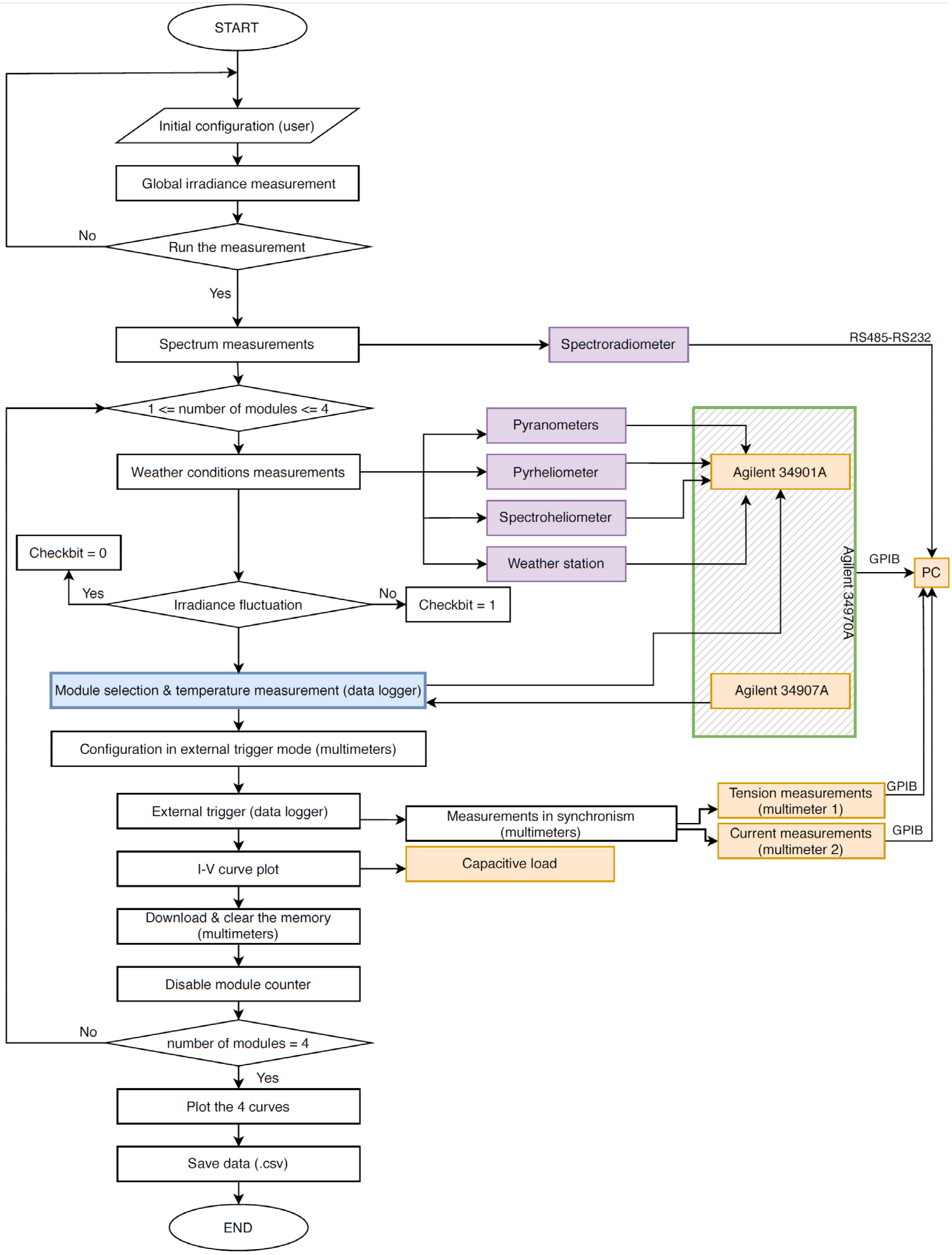

Figure 4.8: LabVIEW measurement control software flowchart

4.2.3. Weather station measurement sensors

The instruments used to measure the weather conditions will be described in this section. All sensors are connected to the two Agilent 34901A 20-Channel General Purpose Multiplexer boards included in Agilent 34970A datalogger. The instruments the system is equipped with are described in the following lines. The description includes all the instruments because the Graphical User Interface (GUI) is developed to read all the measures from each one of them. However, not all the instruments are used for the elaboration and simulation of this master thesis research project.

4.2.3.1. Measurement of module temperature (T_c)

As regard the measure of the module temperature (T_c), a resistance temperature detector (RTDs) of the Pt100 type with 4-wire connection is adopted. This sensor consists of a probe made of platinum (Pt) with a 100 Ω resistance at 0 °C. The temperature coefficient "α_{Pt100}" of this sensor is $0{,}00385\ \Omega \cdot \Omega^{-1} \cdot K^{-1}$. This coefficient describes the linear approximated characteristic of the probe resistance variation with temperature:

$$\alpha_{Pt100} = \frac{R_{100} - R_0}{100 \cdot R_0} \tag{4.3}$$

Where:

- $\alpha_{Pt100} = 0{,}00385\ \Omega \cdot \Omega^{-1} \cdot \mathrm{K}^{-1}$ is the temperature coefficient
- R_{100} is the sensor resistance at 100 °C measured (Ω)
- R_0 is the sensor resistance at 0 °C measured (Ω)

The temperature value is calculated by a measurement of the resistance of the Pt sensor in a 4-wire configuration. A 4-wire measurement is precise and unaffected by the length of the laboratory wires. The datalogger is set properly to make the conversion. The selected probe works for temperature ranged between -50 °C and +150 °C.

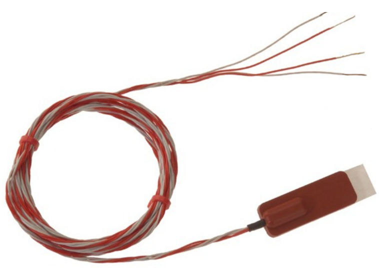

Figure 4.9: Picture of the Pt100 probe to record the PV module temperature

4.2.3.2. Measurement of global in-plane irradiance (GTI or G)

The global in-plane irradiance (GTI or G) represents the global solar power per unit of area received by a surface with an azimuth and zenith angle. Essentially the GTI is composed of the direct and diffuse radiation components. The GTI is measured by a Kipp and Zonnen CMP11 pyranometer, as in Figure 4.10. The instrument is placed co-planar with the modules under study. The pyranometer provides an output voltage signal proportional to the incidental irradiance. Moreover, this voltage signal can be converted in irradiance units with the calibration constant. This calibration constant came from the manufacturer calibration or from external calibration in an accredited laboratory (i.e. CIEMAT in Madrid). The output signal from the pyranometer is measured with the datalogger.

The global normal irradiance (GNI) represents the total solar power per unit of area received on a surface perpendicular to the sun beams. In the case of the tracker system the measured GTI corresponds to the GNI because the tracker stands always perpendicular to the sun.

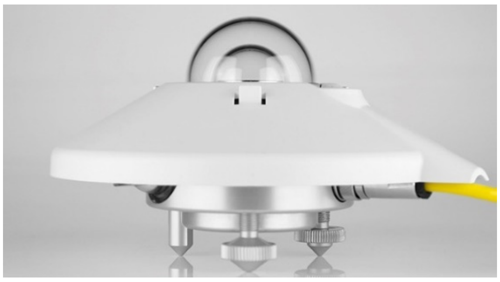

Figure 4.10: Picture of the Kipp and Zonnen CMP11 pyranometer

4.2.3.3. Measurement of global horizontal irradiance (GHI or G_h)

The global horizontal irradiance (GHI or G_h) represents the global solar power per unit of area received by a horizontal surface. The GHI is measured with a Kipp and Zonnen CMP11 pyranometer as the device shown in Figure 4.10. As described in 4.2.3.2, the sensor provides a voltage output signal proportional to the GHI. Then this voltage signal is measured by the datalogger.

4.2.3.4. Measurement of direct normal irradiance (DNI or B)

The direct normal irradiance (DNI or B) represents the direct solar power per unit of area received by a perpendicular surface to the sun beams (normal to the sun). The DNI is measured with a Kipp and Zonnen CHP1 pyrheliometer as shown in Figure 4.11. The instrument is mounted on the tracker system. It is worthwhile to mention that only the solar tracker is equipped with this instrument. This is because the tracker is planned to measure concentration solar modules and the sensor of B is pivotal for this technology. The sensor provides as output a voltage signal linearly proportional to the DNI. The signal is measured by the datalogger.

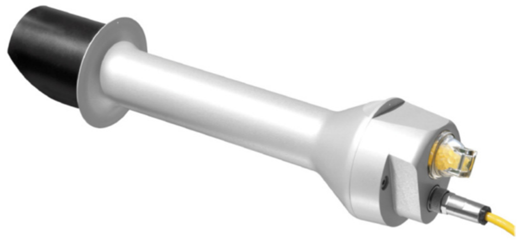

Figure 4.11: Picture of the Kipp and Zonnen CHP1 pyrheliometer

4.2.3.5. Measurement of the spectral irradiance ($F(\lambda)$)

The spectral irradiance ($F(\lambda)$) represents the power per surface unit as a function of the photon wavelength. A typical distribution of spectral irradiance can be seen in Figure 4.12. The spectral irradiance is important because the electrical response of a PV module varies with it. The spectral irradiance is measured with the EKO MS-700 spectroradiometer, as shown in Figure 4.13. The instrument measures the spectral irradiance in the range 350-1050 nm and it sends directly to the PC the information through a RS-232 serial connection.

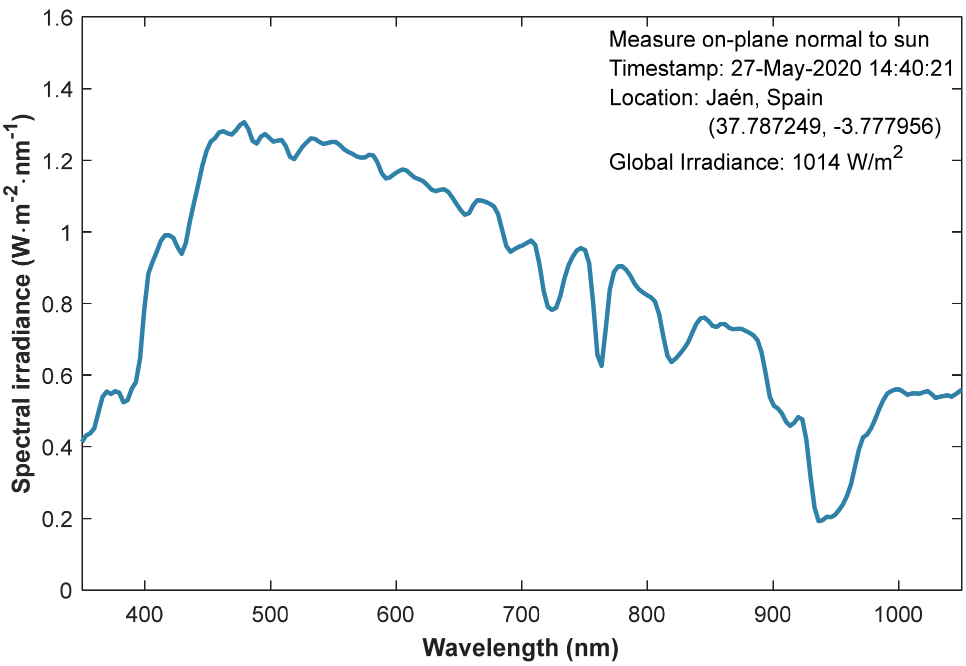

Figure 4.12: Spectral irradiance distribution measured by EKO MS-700

Figure 4.13: Picture of Eko MS-700 spectroradiometer

4.2.3.6. Measurement of the triband irradiance

The Tri-band spectro-heliometer from IES-UPM, shown in Figure 4.14, measures the effective irradiance in the spectral zones corresponding to the top, middle, and bottom sub-cells of a lattice-matched GaInP / GaInAs / Ge triple-junction solar cell. This instrument is useful to conduct experimental campaigns about concentrator photovoltaics. The sensor provides as output a voltage signal linearly proportional to the band irradiance measured by the datalogger. Only the solar tracker is equipped with this instrument.

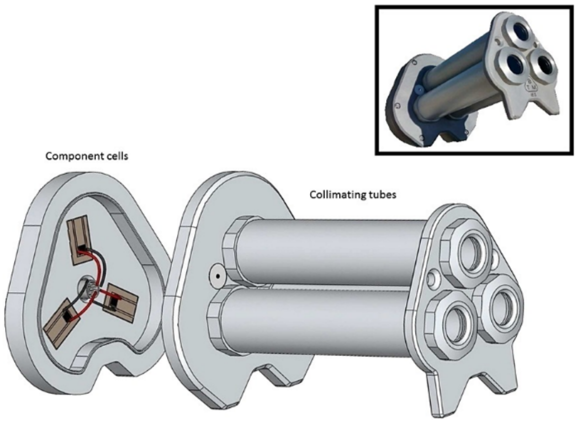

Figure 4.14: Picture of Tri-band spectro-heliometer from IES-UPM [27]

4.2.3.7. Measurement of the wind speed (WS) and wind azimuth direction (WD)

The wind speed (WS) and wind azimuth direction (WD) are measured with a Young 05305VM anemometer in Figure 4.15. The device provides two output-voltage signals linearly proportional to the measured WS and WD. The datalogger is used to measure those signals.

Figure 4.15: Picture of Young 05305VM anemometer

4.2.3.8. Measurement of the ambient air temperature (T_a) and relative humidity (RH)

The ambient air temperature (T_a) and relative humidity (RH) are measured with a Young 41382VC temperature and relative humidity probe as in Figure 4.16. The instrument delivers two output-voltage signals linearly proportional to the measured air temperature and relative humidity. The datalogger is used to measure those signals.

Figure 4.16: Picture of Young 41382VC temperature and relative humidity probe

4.2.3.9. Measurement of the atmospheric pressure (p_{amb})

The atmospheric pressure (p_{amb}) is measured with the Vaisala BAROCAP PTB110 barometer as in Figure 4.17. The device provides as output a voltage signal proportional to the atmospheric pressure.

Figure 4.17: Picture of Vaisala BAROCAP PTB110 barometer

4.2.4. Tracker system details

The "tracker system", shown in Figure 4.18, uses a BSQ D150/6 Solar 2-axes tracker. The system is designed with a 2-axis solution to hold the PV module perpendicularly always to the direct sun light. The tracker is designed to carry out activity on concentration solar with a maximum misalignment of ±0,5°. In this way, the possible angular reflection losses are avoided. Furthermore, the system works as described in 4.2.1 and only the main difference will be reported here. This system integrates all instruments introduced in the previous section, that are module temperature probe, on-plane and horizontal pyranometers, pyrheliometer, spectroradiometer, tri-band spectro-heliometer, anemometer, air temperature and relative humidity probes, and barometer. In addition, the two multimeters are synchronized by the Agilent 34970A datalogger that provides a trigger signal through the Agilent 34907A Digital Multifunction Module. Moreover, the datalogger commands the connection of one of the four modules under test by the switching units in Figure 4.3.

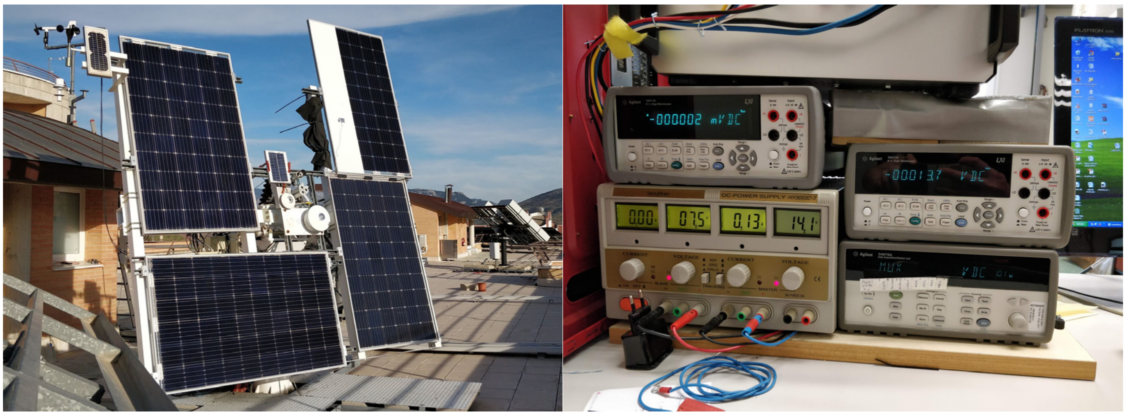

Figure 4.18: Picture of tracker system
(on the left the external part, on the right the internal equipment)

As regards the implemented load to plot the *I-V*-curve, the system includes a capacitive load as shown in Figure 4.19. This load mainly consists of three elements: the first one is the electrolytic capacitor with a capacitance of 47 mF and a maximum voltage of 100 V; the second one is the discharge resistance which is used to discharge the capacitor; finally, The last one is a voltage generator used to negative pre-charge the capacitor and to get the short circuit current.

Figure 4.19: View of the inside of the capacitive load

The working principle of the load is described as follows. The Agilent 34970A datalogger controls the charge and discharge of the capacitive load using relays. Firstly, the datalogger closes only SW7, shown in Figure 4.20, to negative pre-charge the capacitor. This process is essential to get the short circuit current point. Besides, a diode is necessary to avoid problems linked to the internal diode of the solid-state relays. Further information can be found in [28].

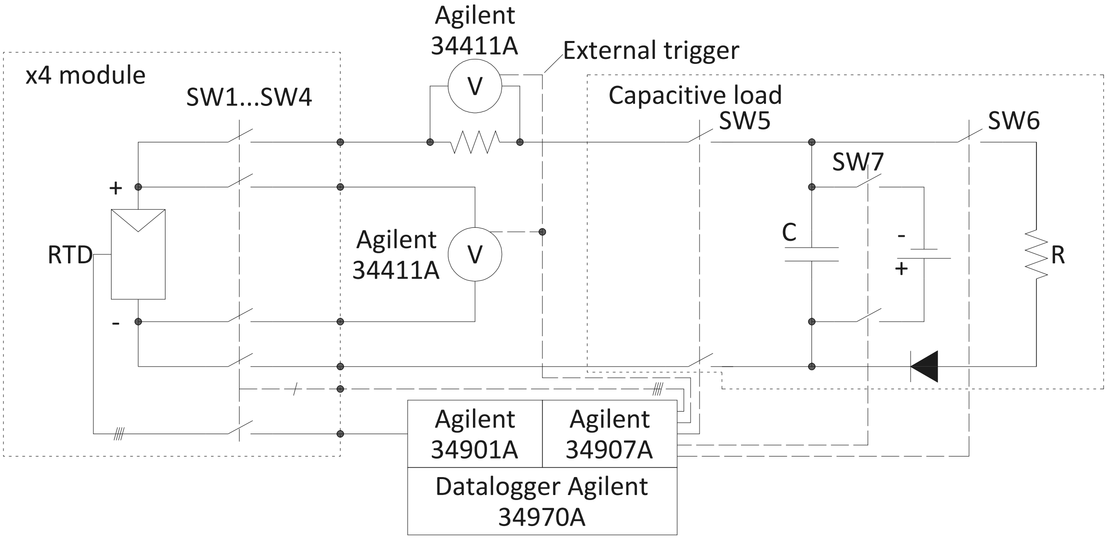

Figure 4.20: Electrical scheme of the tracker system

Secondly, always with reference to Figure 4.20, the datalogger opens SW7 and then it closes SW5. This sequence of commands connects the PV module to the capacitor load C. Then, the multimeters may acquire the voltage and current synchronously. The data acquisition is done in a specific time referred to the capacitive load properties. In fact, the estimation of the charging time (t_c) is essential to meet the timing requirement according to 4.1. This evaluation is done according to eq. (4.2). The time between two samples is settled properly for acquiring the entire curve with enough points.

Finally, the datalogger reopens SW5 at the end of the transient and it closes SW6 to discharge the capacitor on a resistor for the next acquisition.

4.2.5. Fixed system details

The modules are placed on a fixed structure, shown in Figure 4.21, oriented with 0° zenith and a 35° tilt angles. The system works as described in 4.2.1 and the/its main components will be reported in the following lines. This system integrates the module temperature probe, on-plane and horizontal pyranometers, spectroradiometer, anemometer, air temperature and relative humidity probes, and barometer. Furthermore, the two multimeters are synchronized by an Agilent 33220A signal generator. The way in which *I-V* curve is traced in the system is the feature which makes the fixed system remarkably different from the tracker system. In this sense, a commercial *I-V* curve tracker based on a PVE PVPM 2540C controlled by the LabVIEW program is used in this measurement system. The LabVIEW software communicates directly with the *I-V* curve tracker through an RS232 link.

Figure 4.21: Picture of fixed system
(on the left the external part, on the right the internal equipment)

4.3. Evaluation of uncertainty on measure

The uncertainty analysis is important because it allows to compare the theoretical model to the experimental results. The uncertainty interval should be compared with the theoretical model to quantify the accuracy of the results. The calculated tolerances for the worst scenario are reported in this section. The worst scenario indicates the case in which the relative tolerance ($\boldsymbol{U_{x,worst}}$) is the highest. The adopted methodology is described in the Annex B. Table 4.1 shows the worst-case uncertainty according to [29].

Measurands	$\boldsymbol{U_{x,worst}}$ **(%)**
Voltage	±0,02
Current intensity	±1,0
GTI and GHI	±2,0
Module temperature	±1,16
Wind speed	±0,66

Table 4.1: Resume of the worst case uncertainty

Chapter 5

Processing of experimental data (GUI)

The MATLAB software made up to elaborate this thesis will be presented in this chapter. The application projected aims at processing automatically the large amount of data acquired by the measurement systems, described in Chapter 4. The program is designed with the use of MATLAB App Designer tool to achieve a simpler interface. The graphical user interface (GUI) is divided into several tabs. Each tab handles separately one section of the process. This separation is done in order to have the possibility of looking at the partial result of each part. Also, this segmentation allows to reuse part of the interface to execute other tasks. The next four chapters deal separately each GUI's tab. Figure 5.1 shows the flows of these four tabs.

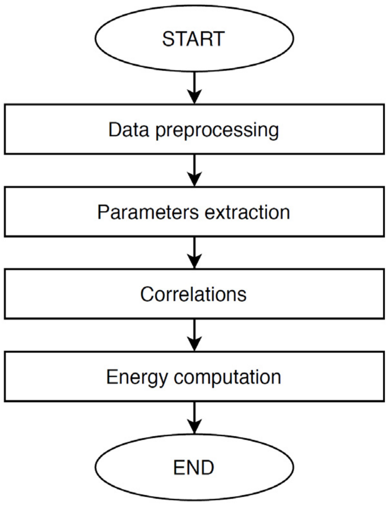

Figure 5.1: Flowchart of the four step of the GUI

First, the data preprocessing will be described. This step consists in the reading and filtering of the raw data. Then, the parameters extraction procedure will be explained. This step consists in the search with the optimization algorithms, used to find the parameters of the model that describes the system. After that, the extraction of correlation coefficient will be clarified. This step consists in the search for irradiance and temperature trends. Last, the energy estimation will be proposed. This step consists in the estimation of power in a bigger set of data, in order to validate the correlation model.

The GUI and the software are developed by the support of the following MathWorks products and toolboxes:

- MATLAB
- App Designer
- Curve Fitting Toolbox
- Parallel Computing Toolbox
- Predictive Maintenance Toolbox
- Signal Processing Toolbox
- Statistics and Machine Learning Toolbox
- System Identification Toolbox

The useful terms in the App Designer description are defined in the MATLAB manual and here are reported:

- “Button” is a component that responds when the user presses and releases it
- “Check Box” is a component indicating the state of a preference or option
- “Drop Down” is a component that enables the user to select an option or type in the text
- “Edit Field” is a component that allows the user to type numeric/text values
- “Button Group” is a component that allows the user to choose one button from the set
- “Text Area” is a component necessary to enter for entering multiple lines of text
- “Tab Group” is a container for grouping and managing tabs
- “Panel” is a container for grouping other components together
- “Switch” is a component indicating a logical state
- “Lamp” is a component that reporting the state using color

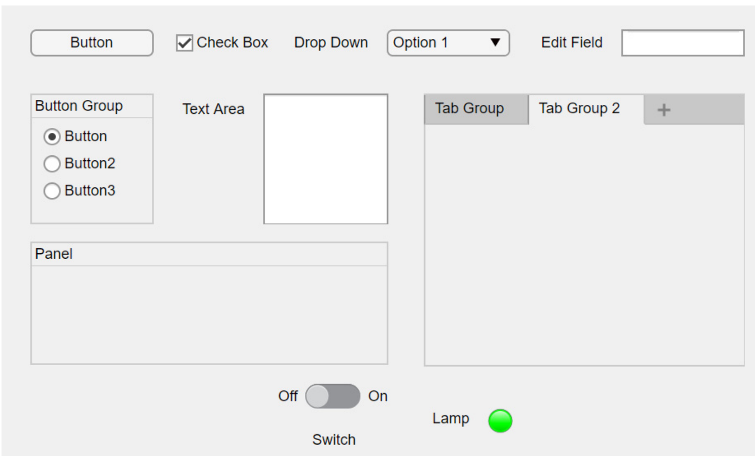

Figure 5.2: MATLAB App Designer useful components

Chapter 6

Data preprocessing

The data preprocessing consists of reading CSV files from the measurement system and removing the problematic measurement automatically. Then, some filters are implemented to fulfill this task. The graphical interface and the software operation are presented in the next two sub-chapters.

6.1. Graphical interface for data preprocessing

The graphical interface is designed to contain all the needed settings in the most intuitive way. Figure 6.1 shows the interface when the program is open.

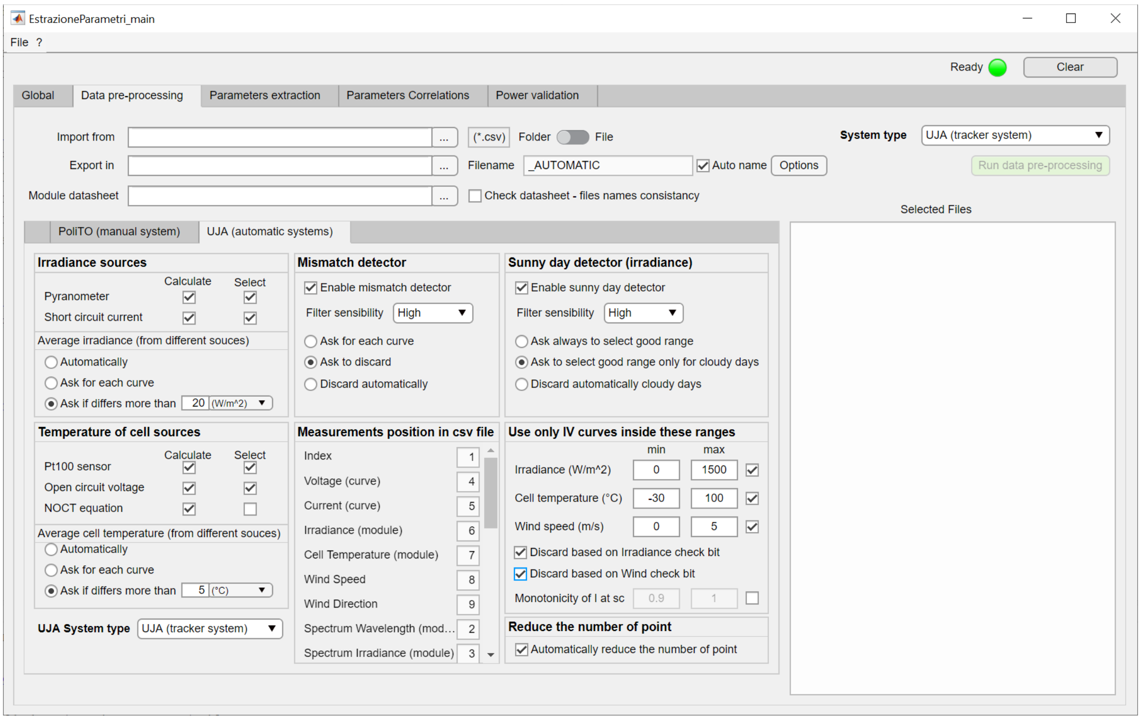

Figure 6.1: Picture of the graphical user interface tab for the preprocessing task

Figure 6.1 may be divided into two sections. The first illustrates the import and export settings; the second is "UJA (automatic system)". A third section can be observed, "PoliTO (manual system)". However, this section is not described because this thesis only processes data from the Spanish university.

6.1.1. Import and export settings

The import and export settings are situated in the upper part of the interface. Three edit fields and a list box may be seen. They are described in the following lines.

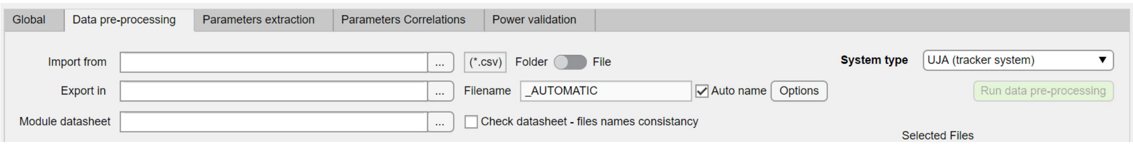

Figure 6.2: Picture of the graphical user interface for the preprocessing task-import and export settings

On the one hand, the first edit field allows the user to select the file path. There are 2 types of input selection, i.e. the choice of a group of files or of an entire folder. Only the CSV files are picked up in case of in the case of a UJA system.

On the other hand, the second element allows the user to choose the data export folder in the desired format. The format selection can be made by clicking the “Options” button present in the same line as the second edit field. The options button opens a new window, shown in the Figure 6.3 and described in the following lines.

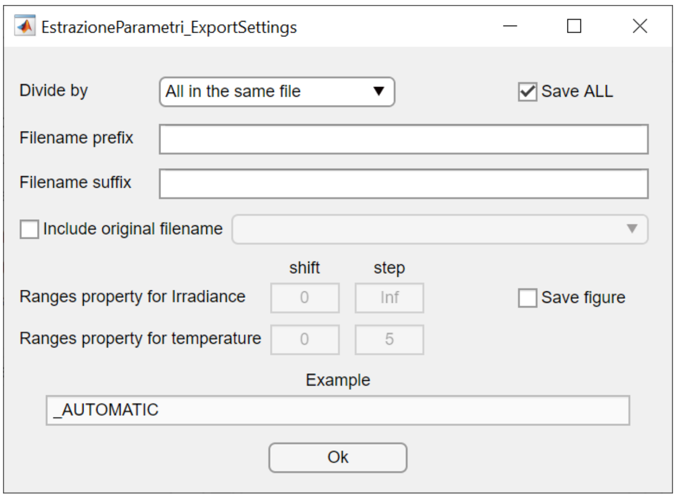

Figure 6.3: Picture of the window for selecting the saving properties

The saving settings in the list box permits to divide the data in various ways. There are different types of data division: “All in the same file”, “Divide by days”, “Divide by months”, “Divide by years”, ‘’Divide by irradiance”, “Divide by temperature (module)”, "Divide by irradiance and temperature (module)". The selection of saving data by irradiance and/or temperature involves a further specification called "the ranges property". Here, the user has to insert two values for quantity: an initial shift value from zero and a step value. The ranges division is created only between the minimum and maximum rounded values of the quantity. An example for the irradiance case with shift = 25 and step = 50 means the division of the irradiance in the ranges (0-25], (25,75], (75,125], …, (975,1025].

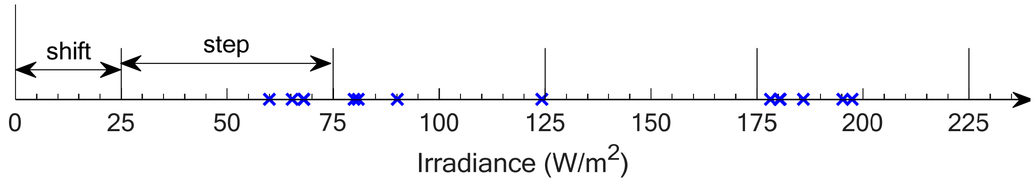

Figure 6.4: Example of ranges division

If there is only one measure with $G = 1000\,\mathrm{W \cdot m^{-2}}$, the ranges division results in (975,1025]. The same logic is adopted for the module temperature classification. In the options window, there are two optional edit fields that allow the user to insert a prefix and a suffix to the name of the output data. Moreover, in the final file name, the user can also decide to include the original filename of the CSV file. Finally, two checkboxes can be seen. On the one hand, the "Save ALL" checkbox keeps a copy of all loaded information before applying the filters. On the other hand, the "Save figure" checkbox saves the figures of the day irradiance and the *I-V* and *P-V* curves of each acquisition.

The third edit field of the import and export settings is the selection of the Excel datasheet files. This Excel file shall be created with a proper model as in Figure 6.5.

	A	B	C	D
1		**Value**	**Unit of measurement**	**Notes**
2	module name	Sanyo_HIT240HDE4	-	Must finish with '_'
3	$P_{max,STC}$	234,37	W	Power MPPT in STC conditions
4	$I_{sc,STC}$	7,54	A	Short circuit current in STC conditions
5	$V_{oc,STC}$	42,39	V	Open circuit voltage in STC conditions
6	α (I_{sc})	0,030	%/K	Coefficiente di temperatura Isc
7	β (V_{oc})	-0,250	%/K	Coefficiente di temperatura Voc
8	γ (P_{max})	-0,300	%/K	Coefficiente di temperatura Pmax
9	NOCT	45	°C	NOCT temperature
10	Ns	60	-	Number of cell in series
11	Nc	1	-	Number of cell in parallel
12	Cell dimension	125	mm	
13	G_{STC}	1000	W/m^2	Irradiance in STC conditions
14	Tc_{STC}	25	°C	Cell temperature in STC conditions
15	G_{NOCT}	800	W/m^2	Irradiance in NOCT conditions
16	Ta_{NOCT}	20	°C	Air temperature in NOCT conditions

Figure 6.5: Picture of the module datasheet in Excel. The data are for the Sanyo HIT module s/n POHA8FA28569 from the 2011 CIEMAT calibration

Eventually, the last element of the import and export settings is the "System type" list box. The user declares the measurement system used between the PoliTO instrumentation, not used for this thesis, and the UJA ones.

6.1.2. Implemented data preprocessing for UJA (automatic system)

The UJA (automatic system) is situated in the lower part of the interface. The settings are grouped in seven panels. These panels will be described starting from the ones involved in the data acquisition. Then, the ones involved in the filtering process are presented.

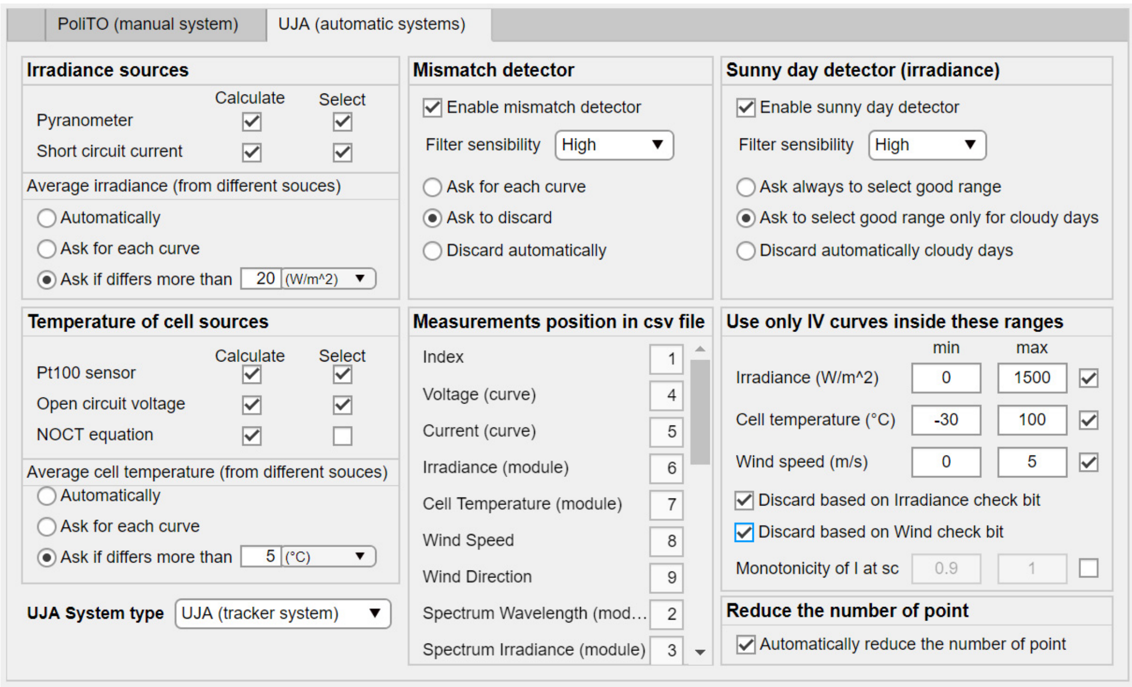

Figure 6.6: Picture of the graphical user interface for the preprocessing task- UJA (automatic system)

The panels involved in the data acquisition are presented in the following lines.

- The "Irradiance sources" panel allows the user to choose the irradiance sources to be used in the next steps. The sources are the pyranometer, the short-circuit current or they may be both. In the last case, the user may decide the method of calculating the average value of the two sources. The selected method between "automatically", "semi-automatically" or "manually" defines the level of user intervention. An ad hoc window, shown in Figure 6.7, intervenes in non-automatically cases for choosing the source case by case.

- The "Temperature sources" panel allows the user to choose the temperature sources to be used in the next steps. The sources of module temperature are the Pt100 probe, the open circuit voltage and the NOCT equation. The temperature considered is the average value if more than one source is selected. Moreover a window, in Figure 6.7, shows up in case of user intervention.

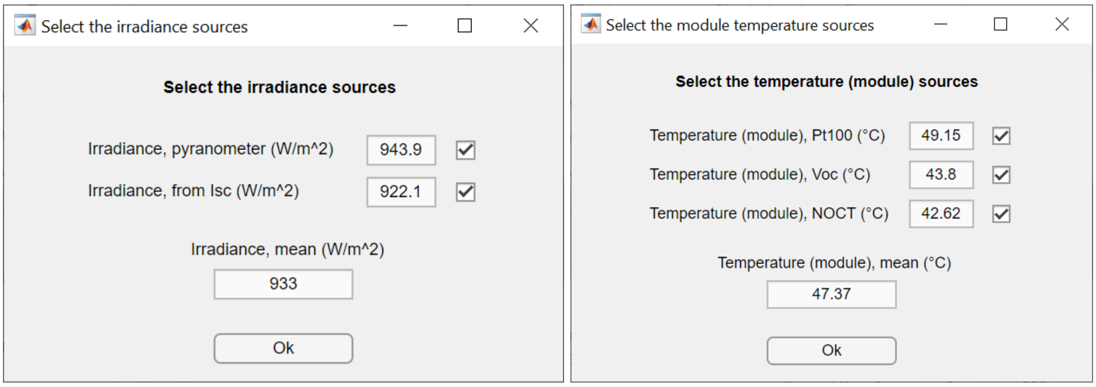

Figure 6.7: Picture of the irradiance and temperature manual selection

- The "Measurement position in CSV file" panel indicates the column position for each measured quantity in the CSV file. The position of each quantity is provided in three preloaded profiles, two for the tracker system and one for the fixed system. These profiles are selectable from the "UJA System type" list box. In addition, in this list box there is a fourth option called "Custom profile". Only in this case the edit fields of the quantities are editable. If a quantity is absent in the CSV file, a value of "-1" should be written down. Furthermore, it is important to indicate that a CSV file contains the values of the measurements for an *I-V* curve acquisition.

The panels involved in the filtering process are presented in the following lines.

- The "Mismatch detector" and the "Sunny day detector (irradiance)" panels are made up of three elements. They have a similar interface presented below. Firstly, the check box enables the mismatch/sunny day detector. Secondly, the list box allows the user to specify three level of filter's sensibility (high, medium, low). Finally, the button group defines the user's level of interaction (automatically, semi-automatically or manually). Further information about those two filters can be found in 6.2.2 for the sunny days filter and in 6.2.4 for the mismatch filter.
- The "Use only *I-V* curve inside these ranges" panel is composed of edit fields for four quantities. These quantities are irradiance, cell temperature, wind, and

current monotonicity at short circuit ranges (see 6.2.3). Besides, this panel includes two check boxes for filtering the data with the irradiance and/or wind check-bits.

- The "Reduce the number of points" panel contains the check box that enables a reduction in the *I-V* curve points. This reduction is necessary to solve the accumulation of points near the open circuit point (see 6.2.1).

6.2. Software operation for data preprocessing

The operation of the software for UJA files is analyzed in this sub-chapter. The software process is summarized in the flowchart of Figure 6.8. Each flowchart box will be treated separately in the following pages.

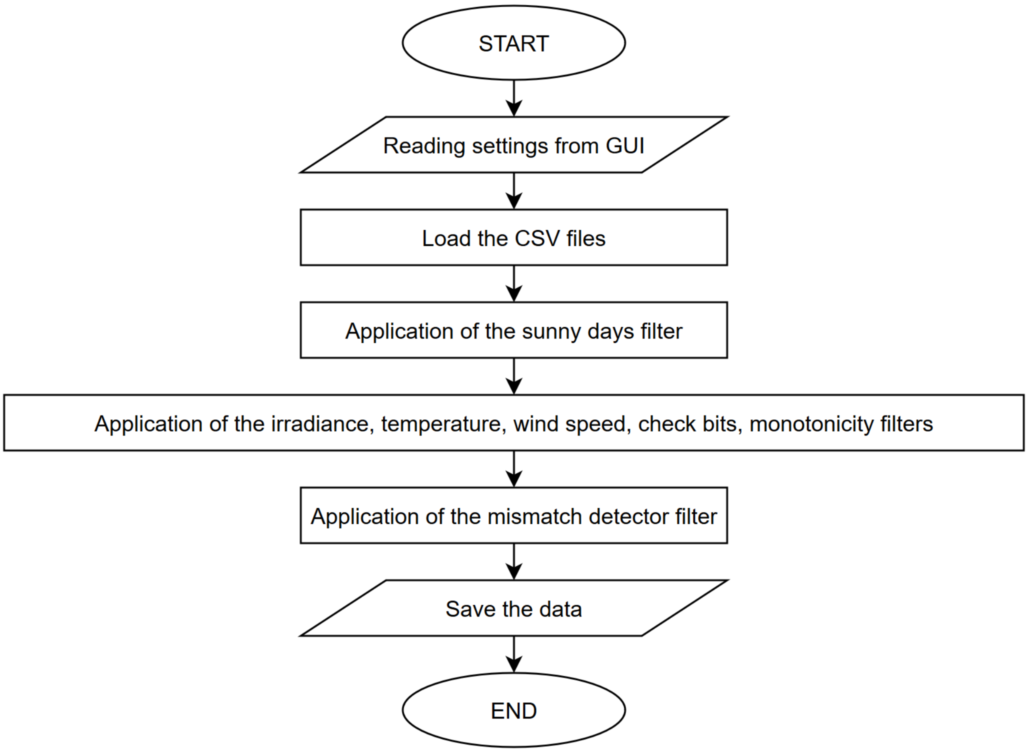

Figure 6.8: Flowchart of the data preprocessing

6.2.1. Load the CSV files

The first step of the flowchart is the "CSV file loading". This part was projected taking in account that the information inside the CSV files are different organized, depending on the measurement systems and year of acquisition. After loading the files correctly, the software calculates some important quantities using the data inside the CSV file. Those quantities are the open circuit voltage, the short circuit current, the maximum power, the MPP voltage and current, the fill factor, the module irradiance from the SC current, the module temperature from OC voltage and/or from NOCT equation, the average photon energy, the monotonicity value for voltage and current. The loading process is represented in Figure 6.9.

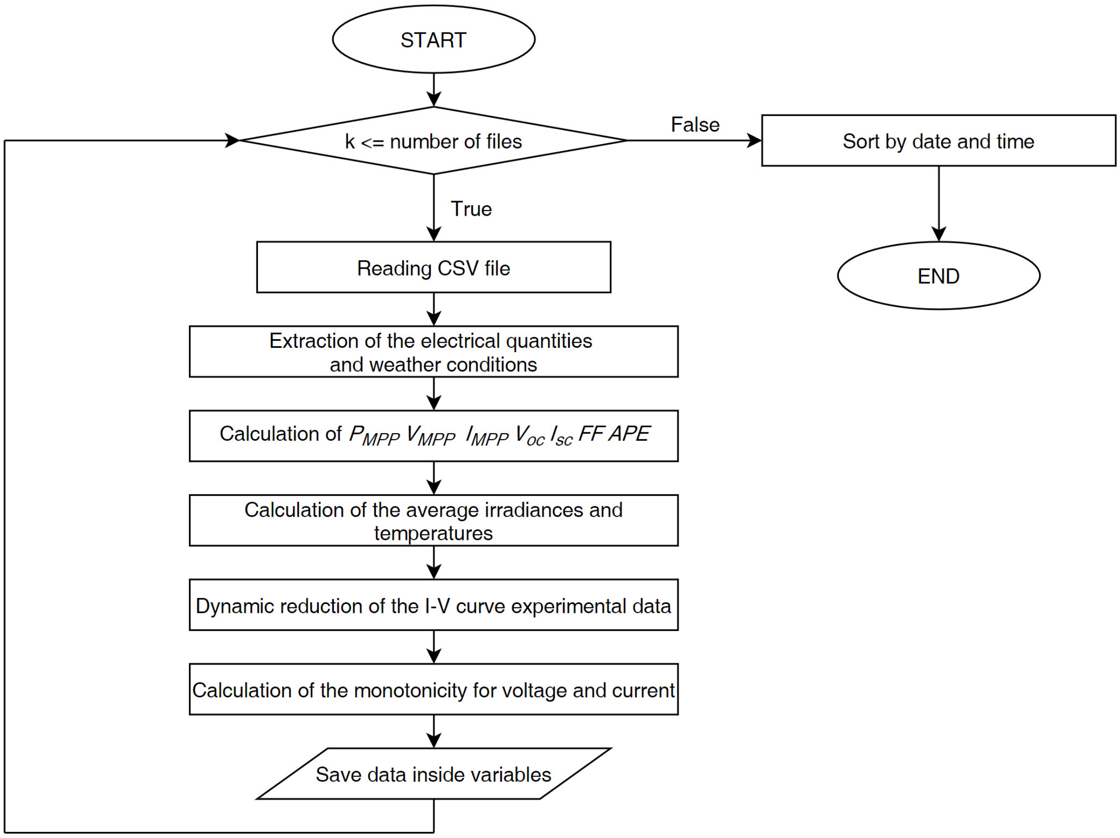

Figure 6.9: Flowchart of the loading process

The flowchart is based on a FOR loop which is repeated for each file. The FOR loop is composed of several steps described in the following lines.

1. "Reading the CSV file". The CSV file (char matrix) is converted into a MATLAB compatible format (double numerical matrix). This final matrix is called "`Curvas`"[2]. Moreover, a variable called "`Fecha`"[3] is also created. This variable contains the date and time of the *I-V* curve acquisition useful for correctly identifying data in various analysis

[2] "Curvas" means "curve" in English
[3] "Fecha" means "date" in English

2. “Extraction of the electrical quantities and weather conditions”. The electrical and weather quantities are extracted from the “`Curvas`” matrix. Besides, This process is carried out using the “position profile” information (see 6.1.2 Implemented data preprocessing for UJA (automatic system)). The electrical parameters are analyzed because they are of particular interest. Once the voltage and current columns from the “`Curvas`” matrix are found, a series of points is discarded. In fact, only the points of the *I-V* curve of the first quadrant are valid. Looking for the sign changes of the two quantities, the ending and starting points of the *I-V* curve are found. On the one hand, the ending point of the curve is in correspondence of the first current sign change at the maximum voltage value. On the other, the starting point is searched for in correspondence of the last voltage sign change or of the first values of the matrix applying search criteria.

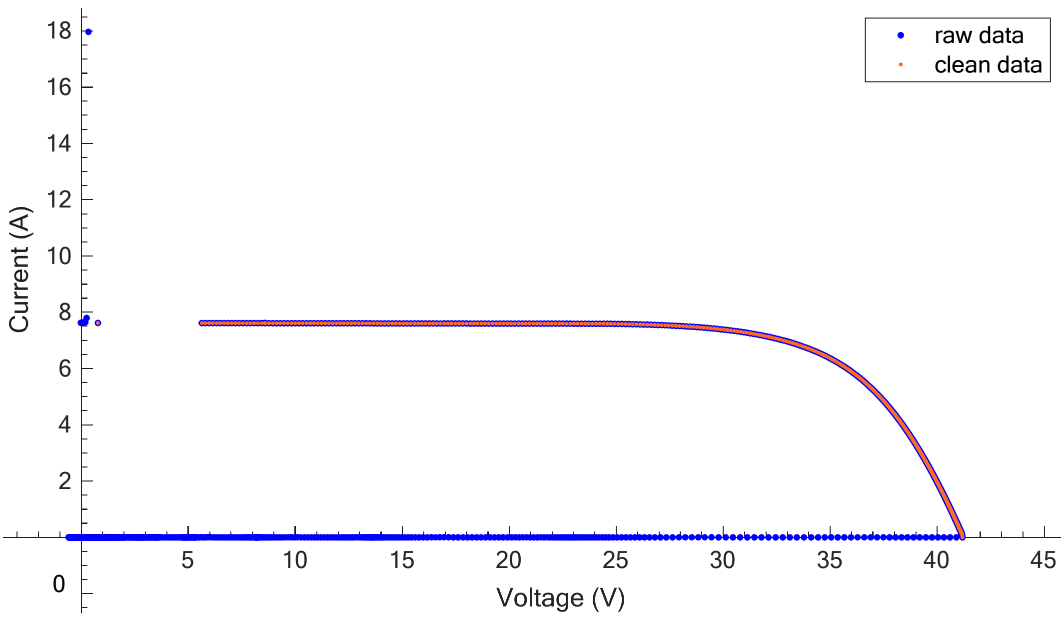

Figure 6.10: Extraction of the electrical quantities (in blue) from raw data (in orange)

3. “Calculation of P_{MPP} V_{MPP} I_{MPP} V_{oc} I_{sc} FF APE”. This step calculates a series of quantities used in subsequent analysis.
The power array is obtained with the product of voltage and current.
Firstly, the MPP is detected by searching the maximum point and secondly, the P_{MPP}, V_{MPP}, I_{MPP} are calculated.
Besides, there are two cases for finding the open circuit voltage, measured or calculated. In one case, if V_{oc} is measured, its value is in the last row of the voltage

column. In the other case, the open circuit value is obtained fitting linearly the last measured points in the V_{oc} region.

The short circuit current value is calculated by fitting linearly the points in the I_{sc} region. In the case of lack of points in the I_{sc} region, the short circuit current may not be computed correctly. The value of I_{sc} is set to NaN.

The fill factor FF is calculated according to equation (2.5).

The average photon energy (APE) is the average energy carried by a group of photons. Only the photon with a sufficient energy can be converted into electricity. Then, this index is a good indicator of the spectral content in the incident radiation. The APE is calculated as the ratio between the incident irradiance and the density of the total electron flow [30], in formula:

$$APE = \frac{\int_a^b F(\lambda) \cdot d\lambda}{q_e \cdot \int_a^b \Phi(\lambda) \cdot d\lambda} = \frac{h \cdot c \cdot \int_a^b F(\lambda) \cdot d\lambda}{q_e \cdot \int_a^b F(\lambda) \cdot \lambda \cdot d\lambda} \cdot 10^9 \tag{6.1}$$

Where:

- APE is the average photon energy (eV)
- $F(\lambda)$ is the spectral irradiance at wavelength λ ($\mathrm{W \cdot m^{-2} \cdot nm^{-1}}$)
- λ is the wavelength (nm)
- $\Phi(\lambda)$ is the spectral photon flux density at wavelength λ ($\mathrm{m^{-2} \cdot nm^{-1} \cdot s^{-1}}$)
- $q_e = 1{,}602 \cdot 10^{-19}$ C is the charge of the electron
- $h = 6{,}626 \cdot 10^{-34}$ J · s is the Planck constant
- $c = 2{,}998 \cdot 10^{8}$ m · s^{-1} is the speed of light in vacuum
- a and b are the lower and upper wavelength limits (nm)

4. "Calculation of the average irradiances and temperatures". This box calculates and selects the temperature and irradiance sources. The STC values necessary for calculations come from the Excel datasheet (see Figure 6.5). The calculations are executed following the order presented below.

   The first quantity is the module temperature calculated from V_{oc}, according to:

$$T_{c,V_{oc}} = \frac{V_{oc} - V_{oc,STC}}{\beta_{V_{oc}} \cdot V_{oc,STC}} + T_{c,STC} \tag{6.2}$$

Where:

- $T_{c,V_{oc}}$ is the module temperature from open circuit voltage (°C)
- V_{oc} is the open circuit voltage (V)

- $\beta_{V_{oc}}$ is the open circuit voltage thermal coefficient from Excel datasheet ($°C^{-1}$)
- $V_{oc,STC}$ is the open circuit voltage in STC from Excel datasheet (V)
- $T_{c,STC}$ is the cell temperature in STC ($T_{c,STC} = 25\ °C$)

The second value is the module irradiance calculated from I_{sc} using the formula:

$$G_{I_{sc}} = \frac{\frac{I_{sc}}{I_{sc,STC}} \cdot G_{STC}}{1 + \alpha \cdot \left(T_c - T_{c,STC}\right)} \tag{6.3}$$

Where:

- $G_{I_{sc}}$ is the module irradiance from short circuit current ($\mathrm{W} \cdot \mathrm{m}^{-2}$).
- I_{sc} is the short circuit current (A)
- α is the short circuit current thermal coefficient from Excel datasheet ($°C^{-1}$)
- $I_{sc,STC}$ is the short circuit current in STC conditions from Excel datasheet (A)
- G_{STC} is the irradiance in STC ($G_{STC} = 1000\ \mathrm{W} \cdot \mathrm{m}^{-2}$)
- T_c is the module temperature (°C). This temperature comes from the following logic procedure. $T_c = T_{c,Pt100}$ if only the temperature from Pt100 sensor is selected. $T_c = T_{c,V_{oc}}$ if only the temperature from open circuit voltage is selected. $T_c = mean(T_{c,Pt100}, T_{c,V_{oc}})$ if both temperatures from Pt100 sensor and open circuit voltage are selected. $T_c = T_{c,STC}$ if only the temperature from NOCT condition is selected (i.e. the temperature effect is neglected)

The third element is the value of the module irradiance (G) which comes from user selection. $G = G_{pyr}$ if only the irradiance from pyranometer is selected. $G = G_{I_{sc}}$ if only the irradiance from short circuit current is selected. $G = mean(G_{pyr}, G_{I_{sc}})$ if both irradiances from pyranometer and short circuit current are selected.

In addition, the module temperature is calculated from V_{oc} according to the formula:

$$T_{c,NOCT} = T_a + \frac{NOCT - T_{a,NOCT}}{G_{NOCT}} \cdot G \tag{6.4}$$

Where:

- $T_{c,NOCT}$ is the module temperature from NOCT equation (°C)
- T_a is the air ambient temperature (°C)
- $NOCT$ is the nominal operating cell temperature from Excel datasheet (°C)
- $T_{a,NOCT}$ is the air ambient temperature in NOCT conditions ($T_{a,NOCT} = 20\ °\mathrm{C}$)
- G_{NOCT} is the irradiance in NOCT conditions ($G_{NOCT} = 800\ \mathrm{W \cdot m^{-2}}$)

Eventually, the last element is the value of the module temperature (T_c) chosen between the following options. $T_c = T_{c,Pt100}$ if only the temperature from Pt100 sensor is selected. $T_c = T_{c,V_{oc}}$ if only the temperature from open circuit voltage is selected. $T_c = T_{c,NOCT}$ if only the temperature from NOCT condition is selected. $T_c = mean(T_{c,Pt100}, T_{c,V_{oc}})$ if both temperatures from Pt100 sensor and open circuit voltage are selected. $T_c = mean(T_{c,Pt100}, T_{c,NOCT})$ if both temperatures from Pt100 sensor and NOCT equation are selected. $T_c = mean(T_{c,V_{oc}}, T_{c,NOCT})$ if both temperatures from Pt100 sensor and open circuit voltage and NOCT equation are selected. $T_c = mean(T_{c,Pt100}, T_{c,V_{oc}}, T_{c,NOCT})$ if all the three temperatures from Pt100 sensor, open circuit voltage and NOCT equation are selected.

5. "Dynamic reduction of the *I-V* curve experimental data". This box resolves the problem linked to the no uniformly spaced acquisition of points in the *I-V* curve. This procedure reduces the gap between two consecutive points in the *I-V* curve, as in Figure 6.11 (red). The first operation consists in normalizing the voltage and current data. Then, the maximum and mean spaces among the points are considered in order to determine the admissible spaces to apply. If the gap measured between two consecutive points is less than the minimum admissible value, the second point is deleted. Then, if the new gap is more than the maximum admissible value, the deleted point is re-added. This operation is performed starting from the SC point to the OC point. The output data are stored at the end of the procedure in variables with the "`_light`" suffix.

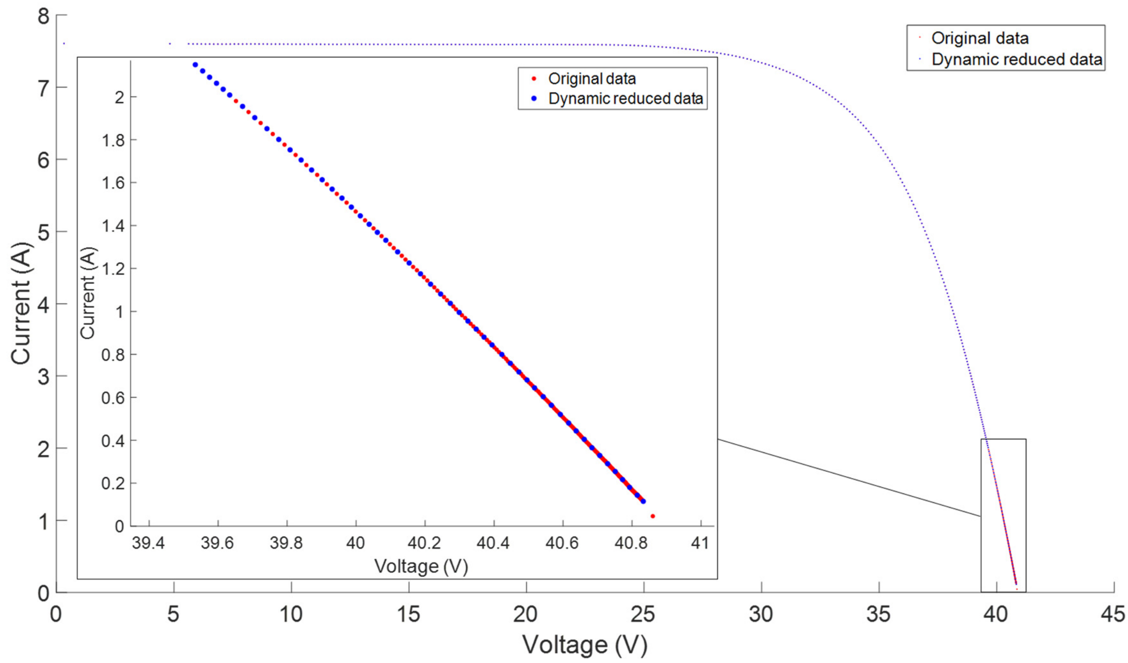

Figure 6.11: Comparison between an original *I-V* curve (red) and the dynamic reduced one (blue). The two curves overlap except in the section near the OC point.

6. "Calculation of the monotonicity for voltage and current". This step computes a coefficient that shows how far the array trend is from the monotonic property. This coefficient takes a value in the range [0; 1], and, particularly, 1 in the case of a strictly monotonic IV curve. The computation is done with the MATLAB "`monotonicity`" function for three arrays: all voltage points, all current points, and current points from SC up to MPP.
7. "Save data inside variables". The last procedure consists in saving the data in an organized way ensuring a simple access. Six arrays, that always keep the same sorting, are used. They are described in the following lines. The first struct array is "`archivos`" in which each row contains the original filename and path of the CSV file. Secondly, "`Curvas`" is a cell array in which each cell contains a matrix with the raw data. The raw data are then stored in this variable in order to allow retrospect verification. Thirdly, "`Fecha`" is another cell array where each cell contains the date and time of all the acquisitions in the "YYYY_MM_DD_hh_mm_ss" format. Fourthly, "`Measurement`" is a cell array where the individual cell contains an ad hoc struct for the data storage of each acquisition, as in Figure 6.12. The timetable "`MeasurementConditions`" reports the main acquired quantities to simplify the creation of plots. To conclude,

the last datetime array is "`TimeStamp`" in which each row contains the date and time of each acquisition.

Field	Value
Timestamp	*1x1 datetime*
index	*501x1 double*
Voltage	*501x1 double*
Current	*501x1 double*
index_light	*167x1 double*
Voltage_light	*167x1 double*
Current_light	*167x1 double*
ModuleIrradianceSpectrum	*256x2 double*
ModuleIrradiance	1.0551e+03
ModuleIrradiance_pyr	1.0551e+03
ModuleIrradiance_Isc	972.2581
ModuleIrradianceSources	'pyr'
ModuleTemperature	48.3280
ModuleTemperature_Pt100	48.3280
ModuleTemperature_Voc	42.0177
ModuleTemperature_NOCT	45.2831
ModuleTemperatureSources	'Pt100'
WindSpeed	0.8710
WindDirection	0.6115
RelativeAirHumidity	26.5640
HorizontalPlaneIrradiance	555.7895
AmbientAirTemperature	12.3100
AtmosphericPressure	1.0375e+03
ModuleDirectIrradiance	957.3529
CoefficientC0SpectroradiometerWavelength	303.4420
CoefficientC1SpectroradiometerWavelength	3.3015
CoefficientC2SpectroradiometerWavelength	2.8278e-04
CoefficientC3SpectroradiometerWavelength	-1.6321e-06
CoefficientC4SpectroradiometerWavelength	0
IrradianceCheckBit	0
WindCheckBit	*[]*
SpectralIrradianceTOP	793.9230
SpectralIrradianceMIDDLE	796.0550
SpectralIrradianceBOTTOM	834.5610
ShortCircuitCurrent	7.7271
OpenCircuitVoltage	40.5866
MaxPower	227.0175
MPPVoltage	32.3296
MPPCurrent	7.0220
FillFactor	0.7239
AveragePhotonEnergy	1.7969
MonotonicityVoltage	1
MonotonicityCurrent	0.5663
MonotonicityCurrentSC	0.9750
system	'UJA (tracker old system)'
info	*1x1 struct*
VariableUnits	*47x94 char*

Figure 6.12: Sample of the struct of one "Measurement" cell

6.2.2. Sunny days filter

The second step of the flowchart in the Figure 6.8 is the "Application of the sunny days filter". After loading the data, calculating various electrical quantities and the monotonicity index, the information can be further selected with filters. The sunny days filter is implemented to detect and discard the days when the shape of irradiance is not regular. Firstly, the GTI and GHI in "`MeasurementConditions`" are split up by days and then they are cyclically analyzed. The analysis of the GTI and GHI consists of a Fourier series of the fourth and second order respectively. The output of this study is the R^2 parameter which is compared to the tolerance value selected by the user in the GUI. There are three levels of tolerance proposed to the user: "high" ($R^2 \geq 0{,}9975$), "medium" ($R^2 \geq 0{,}9920$), and "low" ($R^2 \geq 0{,}9800$). The type of operation in the next process depends on the user's selected option among automatically, semi-automatically and manual. Firstly, automatically means that only the sunny days information is kept. Secondly, semi-automatically consists in the manual selection of one or more parts of the non-sunny days. Manually implies the user manual selection of one or more parts every day. Besides, in the case of discarded data, the corresponding information in the six variables (i.e. "`archivos`", "`Curvas`", "`Fecha`", "`Measurement`", "`MeasurementConditions`", "`TimeStamp`") is also deleted. Finally, if the "Save figure" option in the GUI is enabled, the figure of each day is saved in the selected export folder.

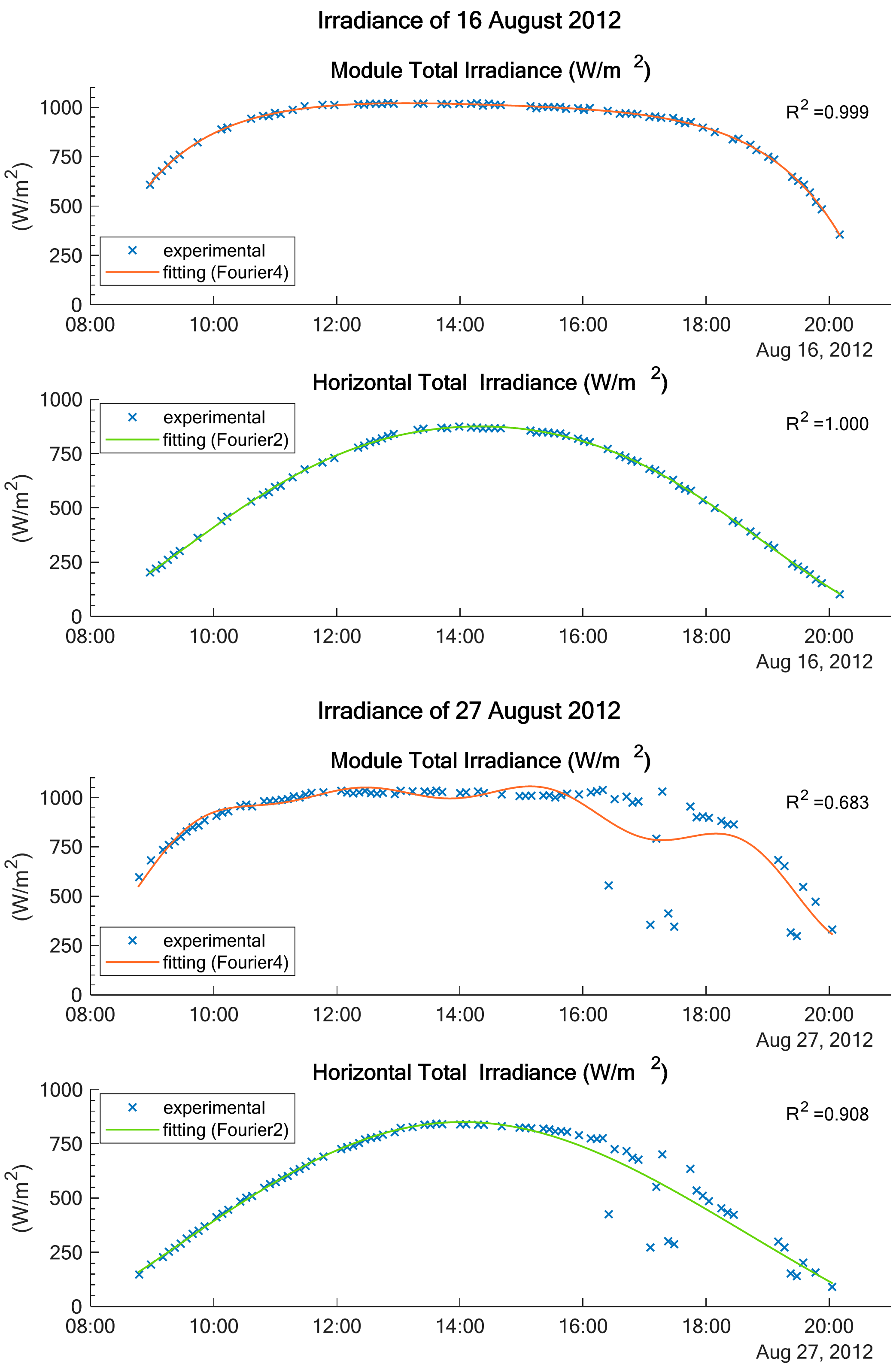

Figure 6.13: Sunny days filter: analysis for two different days. Sunny day upper and non-sunny day lower

6.2.3. Irradiance, temperature, wind speed, check bits and monotonicity of short circuit current ranges filters

The second step of the flowchart in the Figure 6.8 is the "Application of the irradiance, temperature, wind speed, check bits and monotonicity filters". The filtering operation, started by applying the sunny days filter, continues in this section. The ranges specified in the GUI are applied to the module irradiance, module temperature, wind speed and monotonicity at SC. Moreover, two check bits information in the "`MeasurementConditions`" timetable can be used to filter the irradiance and the wind acquisitions. The data are still filtered if the check bit is true. This condition occurs when the irradiance changes (e.g. 10%) or the wind is greater than a certain value (e.g. 5 m/s). Finally, the corresponding information in the six variables (i.e. "`archivos`", "`Curvas`", "`Fecha`", "`Measurement`", "`MeasurementConditions`", "`TimeStamp`") is also eliminated in the case of discarded data.

6.2.4. Mismatch detector filter

The last box of the flowchart in the Figure 6.8 is the "Application of the mismatch detector filter". The aim of the mismatch filter is to find back the presence of shadow on the module. This filter is important because the presence of a mismatch leads to an unreliable *I*-*V* curve for most analyses. The mismatch appears as a stair in the *I*-*V* curve and appears as a local peak in the *P*-*V* curve, as in Figure 6.14. This filter has three levels of tolerance chosen by the user: "high", "medium" and "low". The operation of the filter is described in the following lines.

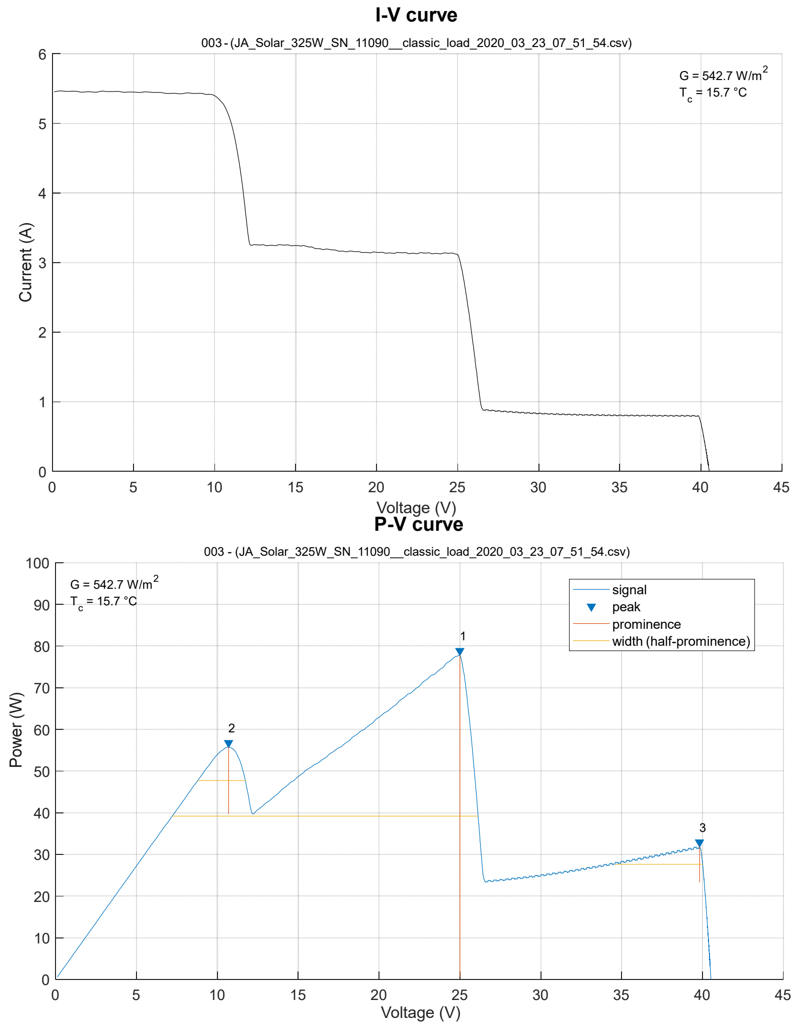

Figure 6.14: Sample of a measure with mismatch.
I-*V* curve on top and *P*-*V* curve on bottom.

The implemented filter uses three methods to find mismatch.

- The analysis of the *P*-*V* curve finds more than one peak in case of shadow. This operation is performed with the "`findpeaks`" MATLAB function. This function receives two vectors as input, one for power and one for voltage. The first vector is used for finding the local peaks in the power data. The voltage vector is used for quantifying the peak widths. This vector should be strictly increasing: the own made function "`convertInStrictmonotonic`" is used to remove the points outside the monotonic trend. The sorted vectors obtained are used only to find peaks and are not used for other analysis. The "`findpeaks`" function finds the local peaks and their relative prominence. The peaks found depend on the settled tolerances. The first tolerance on prominence is defined by the user: 0,5 for “high”, 0,75 for “medium”, 1 for “low”. A high tolerance means greater sensitivity in identifying points and therefore the possibility of finding peaks due to noise. The experimental data show that the noise is mainly located in the low power regions. For this reason, a second tolerance on the minimum peak power is defined. This second tolerance is expressed relatively to the maximum power (i.e. $0{,}05 \cdot P_{MPP}$ for “high”, $0{,}08 \cdot P_{MPP}$ for “medium”, $0{,}12 \cdot P_{MPP}$ for “low”).

- The analysis of the *I-V* curve finds error points (stairs in case of mismatch and/or isolated points). An ad hoc function called “`IVcurveshapetest`” is created for examining the part of the *I-V* curve from the SC point up to $x \cdot P_{MPP}$. The x factor depends on the tolerance level and on the fill factor. This function is composed of two tests. The first test fits the zone of interest in four sections with lines, as in Figure 6.15. Then, the disparity between two consecutive lines is calculated. The disparity obtained should be less than the user-imposed tolerance, in order to pass the test. The tolerance value is expressed in percentage over the SC current (i.e. 0,25% for “high”, for 0,5% “medium”, 0,75% for “low”). This first part of the function is sufficient for finding the stairs. The second shape test fits the same portion of the *I-V* curve (from the SC point up to $x \cdot P_{MPP}$) with only one line, as in Figure 6.15. This test finds punctual errors between experimental points and the fitted line. The tolerance is the same considered in the first test.
- The third method is a voltage monotonicity test. The monotonicity of the voltage vector, calculated in the 6.2.1, is present in the “`MeasurementConditions`” timetable. This value is compared to a user-imposed tolerance (i.e. 0,95 for “high”, for 0,90 “medium”, 0,85 for “low”). The higher the tolerance, the more pronounced the selection

Finally, if the “Save figure” option in the GUI is enabled, the figures of each *I-V* and *P-V* curves are saved in the selected export folder.

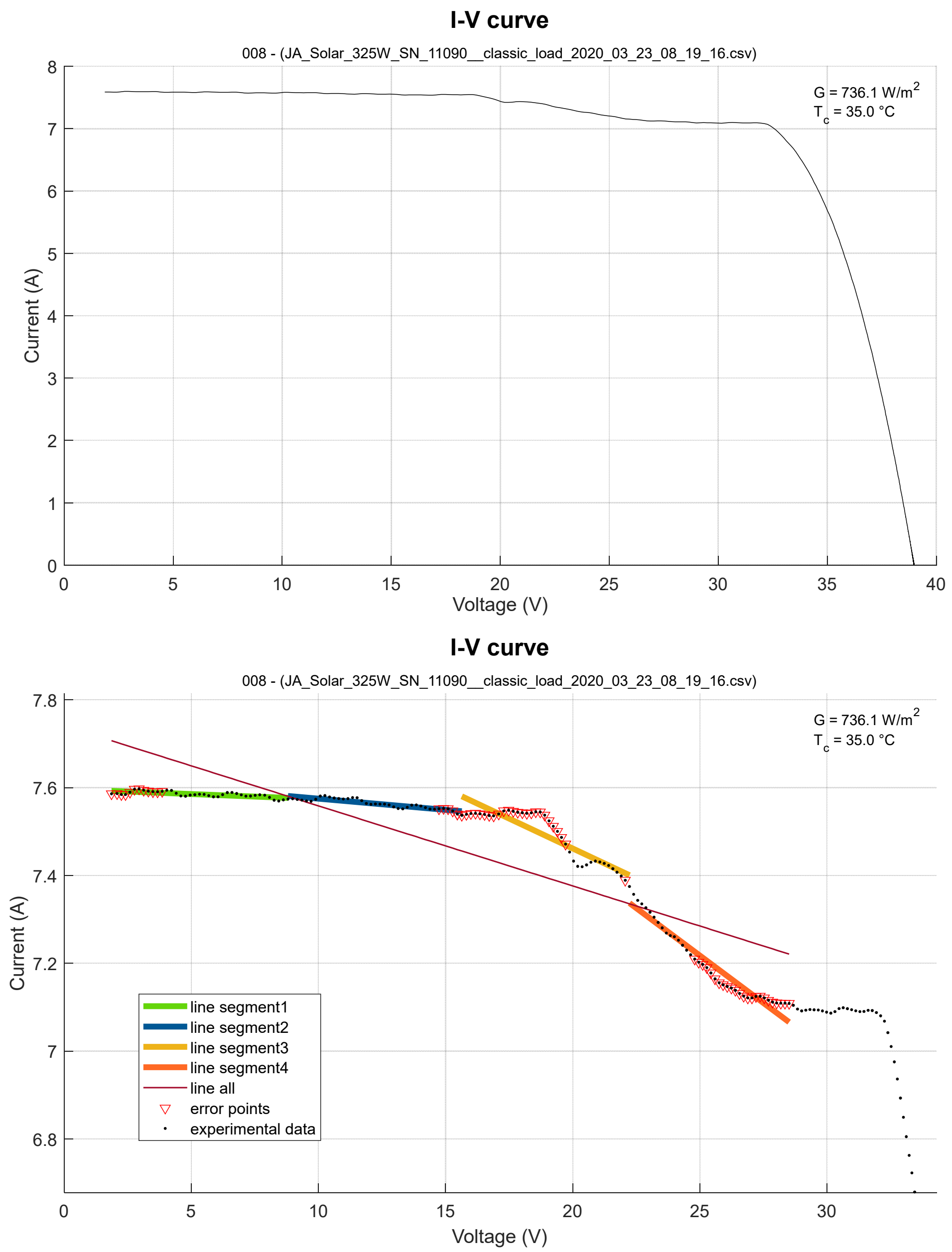

Figure 6.15: Working principles of the mismatch filter on the *I-V* curve.

6.2.5. Save the data inside "mat" files

The last part of the preprocessing, shown in the flowchart in the Figure 6.8, consists in saving the data into "mat" files. The saving procedure could be personalized by the user in the GUI. The saving options, explained below, influence the name of the file and the division in files.

- "All in the same file". Only one file is created by selecting this option. The name of this file depends on the number of days considered. If the data are taken in one day, the filename is in the "prefix_modulename_YYYY_MM_DD_sufix" format. If the data are taken during more days in a month, the filename is in the "prefix_modulename_YYYY_MM_sufix" format. If the data are taken during more months in a year, the filename has the "prefix_modulename_YYYY_sufix" format. If the data are taken during more years, the filename has the "prefix_modulename_YYYY_YYYY_sufix" format.
- "Divide by days". One file for each day is created by selecting this option. The name is in the "prefix_modulename_YYYY_MM_DD_sufix" format.
- "Divide by months". One file for each month is created. The name is in the "prefix_modulename_YYYY_MM _sufix" format.
- "Divide by years". One file for each year is created. The name is in the "prefix_modulename_YYYY_sufix" format.
- ''Divide by irradiance". One file for each range of irradiance is created. The name is in the "prefix_modulename_minG_maxG_sufix" format.
- "Divide by temperature (module)". One file for each range of temperature is created. The name is in the "prefix_modulename_minT_maxT_sufix" format.
- "Divide by irradiance and temperature (module)". One file for each range of irradiance and temperature is created. The name is in the same format of the previous two points.

Moreover, the software checks if the filenames already exist. In this case, a sequential number is written at the end of the format.

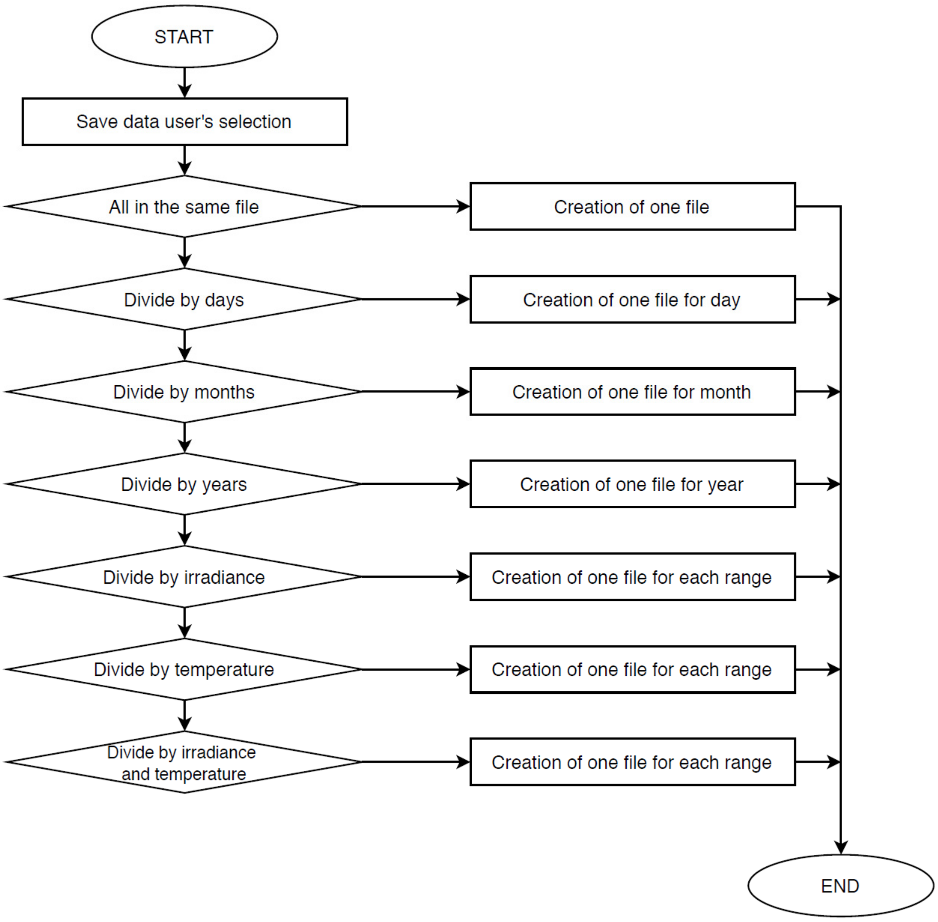

Figure 6.16: Saving data flowchart

Chapter 7

Parameters extraction

The parameter extraction process consists in a numeric optimization used to solve the equation system linked to the PV cells equivalent circuit. The GUI is designed to implement two different PV models and three different extraction algorithms. The two models are the five parameters, used in this thesis, and the seven parameters. The three algorithms are firstly the Levenberg-Marquardt (LM), secondly, the combination of Simulated annealing and Nelder-Mead (SA-NM), and finally, a third algorithm can be added for future analysis. Summing up, only the five parameters model and the LM and SA-NM algorithms are used for the elaboration. The graphical interface and the software operation are presented in the next two section.

7.1. Graphical interface for parameters extraction

The graphical interface is designed to contain all needed settings in the simplest manner. Figure 7.1 shows the interface when the section is open.

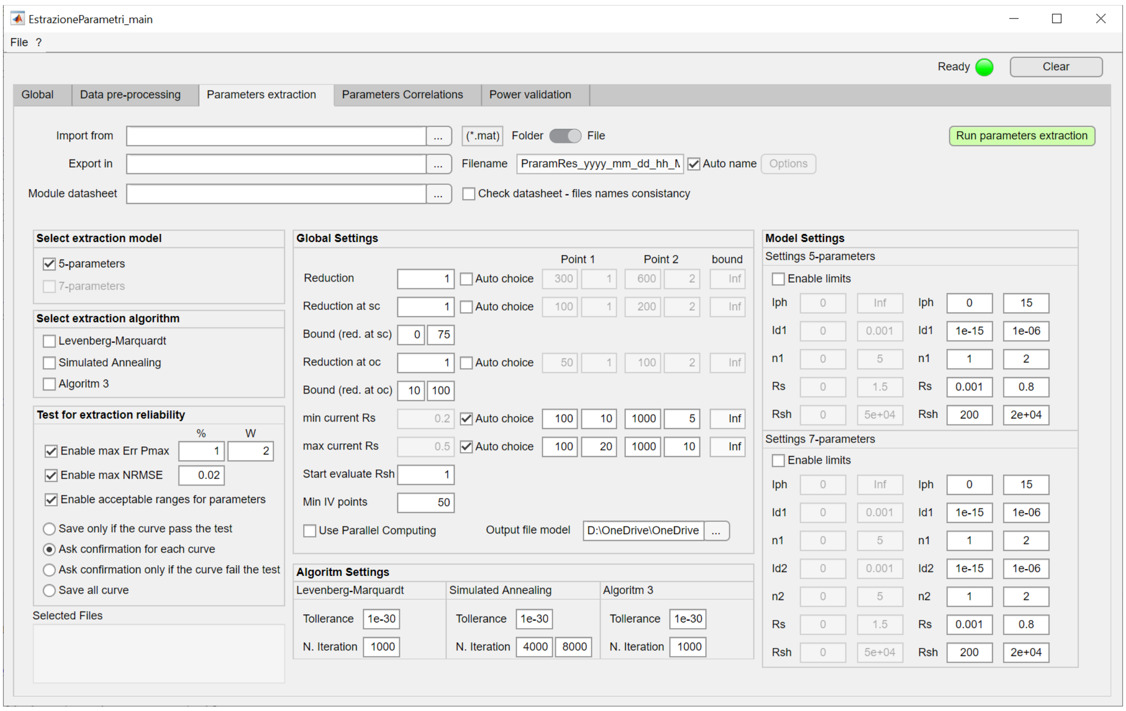

Figure 7.1: Picture of the graphical user interface tab for the parameters extraction

The import/export section, in the upper part, works in the same way as the data preprocessing, described in 6.1.1.

The following two subparagraphs describe two user interfaces. The first section is the Figure 7.1 where the settings employed to start the parameter extraction are presented. The second one shows the results of the extraction.

7.1.1. Parameters extraction GUI settings

The settings for the parameters extraction are grouped in six panels. These panels will be described starting from the model/algorithm selected up to specific settings.

The first panel is called "Select extraction model". The calculations for the parameters extraction of both models (5 and 7 parameters) are performed automatically and successively.

The second panel is called "Select extraction algorithm". The calculations for the parameters extraction are done with all the algorithms.

The "Test for the extraction reliability" allows the user to set the option related to the extracted parameters filtering. The test consists of three validations: the maximum error on power (absolute and relative), the maximum *NRMSE*, and the value of the parameters in a user defined range. In particular, the limits on the parameters can be set in the "Model Settings" panel because they change according to the model. Moreover, the filter can operate in four modes: first automatically (it saves only if the curve passes the test), second, semi-automatically (it asks confirmation for saving if the curve fails the test), third, manually (it asks confirmation for saving for each curve), and finally disabled (it saves all the curves).

In the "Global settings" panel, the user selects the main conditions of the extraction process. The most important options are described in the following lines.

- "Reduction". This option reduces the number of points in the *I-V* curve to speed up the optimization. The user can select a number between 1 (that means no reduction) and (theoretically) infinite. The greater the number x chosen, the greater the reduction because the algorithm uses a point every x points. (i.e. $x = 2$ means taken the points number 1, 3, 5, ...). Moreover, the value of reduction can be computed automatically to maintain a constant number of points of the *I-V* curve.
- "Reduction at SC". This setting has an identical operation as "Reduction" but only in the current source section, between SC and MPP points.

- "Bound (red. at SC)". This condition restricts the section where the "Reduction at SC" operates. This area of operation is defined by two points expressed in percentage over MPP (i.e. 0% means SC point and 100% means MPP point).
- "Reduction at OC". This setting has an identical behavior as "Reduction" but only in the voltage source section, between MPP and OC points.
- "Bound (red. at OC)". This option restricts the section where the "Reduction at OC" operates. This area of operation is defined by two points expressed in percentage over MPP (i.e. 0% means MPP point and 100% means OC point).
- "min current Rs" and "max current Rs". The initial parameter condition must be defined properly for the convergence of the algorithms. These values are the minimum and maximum values of current used to estimate the initial condition of the R_s. These values are expressed in percentage over the I_{sc}. Moreover, the value can be computed automatically. In this setting, the user defines a percentage with respect to the short-circuit current, variable with the irradiance. In this way, an analyzed constant interval is obtained.
- "Start evaluate Rsh": starting point to estimate the first value of the R_{sh}.
- "min *I*-*V* points": minimum number of point that the *I*-*V* curve must have to be elaborated.

"Algorithm Settings". This panel contains the settings of maximum number of iteration and the end tolerance for each algorithm.

"Model setting". This panel contains the bounds for the optimization and the limits for the test on the output.

7.1.2. Parameters extraction result Graphical Interface

The "Parameters extraction result GUI" can be opened at the end of the extraction process based on the "Test for the extraction reliability" settings. The interface has been represented in Figure 7.2. The aim of this interface is to provide the most important information about the extraction to the user. This information is the extracted parameters, the maximum power error, the *NRMSE*, and the curve plot. Moreover, the interface highlights the information that does not satisfy the desired bounds, as in Figure 7.2. Finally, this interface provides the possibility to accept or discard the extraction in the export file.

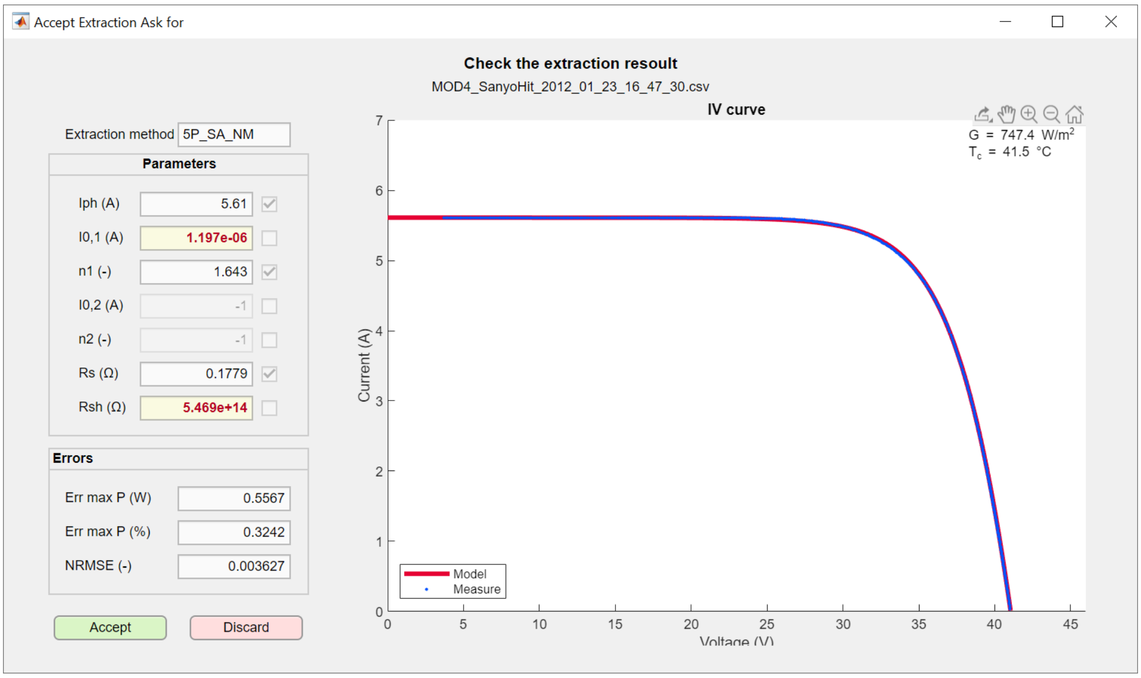

Figure 7.2: Picture of the "Parameters extraction result GUI"

7.2. Software for parameters extraction

The main software operation for parameters extraction is analyzed in this subchapter. The flowchart in Figure 7.3 shows the flow of the parameters extraction procedure. The extraction procedure consists in the estimation of the initial condition and the implementation of a least square optimization algorithm to solve the curve fitting problem.

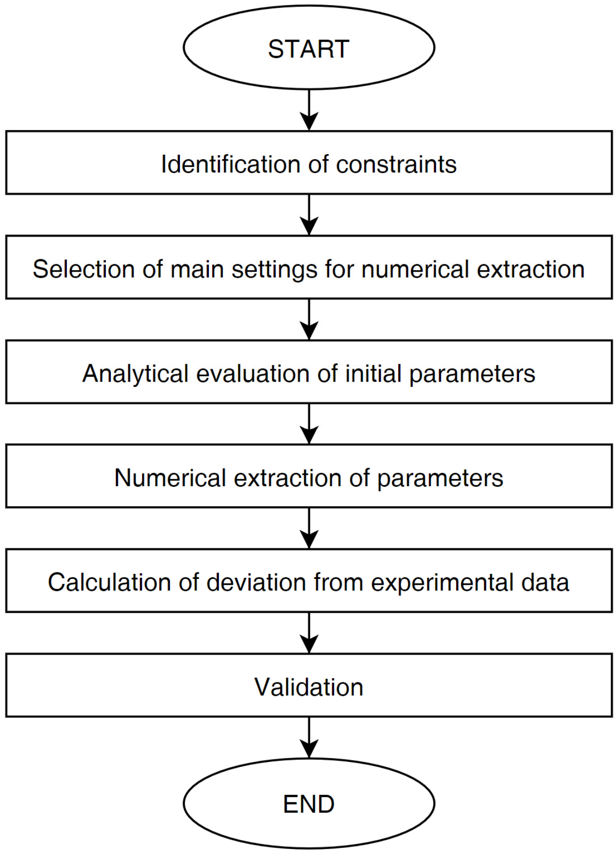

Figure 7.3: Flowchart of the parameters extraction procedure

7.2.1. Equations for five parameters extraction

The implementation in this thesis holds the five parameters model (5P) with two different optimization procedures (LM and SA-NM). The fitting equation depends only on the model and it can be derived from the analysis of the equivalent circuit (see 2.9. Analytical description). On the one hand, the explicit equation is adopted in the LM based optimization procedure, whereas on the other hand, the implicit form is implemented in the SA-NM optimization procedure. Below, the implicit and the explicit equation for a PV module are reported.

Starting from the equation (2.13) and using the following replacement:

$$V_t = \frac{k_B \cdot T_c}{q_e} \tag{7.1}$$

Where:

- V_t is the thermal voltage (V)
- T_c is the cell temperature (K)

- k_B is the Boltzmann constant ($\mathrm{J} \cdot \mathrm{K}^{-1}$)
- q_e is the electron charge (C)

The implicit form is obtained (see [31]):

$$I = I_{ph} - I_0 \cdot \left(e^{\left(\frac{R_s \cdot I + V}{V_t \cdot n \cdot N_s}\right)} - 1 \right) - \frac{V + R_s \cdot I}{R_{sh}} \tag{7.2}$$

Where:

- I is the output current (A)
- V is the output voltage (V)
- I_{ph} is the photogenerated current (A)
- I_0 is the diode saturation current (A)
- n is the diode ideality factor (-)
- R_s is the series resistance (Ω)
- R_{sh} is the shunt resistance (Ω)
- N_s is the number of cells in series (-)

The explicit form, from [32] is:

$$I = R_{sh} \cdot \frac{(I_{ph} + I_0)}{(R_s + R_{sh})} - \frac{V}{R_s + R_{sh}} + n \cdot V_t \cdot \frac{N_s}{R_s} \cdot \left(-\mathrm{W} \left(R_s \cdot R_{sh} \cdot I_0 \cdot \frac{e^{\left(R_{sh} \cdot \frac{R_s \cdot I_{ph} + R_s \cdot I_0 + V}{N_s \cdot n \cdot V_t \cdot (R_s + R_{sh})}\right)}}{N_s \cdot n \cdot V_t \cdot (R_s + R_{sh})} \right) \right) \tag{7.3}$$

Where:

- W is the Lambert W function

$$z = \mathrm{W}(z) \cdot e^{\mathrm{W}(z)} \tag{7.4}$$

The solution of these equations with respect to the five unknown parameters (i.e. I_{ph}, I_0, n, R_s, R_{sh}) could be performed in several ways as described in [33]. There are two main types of approach: analytical and numerical. Firstly, the analytical methods search for the solutions of the system by solving the system equations. The analytical approach is difficult to apply in case of complex systems because of the high number of equations and unknows parameters. A compromise between the equations simplification and the accuracy should be made to use those these methods. Secondly the numerical approach is adopted for complex systems. The solutions in the numerical methods are searched through the iterative calculations of a set of equations.

7.2.2. Evaluation of initial conditions

The convergence of the least square optimization algorithm is strictly related to the initial conditions. Therefore, the choice of the initial parameters values is critical for obtaining a good solution. The computation of the initial conditions is achieved with an analytical-numerical procedure, according to [34], and it is shown in Figure 7.4. The transcendental equation of the equivalent circuit (7.2) is evaluated in the short circuit, open circuit, and maximum power points, as in equations (7.5), (7.6), (7.7). I_0, R_s, R_{sh} are calculated with an iterative numerical algorithm. Moreover, n is supposed equal to 1,5. The whole method is reported in the following lines.

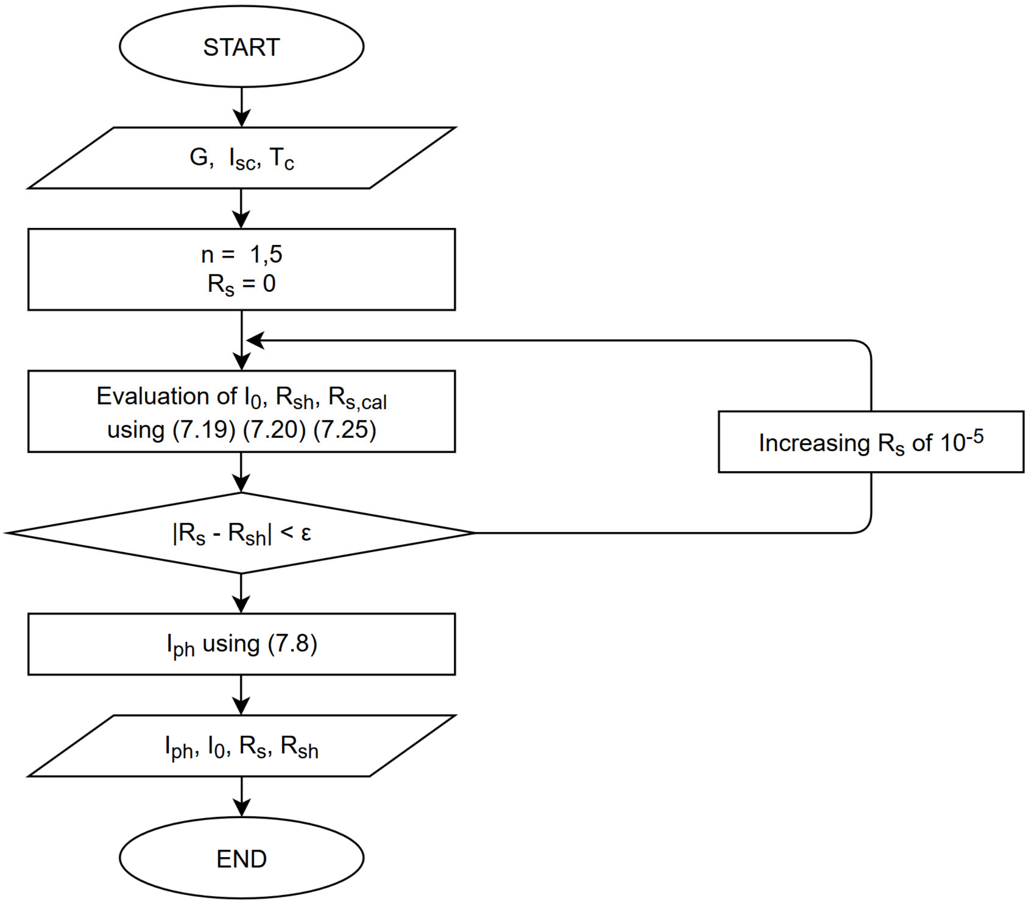

Figure 7.4: Evaluation of initial conditions flow chart

Some quantities are calculated before the iterative process, such as I_{sc}, V_{oc}, I_{MPP}, V_{MPP}. Successively, the equation (7.2) is rewritten in the SC, OC and MPP points. The equations for each characteristic point are reported in the following lines.

Short circuit point:

$$(V, I)_{\mathrm{SC}} = (0, I_{sc})$$

$$I_{sc} = I_{ph} - I_0 \cdot \left(e^{\left(\frac{R_s \cdot I_{sc}}{V_t \cdot n \cdot N_s}\right)} - 1 \right) - \frac{R_s \cdot I_{sc}}{R_{sh}} \tag{7.5}$$

Open circuit point:

$$(V, I)_{\mathrm{oc}} = (V_{oc}, 0)$$

$$0 = I_{ph} - I_0 \cdot \left(e^{\left(\frac{V_{oc}}{V_t \cdot n \cdot N_s}\right)} - 1 \right) - \frac{V_{oc}}{R_{sh}} \tag{7.6}$$

Maximum power point:

$$(V, I)_{\mathrm{MPP}} = (V_{MPP}, I_{MPP})$$

$$I_{MPP} = I_{ph} - I_0 \cdot \left(e^{\left(\frac{R_s \cdot I_{MPP} + V_{MPP}}{V_t \cdot n \cdot N_s}\right)} - 1 \right) - \frac{R_s \cdot I_{MPP} + V_{MPP}}{R_{sh}} \tag{7.7}$$

The photovoltaics current could be derived from (7.6)(7.5):

$$I_{ph} = I_0 \cdot \left(e^{\left(\frac{V_{oc}}{V_t \cdot n \cdot N_s}\right)} - 1 \right) + \frac{V_{oc}}{R_{sh}} \tag{7.8}$$

Then, equation (7.8) is substituted in equations (7.6) and (7.7). Equations (7.9) and (7.10) could be found after some calculations:

$$I_{sc} = I_0 \cdot \left(e^{\left(\frac{V_{oc}}{V_t \cdot n \cdot N_s}\right)} - e^{\left(\frac{R_s \cdot I_{sc}}{V_t \cdot n \cdot N_s}\right)} \right) + \frac{V_{oc} - R_s \cdot I_{sc}}{R_{sh}} \tag{7.9}$$

$$I_{MPP} = I_0 \cdot \left(e^{\left(\frac{V_{oc}}{V_t \cdot n \cdot N_s}\right)} - e^{\left(\frac{V_{MPP} + R_s \cdot I_{MPP}}{V_t \cdot n \cdot N_s}\right)} \right) + \frac{V_{oc} - V_{MPP} - R_s \cdot I_{MPP}}{R_{sh}} \tag{7.10}$$

The following substitution is made to simplify the expression:

$$X_{sc} = e^{\left(\frac{R_s \cdot I_{sc}}{V_t \cdot n \cdot N_s}\right)} \tag{7.11}$$

$$X_{oc} = e^{\left(\frac{V_{oc}}{V_t \cdot n \cdot N_s}\right)} \tag{7.12}$$

$$X_{MPP} = e^{\left(\frac{V_{MPP} + R_s \cdot I_{MPP}}{V_t \cdot n \cdot N_s}\right)} \tag{7.13}$$

And the following equation could be obtained:

$$I_{sc} \cdot \left(1 + \frac{R_s}{R_{sh}}\right) = I_0 \cdot (X_{oc} - X_{sc}) + \frac{V_{oc}}{R_{sh}} \tag{7.14}$$

$$I_{MPP} \left(1 + \frac{R_s}{R_{sh}}\right) = I_0 \cdot (X_{oc} - X_{MPP}) + \frac{V_{oc} - V_{MPP}}{R_{sh}} \tag{7.15}$$

Because of $R_s \gg R_{sh}$:

$$\left(1 + \frac{R_s}{R_{sh}}\right) \approx 1 \tag{7.16}$$

And the equations (7.14), (7.15) turn into:

$$I_{sc} = I_0 \cdot (X_{oc} - X_{sc}) + \frac{V_{oc}}{R_{sh}} \tag{7.17}$$

$$I_{MPP} = I_0 \cdot (X_{oc} - X_{MPP}) + \frac{V_{oc} - V_{MPP}}{R_{sh}} \tag{7.18}$$

Finally, the following equations are derived from the equations (7.17), (7.18):

$$I_0 = \frac{I_{sc} \cdot (V_{MPP} - V_{oc}) + V_{oc} \cdot I_{MPP}}{V_{MPP} \cdot (X_{oc} - X_{sc}) - V_{oc} \cdot (X_{MPP} - X_{sc})} \tag{7.19}$$

$$\frac{1}{R_{sh}} = \frac{I_{sc} \cdot (X_{MPP} - X_{oc}) + I_{MPP} \cdot (X_{oc} - X_{sc})}{V_{oc} \cdot (X_{MPP} - X_{sc}) - V_{MPP} \cdot (X_{oc} - X_{sc})} \tag{7.20}$$

The equations (7.19), (7.20) allow to calculate R_{sh} and I_0 by knowing n and R_s parameters. The diode ideality factor (n) could be impose arbitrary to a value between 1 and 2 (extreme included), then n is set to 1,5. Moreover, a third equation is needed to calculate the series resistance ($R_{s,calc}$). This equation could be derived from the MPP definition:

$$\left(\frac{dP}{dV}\right)_{MPP} = V_{MPP} \cdot dI + I_{MPP} \cdot dV = 0 \tag{7.21}$$

$$\left(\frac{dI}{dV}\right)_{MPP} = -\frac{I_{MPP}}{V_{MPP}} \tag{7.22}$$

$$\frac{I_{MPP}}{V_{MPP}} = \left(1 - \frac{R_s \cdot I_{MPP}}{V_{MPP}}\right) \cdot \left(\frac{I_0}{n \cdot N_s \cdot V_{MPP}} \cdot X_{MPP} + \frac{1}{R_{sh}}\right) \tag{7.23}$$

$$\left(\frac{dI}{dV}\right)_{MPP} = -\frac{I_0}{n \cdot N_s \cdot V_{MPP}} \cdot \left(1 - \frac{R_s \cdot I_{MPP}}{V_{MPP}}\right) \cdot X_{MPP} - \frac{1}{R_{sh}} \cdot \left(1 - \frac{R_s \cdot I_{MPP}}{V_{MPP}}\right) \tag{7.24}$$

$$R_{s,cal} = \frac{V_{MPP}}{I_{MPP}} - \frac{1}{\left(\frac{I_0}{n \cdot N_s \cdot V_{MPP}} \cdot X_{MPP} + \frac{1}{R_{sh}}\right)} \tag{7.25}$$

The equations (7.11), (7.12), (7.13), (7.19), (7.20), (7.25) are implemented in an iterative process where R_s is increased from 0 with a step of 10^{-5}. The iteration process ends when R_s and $R_{s,cal}$ are matching.

The analytical-numerical method described above is used in both optimization procedures to calculate the initial conditions.

7.2.3. Calculation of deviation from experimental data

The deviation from experimental data is calculated with two indicators: the *NRMSE* and the percentage error on the MPP.

The Normalized Root Mean Square Error (*NRMSE*) is used to compute the error between the experimental current and the estimated current from the equation (7.3) with the optimized parameters. This operation is performed using the expression (7.26).

$$NRMSE_I = \frac{\sqrt{\frac{\sum_{i=1}^{N_{points}} \left(I_{model} - I_{exp}\right)^2}{N_{points}}}}{\frac{\sum_{i=1}^{N_{points}} I_{exp}}{N_{points}}} \cdot 100 \tag{7.26}$$

Where:

- $NRMSE_I$ is the normalized root mean square error on the current (%)
- I_{exp} is the experimental current value (A)
- I_{model} is the estimated current from the equation (7.3), $I_{model} = f\left(V_{exp}\right)$ (A)
- V_{exp} is the experimental voltage value (V)
- N_{points} is the number of points in the experimental *I-V* curve (-)

The percentage error on the maximum power point is computed using the expression (7.27).

$$Err_{maxP} = \frac{P_{MPP,model} - P_{MPP,exp}}{P_{MPP,exp}} \cdot 100 \tag{7.27}$$

Where:

- Err_{maxP} is the percentage error on the maximum power point (%)
- $P_{MPP,exp}$ is the experimental power at MPP (W)
- $P_{MPP,model}$ is the model power at MPP (W)

Chapter 8

Parameters Correlations

The "Correlations" step consists in the identification of a surface that approximates the trend of each parameter in irradiance and/or in temperature. Each parameter is fitted with correlation expressed in literature, according to [35]. The curve fitting consists in the solution of nonlinear regression form. The method uses the MATLAB fitting function based on the Levenberg Marquart algorithm. The main output from the "Correlation" step is a matrix that contains the optimized coefficients. The graphical interface and the software operation are presented in the next two sub-chapters.

8.1. Graphical interface for correlations

The graphical interface is designed to contain all the needed settings in the simplest manner. Figure 8.1 shows the interface when the section is open.

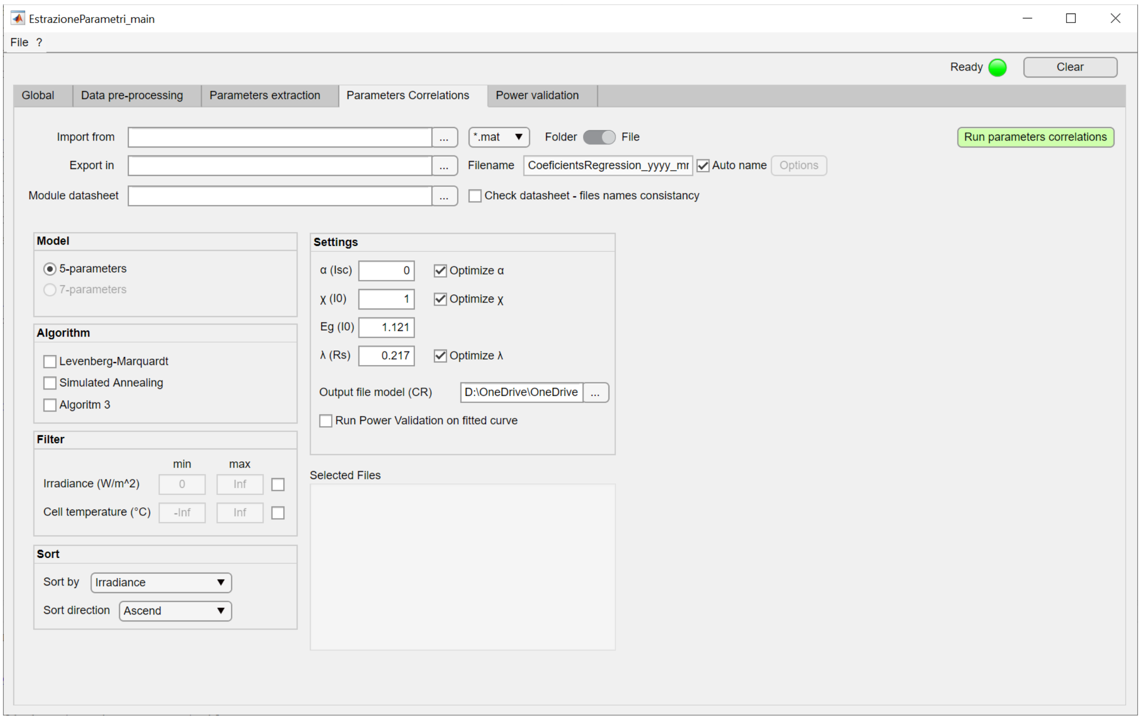

Figure 8.1: Picture of the graphical user interface tab for the parameters correlation

The import/export section, in the upper part, works in the same way as the data preprocessing, described in 6.1.1.

The settings for the parameters correlation procedure are grouped in five panels. The first panel, called “Model”, gives the possibility to choose between 5 and 7 parameters model. The second panel, called “Algorithm”, gives the possibility to choose which parameters dataset elaborate. The third panel is “Filter” and it gives the possibility to filter the parameters sets by irradiance and temperature. The fourth panel, “Sort”, gives the possibility to sort by irradiance or temperature the output file. The last panel, “Settings”, contains all the settings for the correlation procedure. These settings consist in some flags deciding which coefficient shall be analyzed. Moreover, there are some edit fields specifying the coefficient value (optimization disable) or the initial value (optimization enable).

8.2. Equation for parameters correlations

The software operation for parameters correlations is analyzed in this sub-chapter. This part consists in the application of a nonlinear fitting procedure to the equations in this section. The correlations obtained are valid only for the five parameters model (i.e. I_{ph}, I_0, n, R_s, R_{sh}).

8.2.1. Photogenerated current correlation

The photogenerated current has a trend proportional to the irradiance and linear with the temperature, according to [35]. The following equation is optimized:

$$I_{ph} = I_{ph,STC} \cdot \left(1 + \left(\alpha \cdot \left(T_c - T_{c,STC}\right)\right)\right) \cdot \frac{G}{G_{STC}} \tag{8.1}$$

Where:

- I_{ph} is the photogenerated current of the five parameters model (A)
- $I_{ph,STC}$ is the photogenerated current in STC (A)
- G is the module irradiance ($\mathrm{W \cdot m^{-2}}$)
- G_{STC} is the module irradiance in STC ($\mathrm{W \cdot m^{-2}}$)
- T_c is the cell temperature (K)
- $T_{c,STC}$ is the cell temperature in STC (K)
- α is the short circuit temperature coefficient ($\mathrm{K^{-1}}$)

The optimization coefficients are $I_{ph,STC}$ and α. In particular, α can be optimized or fixed to a specific value (i.e. from the datasheet)

8.2.2. Saturation current correlation

The diode saturation current has a cubic trend proportional to the temperature, according to [35]. The equation (8.2(8.2) is optimized in monocrystalline technology.

$$I_0 = I_{0,STC} \cdot \left(\frac{T_c}{T_{c,STC}}\right)^3 \cdot \exp\left(\left(\frac{E_{g,STC}}{T_{STC}} - \frac{E_g(T_c)}{T_c}\right) \cdot \frac{1}{k_B}\right) \tag{8.2}$$

$$E_g(T_c) = E_{g,STC} \cdot \left(1 - 0{,}0002677 \cdot \left(T_c - T_{c,STC}\right)\right) \tag{8.3}$$

$$\text{(for m-Si @ 298 K)} \qquad E_{g,STC} = 1{,}121 \cdot q_e \tag{8.4}$$

Where:

- I_0 is the diode saturation current (A)
- $I_{0,STC}$ is the diode saturation current in STC (A)
- $E_g(T_c)$ is the energy gap at T_c (J)
- $E_{g,STC}$ is the energy gap in STC (J)
- k_B is the Boltzmann constant ($\mathrm{J \cdot K^{-1}}$)
- $q_e = 1{,}602 \cdot 10^{-19}$ C is the charge of the electron

The equation above is studied in detail only for some technologies because the energy gap is well known in specific cases. (i.e. monocrystalline silicon, amorphous silicon, etc.). A new adimensional empirical coefficient χ is added to take in account the different behaviors of the energy gap of other specific technologies (es. HIT). The following equation is optimized in case of no standard technologies.

$$I_0 = I_{0,STC} \cdot \left(\frac{T_c}{T_{c,STC}}\right)^3 \cdot \exp\left(\chi \cdot \left(\frac{E_{g,STC}}{T_{STC}} - \frac{E_g(T_c)}{T_c}\right) \cdot \frac{1}{k_B}\right) \tag{8.5}$$

The optimization coefficients are $I_{0,STC}$ and χ. In particular, χ can be optimized or fixed to a specific value (i.e. $\chi = 1$ to use equation (8.2)).

8.2.3. Ideality factor correlation

The diode ideality factor has a slightly trend with the irradiance and temperature according to [36]. The following equation is optimized:

$$n = a + b \cdot G + c \cdot T_c \tag{8.6}$$

Where

- n is the diode ideality factor (-)
- a is the intercept term (-)
- b expresses the linear effect in irradiance ($\mathrm{W}^{-1} \cdot \mathrm{m}^2$)
- c expresses the linear effect in module temperature (C^{-1})

The optimization coefficients are a, b, c.

8.2.4. Series resistance correlation

The series resistance has a trend proportional to the temperature and logarithmical to the irradiance, according to [35]. The following equation is optimized:

$$R_s = R_{s,STC} \cdot \frac{T_c}{T_{c,STC}} \cdot \left(1 - \lambda_{R_s} \cdot \log\left(\frac{G}{G_{STC}}\right)\right) \tag{8.7}$$

Where:

- R_s is the series resistance (Ω)
- $R_{s,STC}$ is the series resistance at STC (Ω)
- λ_{R_s} is an empirical coefficient that expresses proportionality to the logarithmic variation of the irradiance (-)

The optimization coefficients are $R_{s,STC}$, λ_{R_s}.

8.2.5. Shunt resistance correlation

The shunt resistance has a trend inversely proportional to the irradiance, according to [35]. The following equation is optimized:

$$R_{sh} = R_{sh,STC} \cdot \frac{G_{STC}}{G} \tag{8.8}$$

Where:

- R_{sh} is the shunt resistance (Ω)
- $R_{sh,STC}$ is the shunt resistance in STC (Ω)

The optimization coefficient is $R_{sh,STC}$.

8.2.6. Normalized Root Mean Square Error (*NRMSE*)

The Normalized Root Mean Square Error (*NRMSE*) is used to compute the errors between the experimental points and the fitting surfaces. This operation is performed for the 5 parameters of the model using the same expression (8.9). The X symbols can be replaced by the symbol of the parameter analyzed (i.e. I_{ph}, I_0, n, R_s, R_{sh}).

$$NRMSE_X = \frac{\sqrt{\frac{\sum_{i=1}^{N_{points}} \left(X_{cor} - X_{exp}\right)^2}{N_{points}}}}{\frac{\sum_{i=1}^{N_{points}} X_{exp}}{N_{points}}} \cdot 100 \tag{8.9}$$

Where:

- $NRMSE_X$ is the normalized root mean square error for parameter X (%)
- X_{exp} is the experimental parameter value
- X_{cor} is the estimation from correlation parameter value
- N_{points} is the number of points in the experimental samples

Chapter 9

Power and Energy computation

The last step of this research consists in the maximum power point and energy estimation from the weather condition (module irradiance and temperature). The graphical interface and the software operation are presented in the next two section.

9.1. Graphical interface for energy

The graphical interface is designed to contain all the needed settings in the simplest manner. Figure 9.1 shows the interface when the section is open.

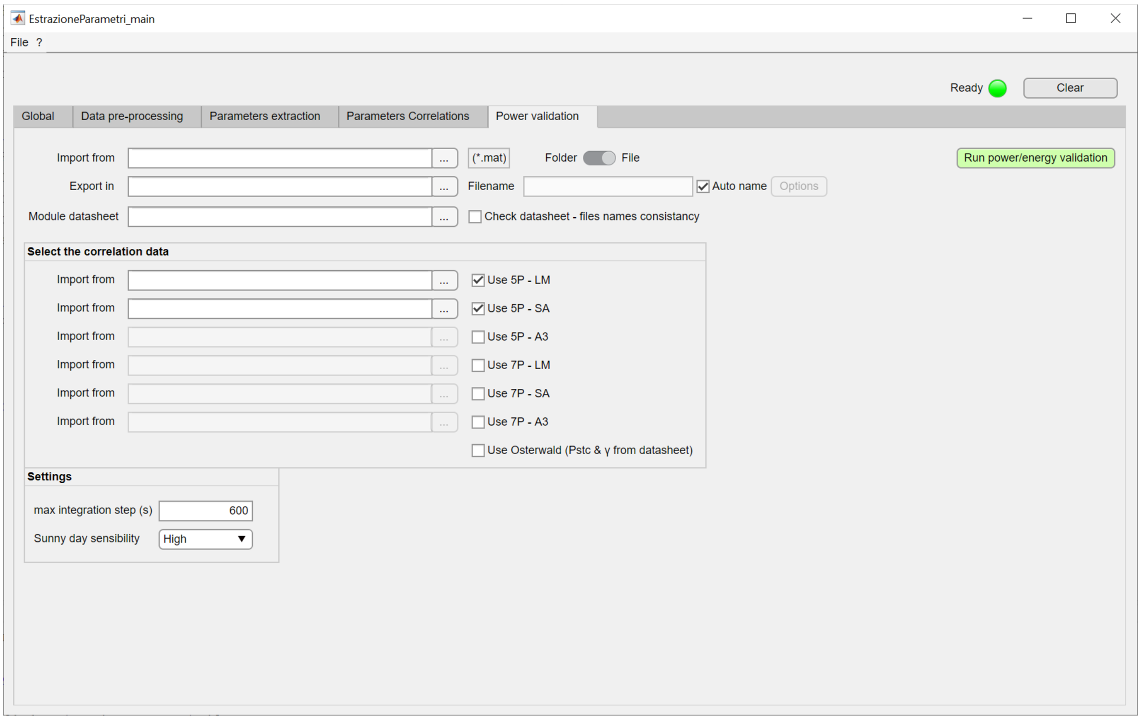

Figure 9.1: Picture of the graphical user interface tab for the power and energy computation

The import/export section, in the upper part, works in the same way as the data preprocessing, described in 6.1.1.

The settings for the Power and Energy computation procedure are grouped in two panels. The first panel, called "Select the correlation data", gives the possibility to select the mat files with the optimization coefficient. These files are the output of the parameters correlation procedure. The second panel, called "Settings", gives the possibility to choose the maximum time between two consecutive power points in the integration of energy. Moreover, there is the possibility to choose the sensibility of the division among three types of days (sunny, partly cloudy, cloudy).

9.2. Equation for Power and Energy computation

The procedure receives as input an experimental set of data, the module datasheet information, and the correlation coefficients of each model. The experimental set of data can be different from the data imported for parameters and correlation analysis.

The estimation of the power is calculated with the application of the correlation described in 8.2. The five parameters (i.e. I_{ph}, I_0, n, R_s, R_{sh}) are calculated from the coefficients (i.e. $I_{ph,STC}$, α, $I_{0,STC}$, χ, a, b, c, $R_{s,STC}$, λ, $R_{sh,STC}$) for a given couple of irradiance and temperature (G, T_c). Then, the parameters are used to draw the I-V curve and the maximum power point is found on the curve. After that, the power is calculated with the Osterwald method to compare the two approaches. The Osterwald equation [37] is reported below (9.1).

$$P_{Osterwald} = P_{STC} \cdot \frac{G}{G_{STC}} \cdot \left(1 + \frac{\gamma}{100} \cdot \left(T_c - T_{c,STC}\right)\right) \tag{9.1}$$

Where

- $P_{Osterwald}$ is the power calculated by the Osterwald method (W)
- P_{STC} is the power in STC from the datasheet (W)
- γ is the power thermal coefficients ($\% \cdot \mathrm{K}^{-1}$)
- G is the module irradiance ($\mathrm{W} \cdot \mathrm{m}^{-2}$)
- T_c is the module temperature (K)
- G_{STC} is the irradiance in STC (i.e. $1000\ \mathrm{W} \cdot \mathrm{m}^{-2}$)
- $T_{c,STC}$ is the module temperature in STC (i.e. 298,15 K)

The goodness of the power estimation may be assessed with the Normalized Root Mean Square Error (*NRMSE*) between the experimental power and the estimated ones. This computation is performed for each model using the same expression (9.2).

$$NRMSE_{P_{MPP}} = \frac{\sqrt{\frac{\sum_{i=1}^{N_{points}} \left(P_{MPP,model} - P_{MPP,exp}\right)^2}{N_{points}}}}{\frac{\sum_{i=1}^{N_{points}} P_{MPP,exp}}{N_{points}}} \cdot 100 \tag{9.2}$$

Where:

- $NRMSE_{P_{MPP}}$ is the normalized root mean square error on the power at MPP (%)
- $P_{MPP,exp}$ is the experimental power at MPP (W)
- $P_{MPP,model}$ is the estimated power at MPP with the model under exam (W)
- N_{points} is the number of points in the dataset (-)

The estimation of energy is computed with the integration in time of the maximum power point value. The integration is made by the rectangular rule (base multiplied for height) and the MPP is adopted as the midpoint of the integration (see Figure 9.2). Furthermore, a maximum time step is imposed in order to avoid the integration on a large time step (e.g. lack of measurement acquisition, time between sunset and sunrise). The mathematical steps for calculating energy are reported in the following lines.

$$E = \int_{t_1}^{t_2} p(t) \cdot dt \approx \sum_{i=1}^{N_{tot}} \Delta \mathrm{t}_\mathrm{i}^* \cdot P_{MPP,i} \tag{9.3}$$

Where:

- E is the energy in the considered period (i.e day, month, year, etc.) (J)
- $p(t)$ is the power over the time (W)
- N_{tot} is the number of curves in the time interval considered (-)
- $P_{MPP,i}$ is the maximum power for each step (W)
- $\Delta \mathrm{t}_\mathrm{i}^*$ is the integration time step used to compute the energy (s)

$$\Delta \mathrm{t}_\mathrm{i}^* = \begin{cases} \Delta t_i & \Delta t_i \leq \Delta t_{max} \\ \Delta t_{max} & \Delta t_i > \Delta t_{max} \end{cases} \tag{9.4}$$

Where:

- Δt_i is the computed time step by equation (9.5) (see Figure 9.2) (s)
- Δt_{max} is the maximum integration step admissible (s)

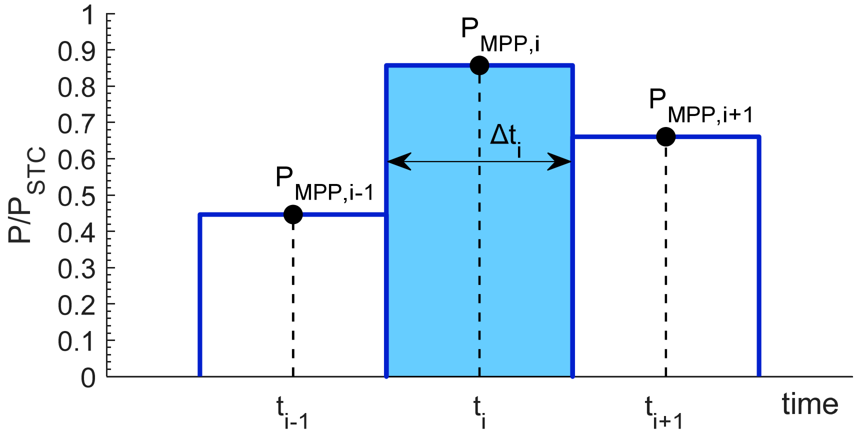

Figure 9.2: Computation of the integration time

$$\begin{cases} \Delta t_i = \dfrac{t_{i+1} - t_i}{2} & i = 1 \\ \Delta t_i = \dfrac{t_i - t_{i-1}}{2} + \dfrac{t_{i+1} - t_i}{2} & \forall i \neq 1, N_{tot} \\ \Delta t_i = \dfrac{t_i - t_{i-1}}{2} & i = N_{tot} \end{cases} \tag{9.5}$$

Where:

- Δt_i is the computed time step by equation (9.5) (see Figure 9.2) (s)
- t_i is the time at the actual time instant (s)
- t_{i-1} is the time at the previous time instant (s)
- t_{i+1} is the time at the next time instant (s)

The goodness of the energy estimation may be assessed with the percentage error between the experimental energy and the estimated ones. This computation is performed for each model using the expression (9.6).

$$Err_E = \frac{E_{model} - E_{exp}}{E_{exp}} \cdot 100 \tag{9.6}$$

Where:

- Err_E is the percentage error on the energy (%)
- E_{exp} is the experimental energy (J)
- E_{model} is the estimated energy with each model (J)

Three types of days are identified to evaluate the power *NRMSE* and the energy percentage error. These days, divided according the sky profile, are sunny, partly cloudy, and cloudy days. Firstly, the sunny days should present a regular shape of the irradiance during all day. These days are identified thanks to the sunny day filter described in section 6.2.2. Secondly, the partly cloudy days may show a shape of the irradiance where it is possible to recognize the typical shape with some local minimum. These days are identified comparing the measured irradiance profile to the expected one from PVGIS data. Lastly, the cloudy days do not show any regular irradiance shape. These days are the ones that do not respect the sunny and partly cloudy criteria.

Another division is made on the irradiance to evaluate the power *NRMSE* at three different irradiance levels: low, medium, and high. Low irradiance indicates $0 \leq G < 400$ W/m^2, medium irradiance implies $400\ W/m^2 \leq G < 800\ W/m^2$, and high irradiance means $800\ W/m^2 \leq G < 1200\ W/m^2$.

Chapter 10

Experimental data acquisition campaign

The experimental data used in this thesis will be commented in this chapter. This thesis is partially developed during the exceptional circumstances caused by COVID-19 pandemic outbreak. Consequently, the planned experimental campaign here involved could not be completed. Therefore, data from a previous experimental campaign carried out in 2012 is used to overcome the lockdown aftermaths. This campaign was conducted with a Sanyo HIT 240-HDE4 module.

The HIT 240-HDE4 module's specifications are reported in the Annex C. The module was calibrated by the CIEMAT accredited laboratory before the beginning of the experimental campaigns. Table 10.1 and Table 10.2 reports the main specification from the manufacturer datasheet and the calibration certificate. The "CIEMAT lab" values are measured in STC inside a sun simulator while the "CIEMAT sun" values are actually measured with sun rays and reported in STC.

Source	P_{MPP} (W)	V_{oc} (V)	I_{sc} (A)	V_{MPP} (V)	I_{MPP} (A)	FF (%)
Manufacturer	240	43,6	7,37	35,5	6,77	-
CIEMAT lab	233,3	42,24	7,54	32,29	7,23	73,3
CIEMAT sun	239,1	42,62	7,42	-	-	75,8

Table 10.1: Specifications of the HIT module.

Source	Temperature coeff P_{MPP} (%/°C)	Temperature coeff V_{oc} (V/°C)	Temperature coeff I_{sc} (mA/°C)
Manufacturer	-0,30	-0,109	-2,21

Table 10.2: Temperature coefficients of the HIT module.

The experimental measurement campaign of HIT module was carried out between January and December 2012. Throughout these 12 months of measurement, the module was tested in different weather conditions and 21'362 measures were acquired (and only 14'367 are reliable). A series of charts is reported in the next pages, in order to show the conditions in which the measures took place. The first analysis in Figure 10.1 is made to see the distribution of the most important weather conditions using the histogram representations. The irradiation data were recorded at high GTI due to the sun tracking, especially into the ranges between 950 and 1100 W/m². Instead, the module temperature shows a more widespread tendency thanks to the full year campaign, mainly covering the ranges between 35 and 65 °C. Furthermore, a high quantity of measurements is recorded under scattered air temperature, and low wind speed values (below 5 m/s).

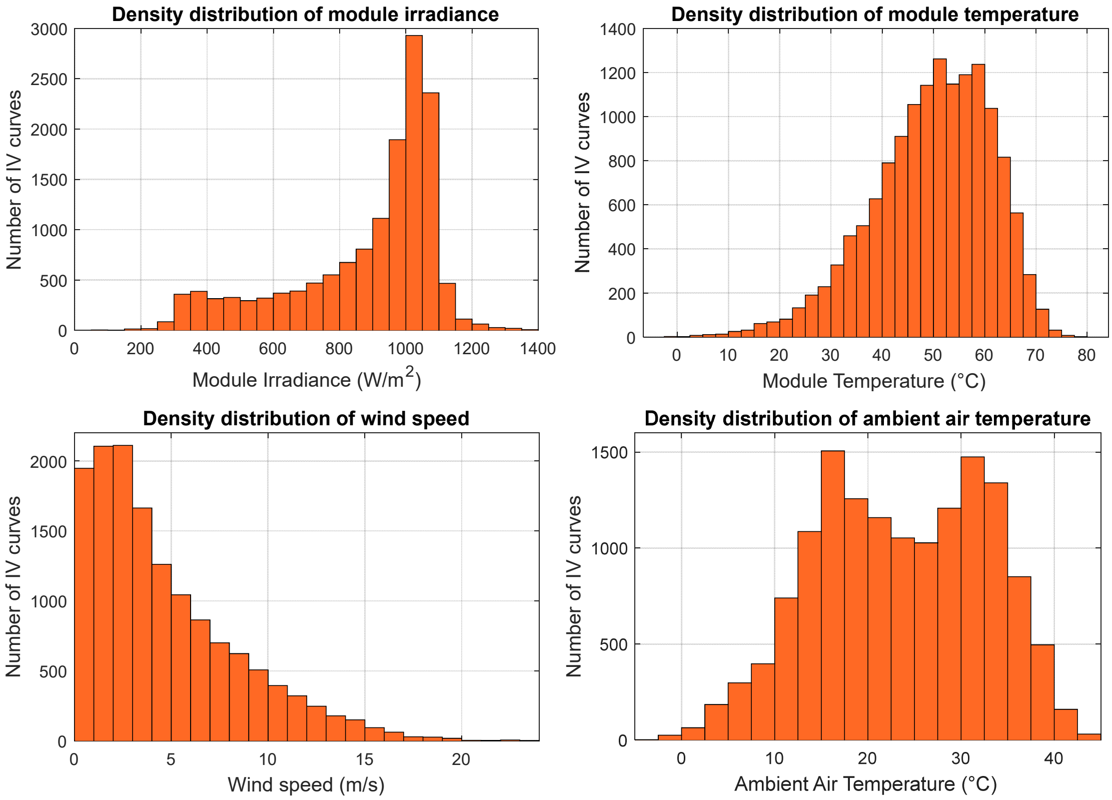

Figure 10.1: Density distribution of the main four environment conditions for HIT module.

The next analysis in Figure 10.2 and Figure 10.3 concerns the irradiance and temperature reliability because the module's output power is mainly affected by these two quantities. Firstly, the irradiance from the pyranometers and the irradiance calculated from the short circuit current are compared. The result is shown in Figure 10.2. Then, the module temperature from the Pt100 probe and the temperature from the NOCT equation are compared. The result is shown in Figure 10.3. Moreover, some parts are white without data because the information was not reliable, or the system did not work for maintenance.

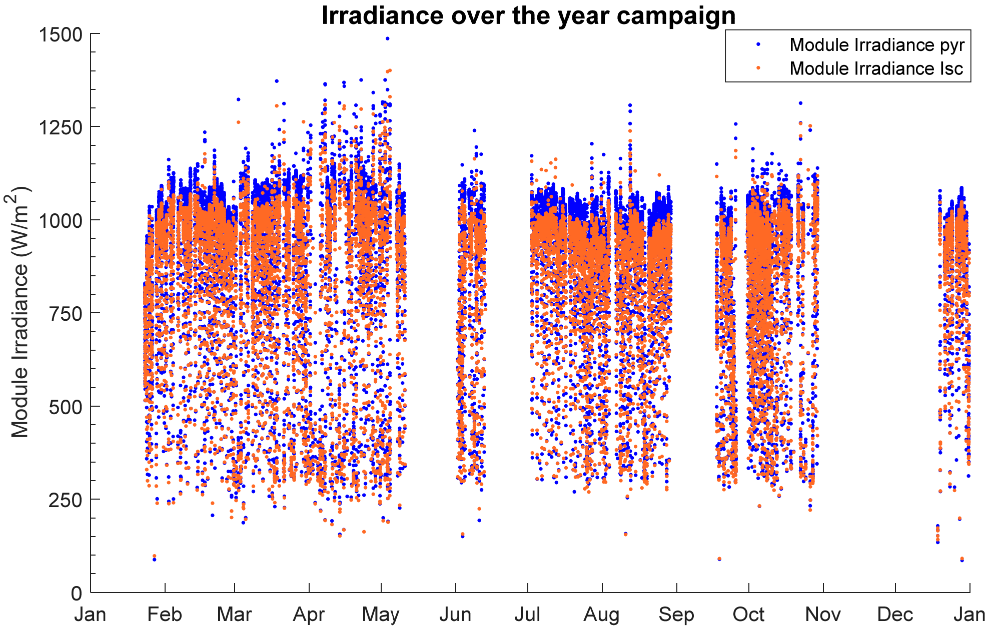

Figure 10.2: Irradiances during the year

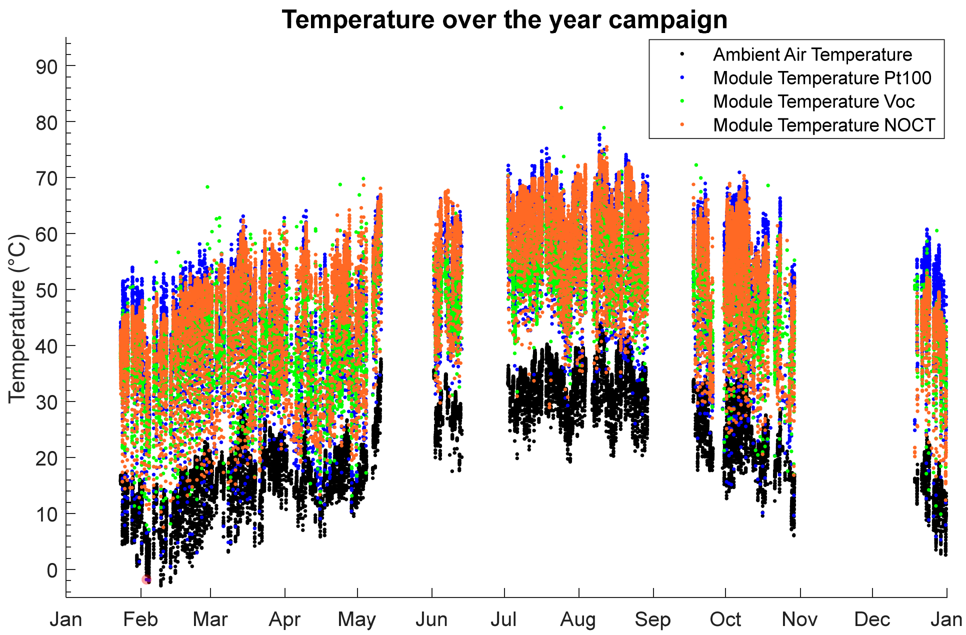

Figure 10.3: Temperatures during the year

The parameters extraction is made on a limited dataset which only involves the use of 417 *I-V* curves. This dataset is composed of all the reliable *I-V* curves for parameters extraction. Figure 10.4 shows the couples of irradiance and temperature of the *I-V* curves.

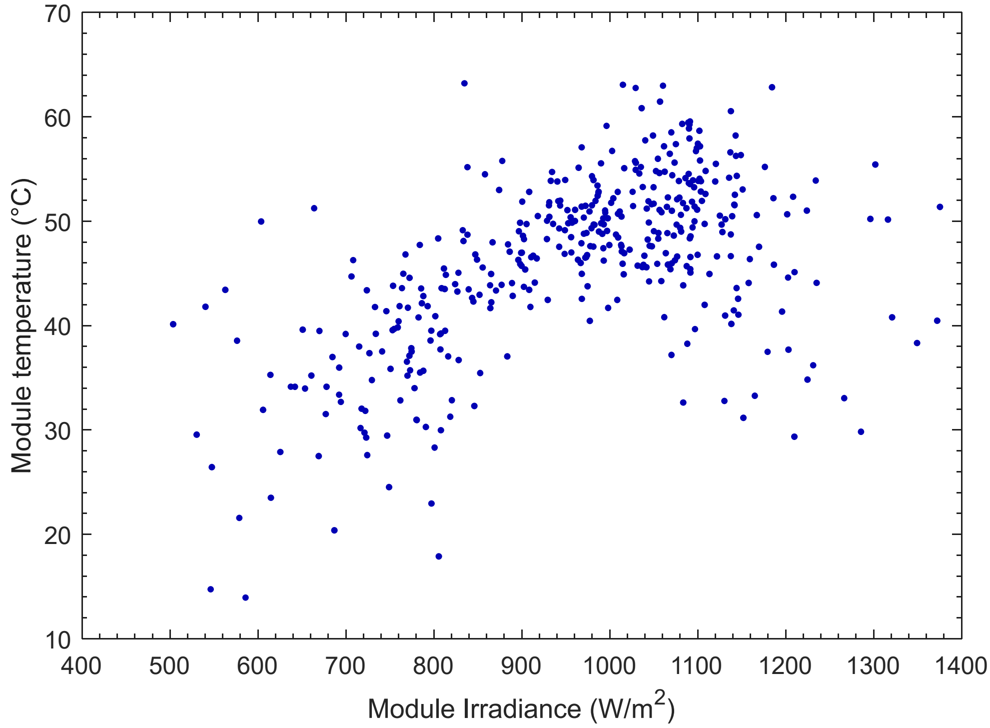

Figure 10.4: Irradiance and temperature of the *I-V* curves for parameters extraction

The power validation is performed on a mismatch filtered dataset of 10630 curves. This data is obtained from the Global dataset with the application of mismatch detector (medium level).

In summary, four datasets are used in this thesis:

- Raw dataset with all the acquisition (21'362 *I-V* curves)
- Global dataset with all the reliable data (14'367 *I-V* curves)
- Mismatch filtered dataset (10'630 *I-V* curves)
- Parameters extraction dataset (417 *I-V* curves)

Chapter 11

Analysis of obtained results

The analysis of the heterojunction with intrinsic thin layer module (HIT) will be presented in this chapter. The chapter is organized as follows. Firstly, the results of the parameter extraction are reported. Then, the founded correlations for each parameter are presented. At the end, the power and energy results are shown. The analysis is carried out with two optimization methods, the Levenberg-Marquardt (LM) and Simulated Annealing and Nelder Med (SA-NM), to assess the goodness of each procedure. Generally, the LM results are marked in orange whereas the SANM in green, in order to simplify the reading.

11.1. Parameters extraction results

The two optimization algorithms can find different sets of parameters. Nonphysical solutions, to be discarded, are present in this set of parameters. Therefore, the final results can be slightly different. In the case under study, 417 sets of parameters are elaborated for both the LM and SA-NM algorithm. Then, the LM algorithm leads to a set of 357 feasible curves while the SA-NM method leads to a set of 335 feasible curves. The results of the parameters extraction with the five parameters model are reported and discussed in this section.

The first analysis in Figure 11.1 presents a set of *I-V* curves at different irradiance. This figure shows the experimental points and their trend line. Moreover, the trend line is drawn using the extracted parameters of the LM algorithm.

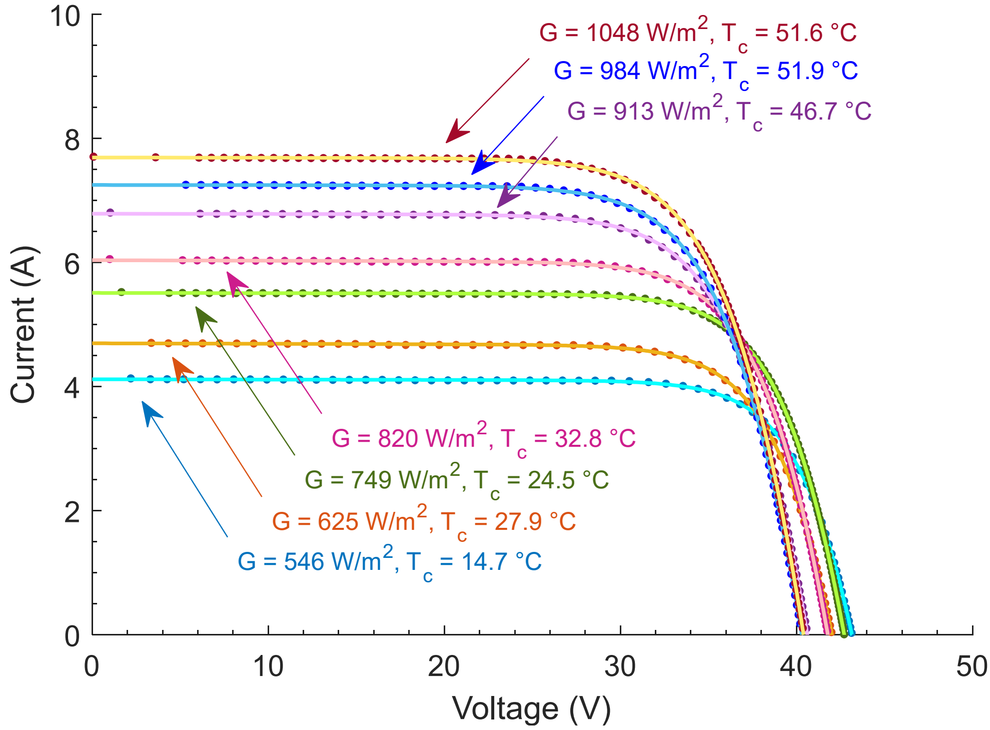

Figure 11.1: *I-V* curves experimentally measured (dots) and trend estimated with the LM parameters

The Levenberg-Marquardt algorithm correctly fits the experimental data in all the examined conditions. The *NRMSE* is a good benchmark value to define the efficiency of the fitting. The *NRMSE* value for this set of data ranges from 0,15% to 0,46% using the LM algorithm. The extraction with Simulated Annealing and Nelder-Mead algorithm leads to similar results. Therefore, the SA-NM graph is not shown. Finally, The *NRMSE* value ranges from 0,36% to 0,55% using the SA-NM method.

The second analysis in Figure 11.2 and Figure 11.3 shows the error distribution at the maximum power point for the LM and SA-NM algorithms. An analysis dedicated to MPP is performed because this point is the most important in the *I-V* curve for the energy estimation. In fact, a PV generator is usually equipped with a maximum power point tracking technique.

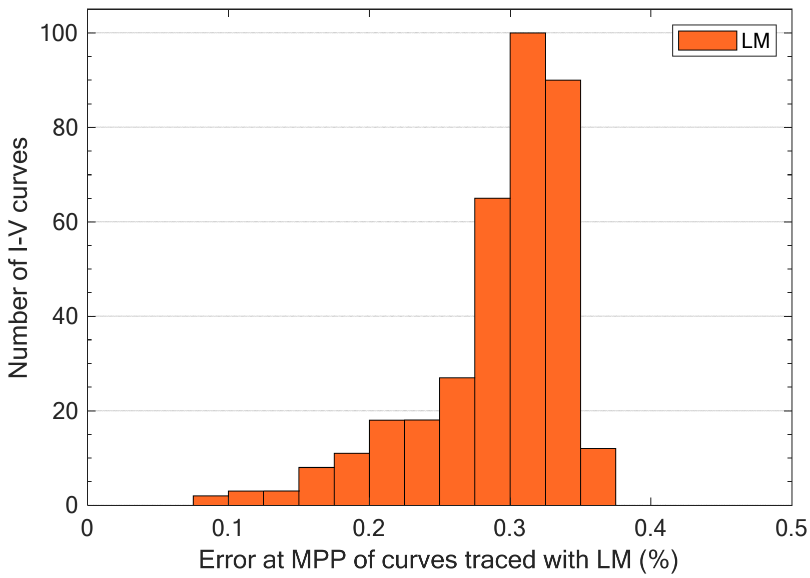

Figure 11.2: Distribution of the error at MPP for curves traced with LM method

Figure 11.2 shows that the error at the maximum power point is concentrated in a range of less than 0,4% for the LM algorithm. Besides, it can be observed that most of the curves have an error of 0,3%. These data show that the extraction is carried out correctly.

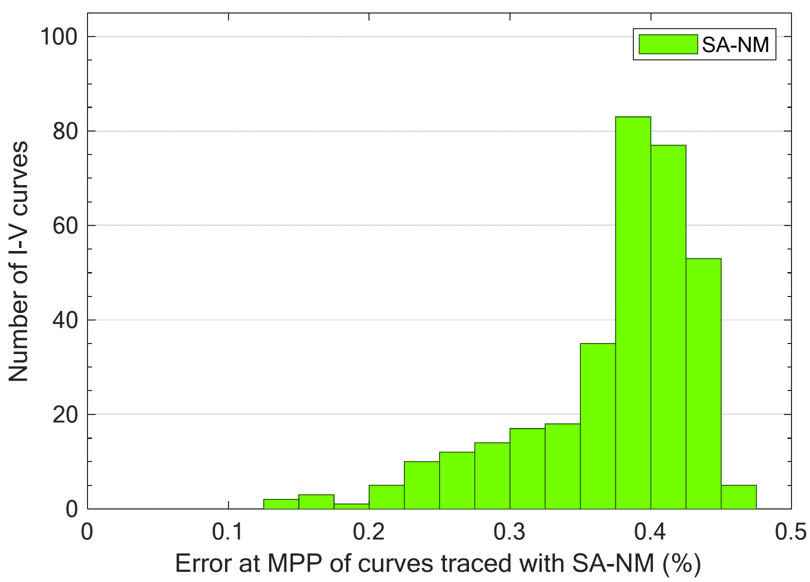

Figure 11.3: Distribution of the error at MPP for curves traced with SA-NM method

Figure 11.3 shows that the error at the maximum power point is concentrated in a range of less than 0,5% for the SA-NM algorithm. Besides, it can be observed that most of the curves have an error of 0,4%. This method also leads to correct values, but the error is slightly greater than in the LM.

The latest comparison of the algorithms in the context of parameter extraction concerns the computation times.

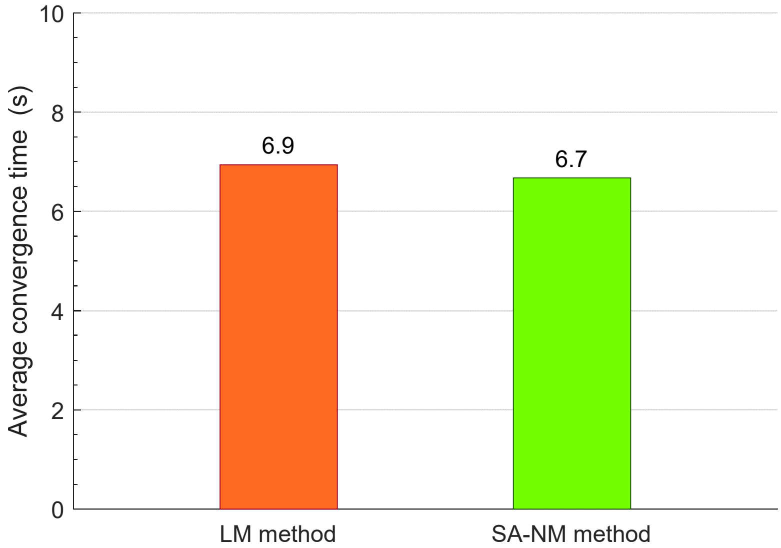

Figure 11.4: Average time to extract the five parameters

Figure 11.4 shows that the average time to optimize the parameters is similar for the two methods. However, the LM algorithm benefits from the MATLAB Parallel Computing Toolbox while the SA-NM does not use this toolbox. Even if the LM is better from the parameter extraction, the SA-NM is better in terms of the computational effort.

The next section shows the graph of the extracted parameters together with the relative correlation.

11.2. Parameters correlations results

The correlations estimate how the five parameters vary with respect to the irradiance and cell temperature. The trend of each parameter is graphically presented for both optimization methods in the following pages. Here, the term “experimental” in the legends indicates the points found after applying the two methods. Besides, the term “correlation” indicates points out the trend that showing the correlation found. The parameters are represented in the following order: photogenerated current, diode saturation current, diode ideality factor, series resistance and shunt resistance.

Firstly, the photogenerated current (I_{ph}) presents a main dependence on the irradiance. It can be observed that the dependence on cell temperature is negligible. In addition, the correlation equation comes from the equation (8.1). The $I_{ph,STC}$ coefficient is optimized by the correlation while the α is taken from the manufacturer datasheet. Figure 11.5 and Figure 11.6 clearly show the irradiance tendence respectively for LM and SA-NM methods.

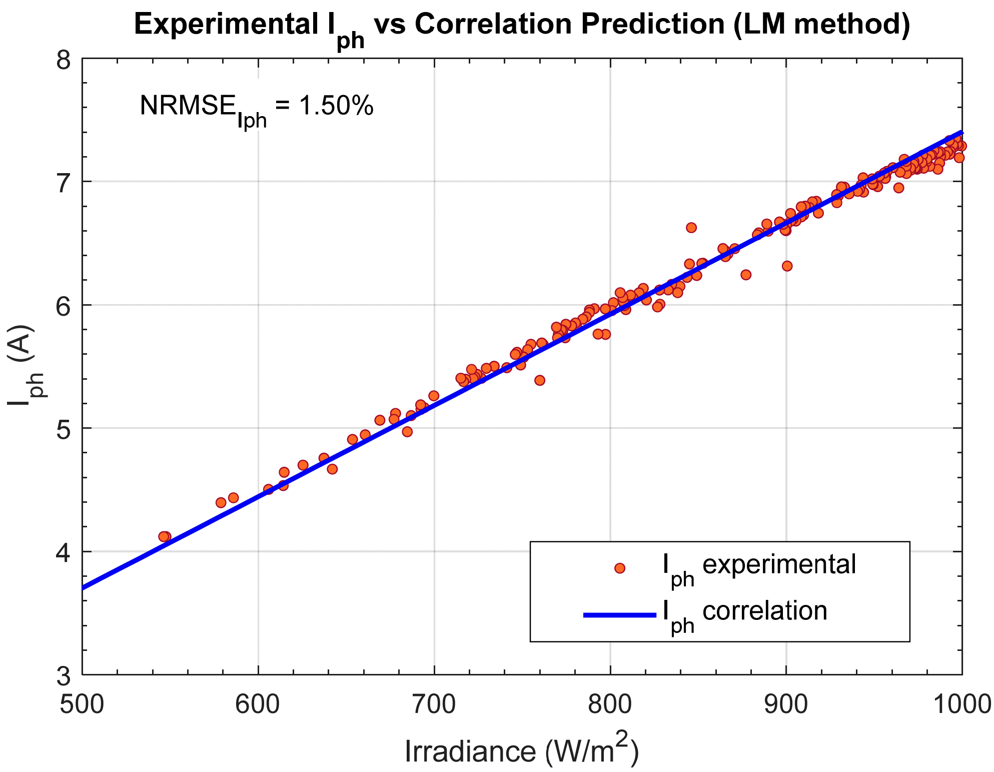

Figure 11.5: I_{ph} tendency with irradiance (LM algorithm)

$$I_{ph} = \mathbf{7,35} \cdot \left(1 + \left(0{,}3 \cdot 10^{-3} \cdot (T_c - 298)\right)\right) \cdot \frac{G}{1000} \tag{11.1}$$

The orange dots show the I_{ph} values from the LM optimization (i.e. experimental) while the blue line shows the trend of the correlation in (11.1). The goodness of the correlation is confirmed by the *NRMSE* value of 1,50%.

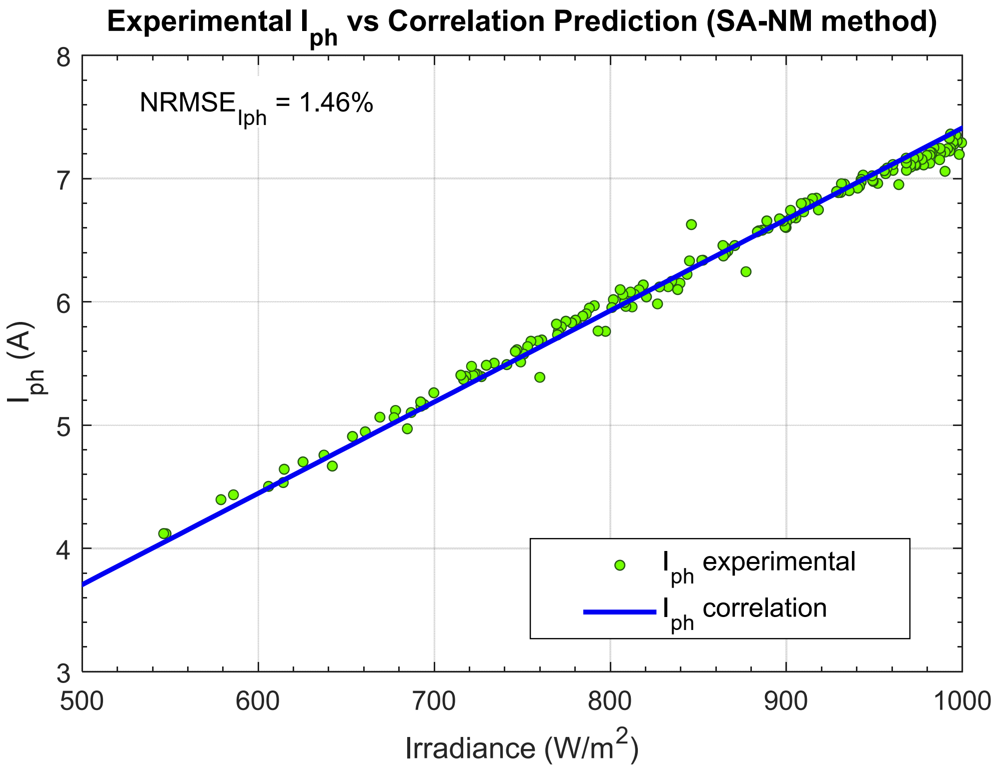

Figure 11.6: I_{ph} tendency with irradiance (SA-NM method)

$$I_{ph} = \mathbf{7,36} \cdot \left(1 + \left(0{,}3 \cdot 10^{-3} \cdot (T_c - 298)\right)\right) \cdot \frac{G}{1000} \tag{11.2}$$

The green dots show the I_{ph} values from the SA-NM optimization (i.e. experimental) while the blue line shows the trend of the correlation in (11.2). The goodness of the correlation is confirmed by the *NRMSE* value of 1,46%. However, the correlation on SA-NM data is slightly better than the one on LM data.

Secondly, the diode saturation current (I_0) presents only a dependence on the cell temperature. The correlation equation comes from the equation (8.5). The $I_{0,STC}$ and χ coefficients are optimized by the correlation. Figure 11.7 and Figure 11.8 visibly show this tendence.

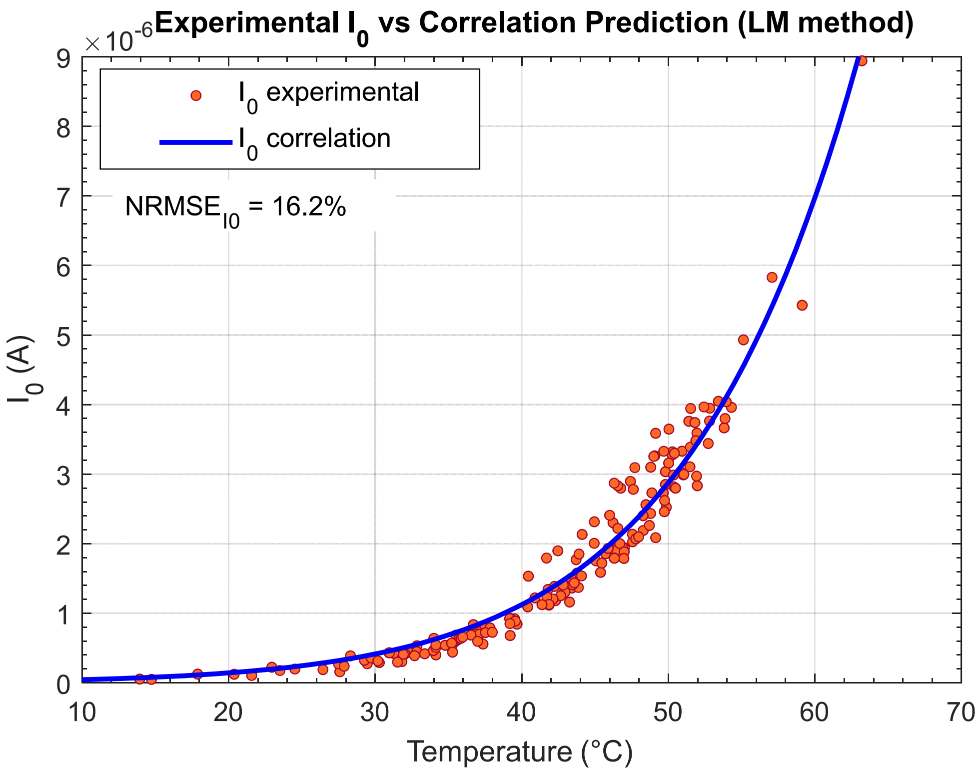

Figure 11.7: I_0 tendency with temperature (LM algorithm)

$$I_0 = \mathbf{2,25 \cdot 10^{-7}} \cdot \left(\frac{Tc}{298}\right)^3 \cdot \exp\left(\mathbf{0,61} \cdot \left(\frac{E_{g,STC}}{T_{STC}} - \frac{E_g(T_c)}{T_c}\right) \cdot \frac{1}{k_B}\right) \tag{11.3}$$

The orange dots indicate the I_0 values from the LM optimization (i.e. experimental) while the blue line shows the trend of the correlation in (11.3). The goodness of the correlation is confirmed by the *NRMSE* value of 16,2%. Moreover, this value is typical for the diode saturation current correlation.

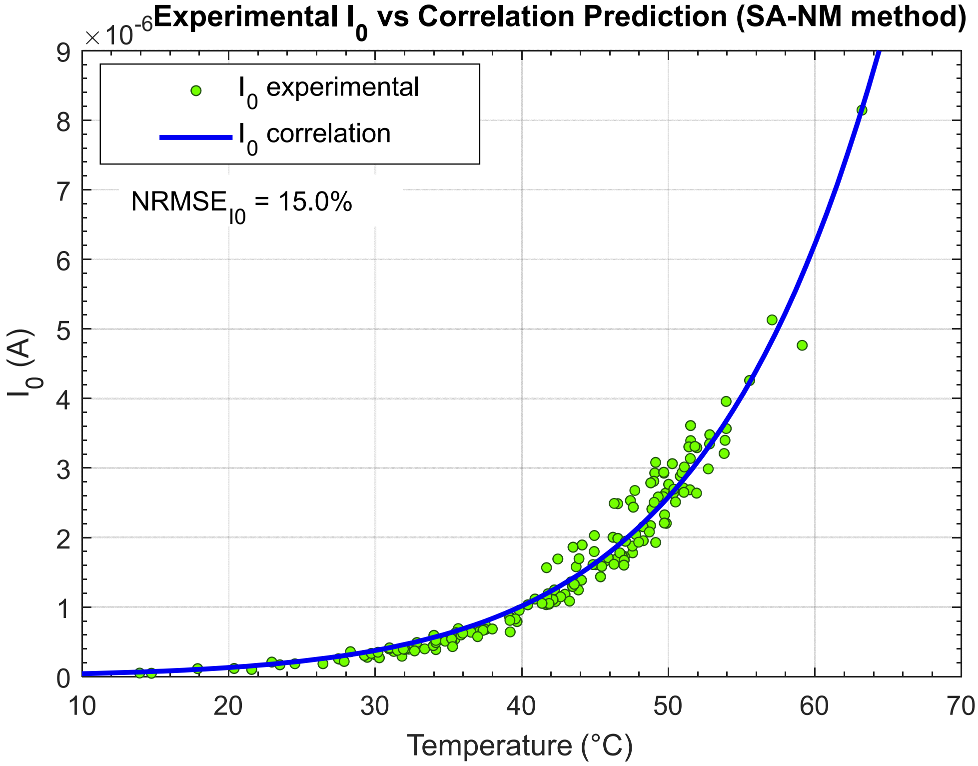

Figure 11.8: I_0 tendency with temperature (SA-NM method)

$$I_0 = \mathbf{2,46 \cdot 10^{-7}} \cdot \left(\frac{T_c}{298}\right)^3 \cdot \exp\left(\mathbf{0,60} \cdot \left(\frac{E_{g,STC}}{T_{STC}} - \frac{E_g(T_c)}{T_c}\right) \cdot \frac{1}{k_B}\right) \tag{11.4}$$

The green dots show point out the I_0 values from the SA-NM optimization (i.e. experimental) while the blue line shows the trend of the correlation in (11.4). The goodness of the correlation is confirmed by the *NRMSE* value of 15,0%. However, the correlation on SA-NM data is slightly better than the one on LM data.

Thirdly, the diode ideality factor (n) presents low variation with irradiance and cell temperature. The correlation equation comes from the equation (8.6). In addition, the a, b and c coefficients are optimized by the correlation. Figure 11.9 and Figure 11.10 evidently show the irradiance and temperature tendencies respectively for LM and SA-NM methods.

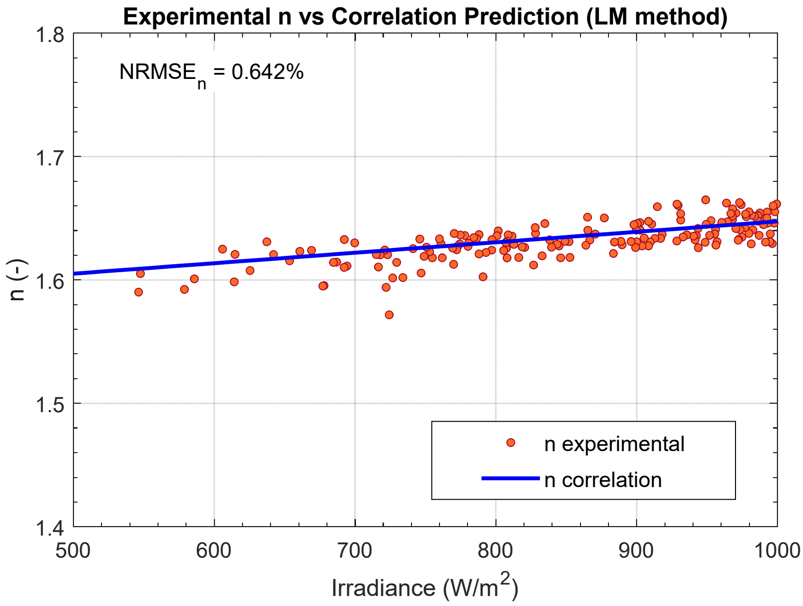

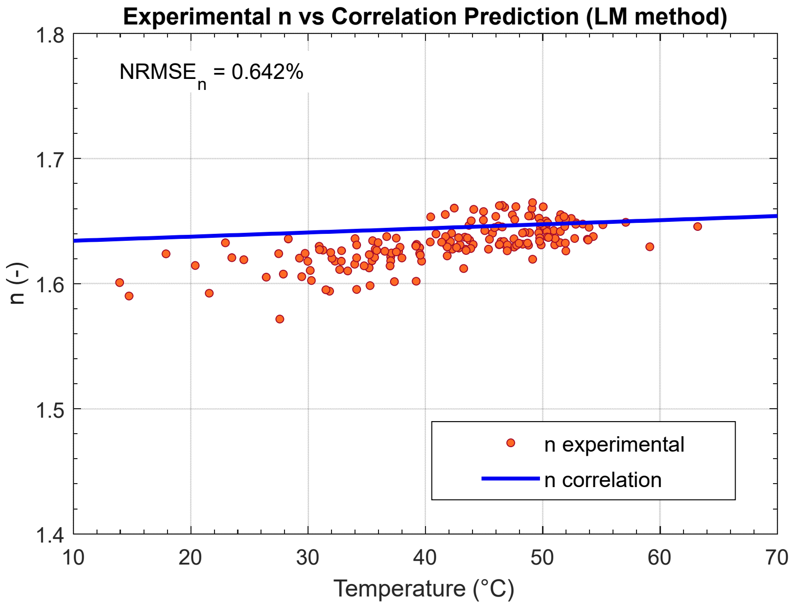

Figure 11.9: n tendency with irradiance and temperature (LM algorithm)

$$n = \mathbf{1,46} + \mathbf{8,47 \cdot 10^{-5}} \cdot G + \mathbf{3,29 \cdot 10^{-4}} \cdot T_c \tag{11.5}$$

The orange dots highlight the n values from the LM optimization (i.e. experimental) while the blue line shows the trend of the correlation in (11.5). The goodness of the correlation is confirmed by the *NRMSE* value of 0,642%. Finally, this value is typical for the diode ideality factor correlation. The ideality factor shows an increase tendency with both irradiance and temperature.

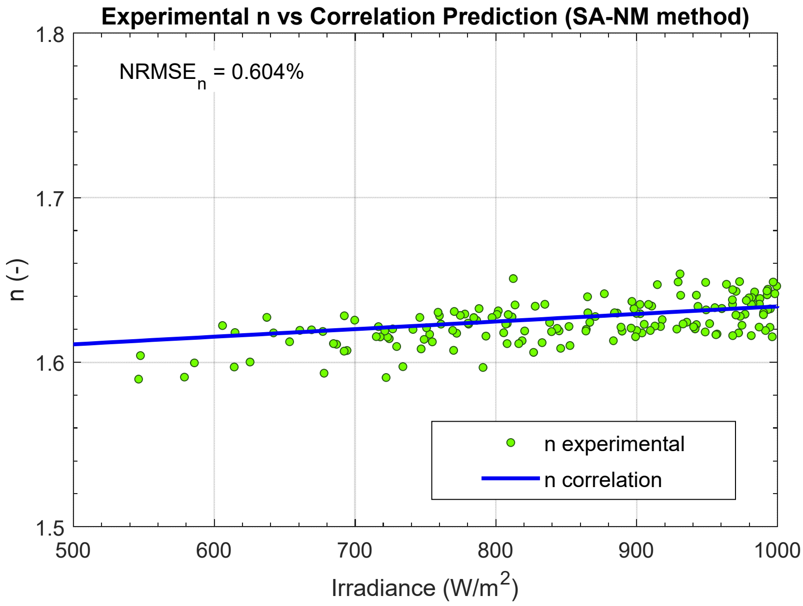

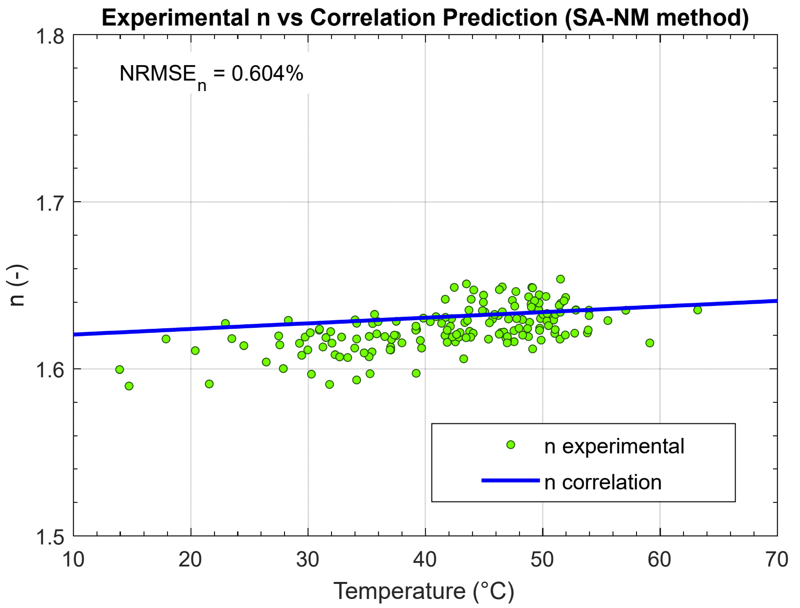

Figure 11.10: n tendency with irradiance and temperature (SA-NM method)

$$n = \mathbf{1,48} + \mathbf{4,61 \cdot 10^{-5}} \cdot G + \mathbf{3,36 \cdot 10^{-4}} \cdot T_c \tag{11.6}$$

The green dots show the n values from the SA-NM optimization (i.e. experimental) while the blue line represents the trend of the correlation in (11.6). The goodness of the correlation is confirmed by the *NRMSE* value of 0,604%. However, the correlation on SA-NM data is slightly better than the one on LM data. Moreover, the dependence is similar in irradiance and temperature. Therefore, two 3D plots are used to understand the double dependency on irradiance and temperature and they are proposed in Annex D.

Fourthly, the series resistance (R_s) shows variation with irradiance and cell temperature. The correlation equation comes from the equation (8.7). The $R_{s,STC}$ and λ_{R_s} coefficients are optimized by the correlation. Figure 11.11 and Figure 11.12 evidently report the irradiance and temperature tendencies respectively for LM and SA-NM methods.

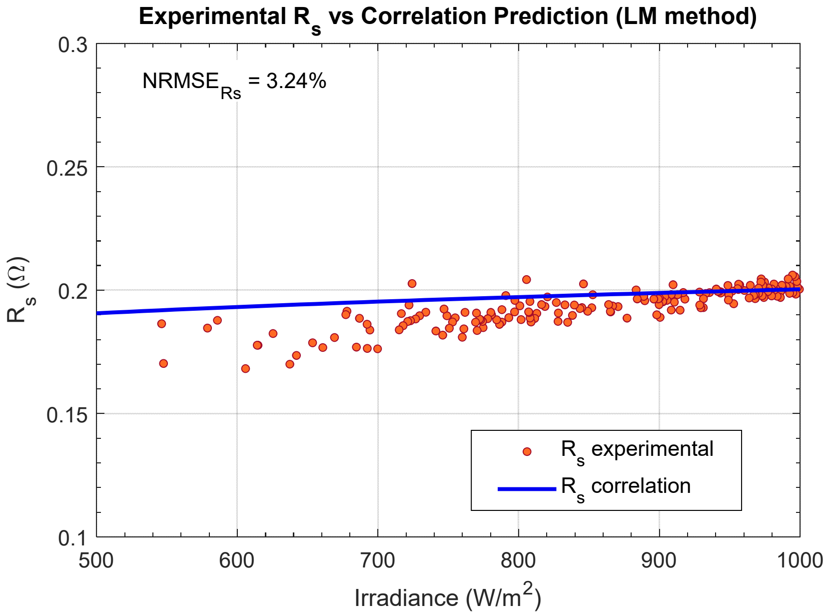

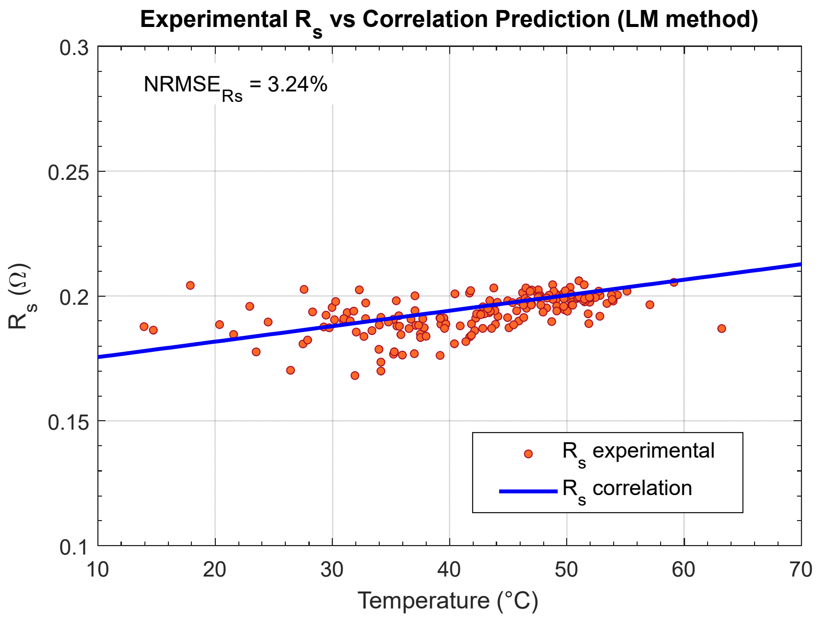

Figure 11.11: R_s tendency with irradiance and temperature (LM algorithm)

$$R_s = \mathbf{0,185} \cdot \frac{T_c}{T_{c,STC}} \cdot \left(1 - (\mathbf{-0,070}) \cdot \log\left(\frac{G}{G_{STC}}\right)\right) \tag{11.7}$$

The orange dots show the R_s values from the LM optimization (i.e. experimental) while the blue line shows the trend of the correlation in (11.7). The goodness of the correlation is confirmed by the *NRMSE* value of 3,24%. This value is typical for the series resistance correlation. The series resistance shows an increase tendency with both irradiance and temperature.

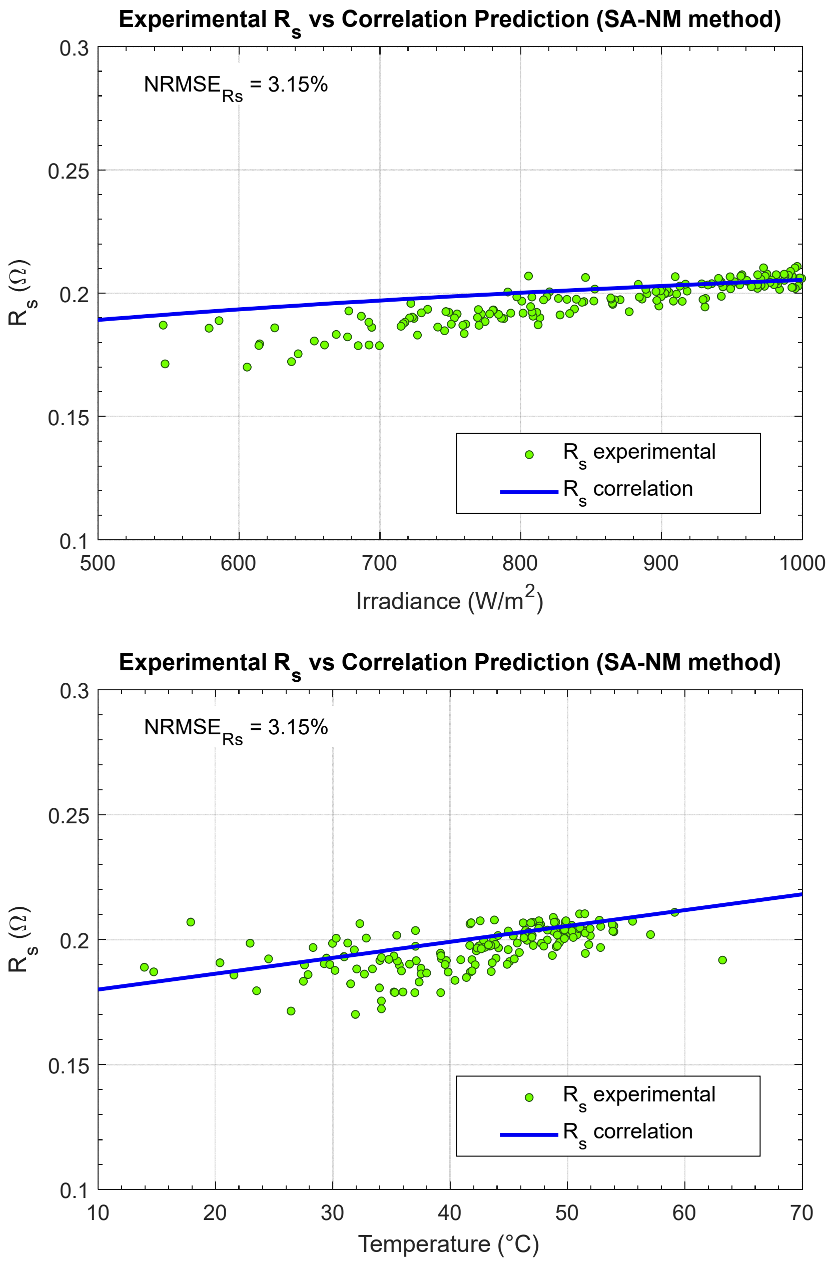

Figure 11.12: R_s tendency with irradiance and temperature (SA-NM method)

$$R_s = \mathbf{0,190} \cdot \frac{T_c}{T_{c,STC}} \cdot \left(1 - (\mathbf{-0,114}) \cdot \log\left(\frac{G}{G_{STC}}\right)\right) \tag{11.8}$$

The green dots show the R_s values from the SA-NM optimization (i.e. experimental) while the blue line represents the trend of the correlation in (11.6). The goodness of the correlation is confirmed by the $NRMSE$ value of 3,15%. However, the correlation on SA-NM data is slightly better than the one on LM data. It is important to highlight that the dimensionless coefficient λ is negative. This is confirmed in the experimental data, where the series resistance increase with irradiance and temperature. Moreover, the dependence is similar in irradiance and temperature. Therefore, two 3D plots (LM and SA-NM) are used to understand the double dependency in irradiance and temperature and they are proposed in Annex D.

Finally, the shunt resistance (R_{sh}) shows variation with irradiance and cell temperature. The correlation equation comes from the equation (8.8)(8.1). The $R_{sh,STC}$ coefficient is optimized by the correlation. Figure 11.13 and Figure 11.14 illustrate the irradiance tendency respectively for LM and SA-NM methods.

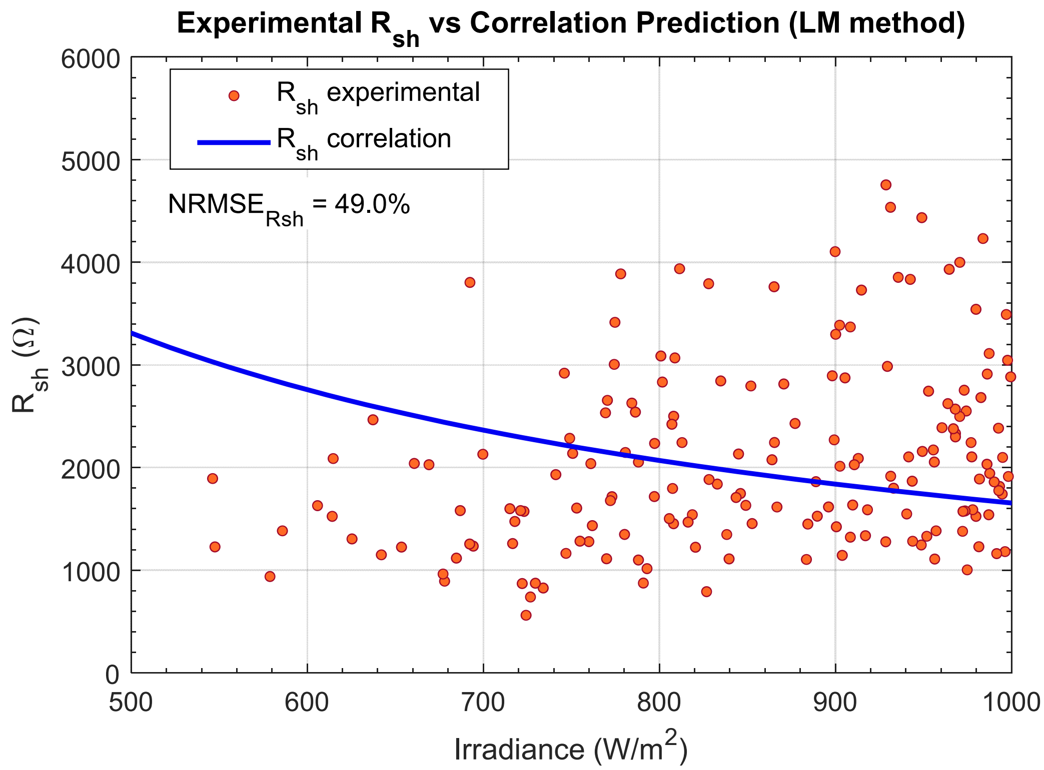

Figure 11.13: R_{sh} tendency with irradiance (LM algorithm)

$$R_{sh} = \mathbf{1655} \cdot \frac{G_{STC}}{G} \tag{11.9}$$

The orange dots indicate the R_{sh} values from the LM optimization (i.e. experimental) while the blue line highlights the trend of the correlation in (11.9). Besides, the plot shows a scattered tendency. This tendency is typical for the shunt resistance because this parameter has little influence in the optimization process if big enough. Therefore, the *NRMSE* value of 49,0% is acceptable.

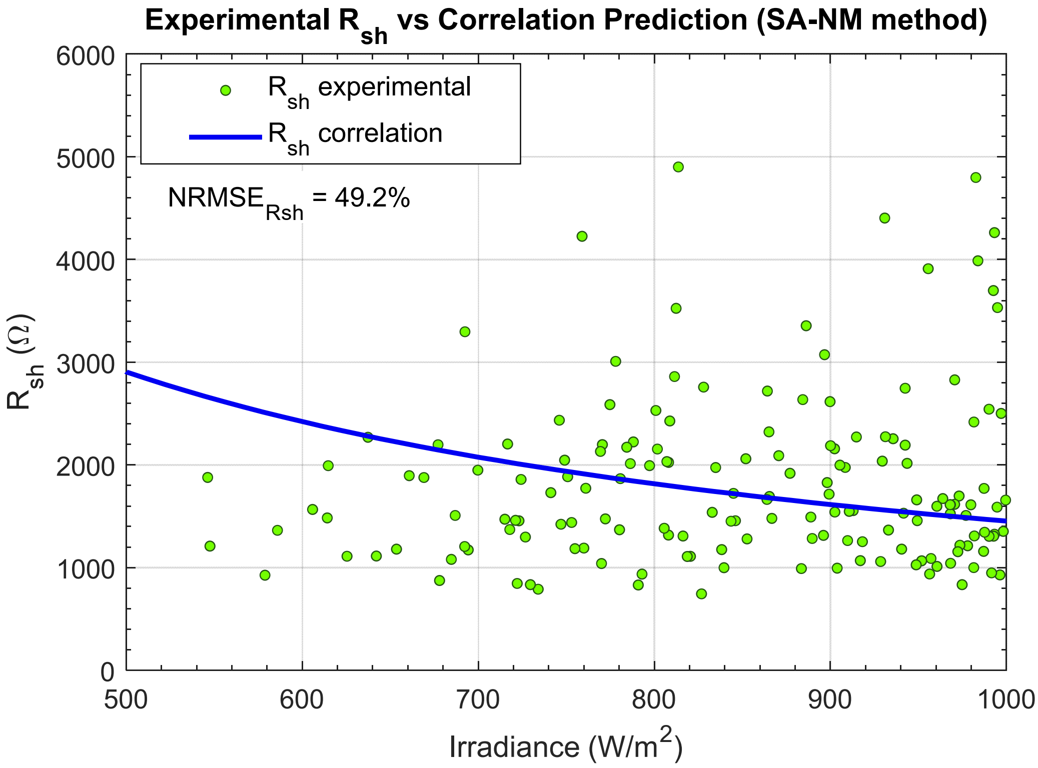

Figure 11.14: R_s tendency with irradiance (SA-NM method)

$$R_{sh} = \mathbf{1453} \cdot \frac{G_{STC}}{G} \tag{11.10}$$

The green dots show represent the R_{sh} values from the SA-NM optimization (i.e. experimental) while the blue line indicates the trend of the correlation in (11.10)(11.6). The correlation shows the *NRMSE* value of 49,2%. However, the correlation on LM data is slightly better than the one on SA-NM data.

The correlation coefficients (i.e. $I_{ph,STC}$, α, $I_{0,STC}$, χ, a, b, c, $R_{s,STC}$, λ, $R_{sh,STC}$) found are reported in Table 11.1.

Correlation coefficients	LM method	SA-NM method
$I_{ph,STC}$ (A)	7,35	7,36
α (%/K)	0,0300	0,0300
$I_{0,STC}$ (A)	$2{,}25 \cdot 10^{-7}$	$2{,}25 \cdot 10^{-7}$
χ (-)	0,61	0,60
a (-)	1,46	1,48
b ($\mathrm{W}^{-1} \cdot \mathrm{m}^2$)	$8{,}47 \cdot 10^{-5}$	$4{,}61 \cdot 10^{-5}$
c (C^{-1})	$3{,}29 \cdot 10^{-4}$	$3{,}36 \cdot 10^{-4}$
$R_{s,STC}$ (Ω)	0,185	0,190
λ_{R_s} (-)	-0,070	-0,114
$R_{sh,STC}$ (Ω)	1655	1453

Table 11.1: Correlation coefficients for the Sanyo HIT module

It is important to say that both extraction procedures lead to similar results and *NRMSE* errors. These errors are reported in Figure 11.15 for each parameter. Although some errors may seem significant, it is necessary to consider that the correlations' mathematical model used has approximations. In particular, the study is conducted on a photovoltaic module made up of 60 cells that can have slightly different behaviors.

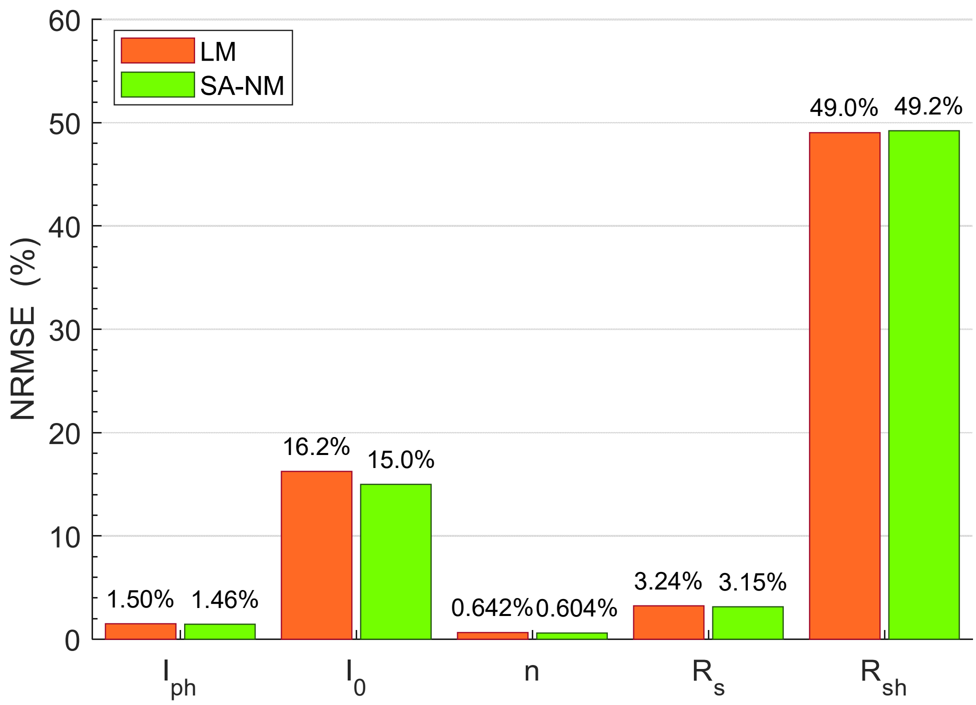

Figure 11.15: *NRMSE* for each parameters correlation

The last analysis on the results of the correlation consists in redrawing the experimental *I-V* curve with the found correlations. Figure 11.16 shows the seven experimental *I-V* curves of Figure 11.1 compared to the respective approximations found with the correlations.

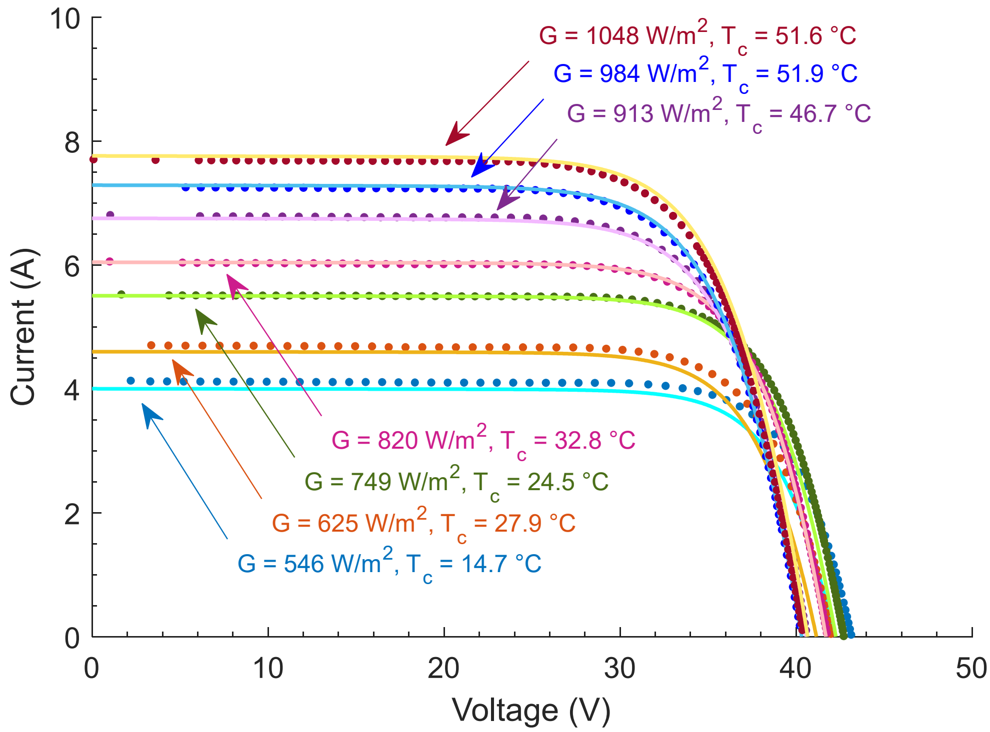

Figure 11.16: *I-V* curves experimentally measured (dots) and trend estimated with the correlation (LM method)

The model trends fit the experimental *I-V* curve with a good approximation for all the levels of irradiance.

11.3. Power validation and Energy computation results

The maximum power experimental data are compared to the maximum power estimated data from the three models (i.e. LM, SA-NM, and Osterwald). This comparison is performed in three ways.

The first analysis is performed on a single day. Figure 11.17 shows the shape of the power during a day. On the one hand, the LM and the SA-NM methods provide a similar estimation. They overestimate the experimental power especially during the central hour. In particular, the LM method presents a *NRMSE* value of 2,3% while the SA-NM method presents a *NRMSE* value of 2,2% for that day. On the other hand, the Osterwald method overestimates even more the experimental data. In this case, the *NRMSE* value is 3%. In summary, the use of the proposed correlation method leads to a reduction of the *NRMSE*, compared to the Osterwald method, evaluable in 27%.

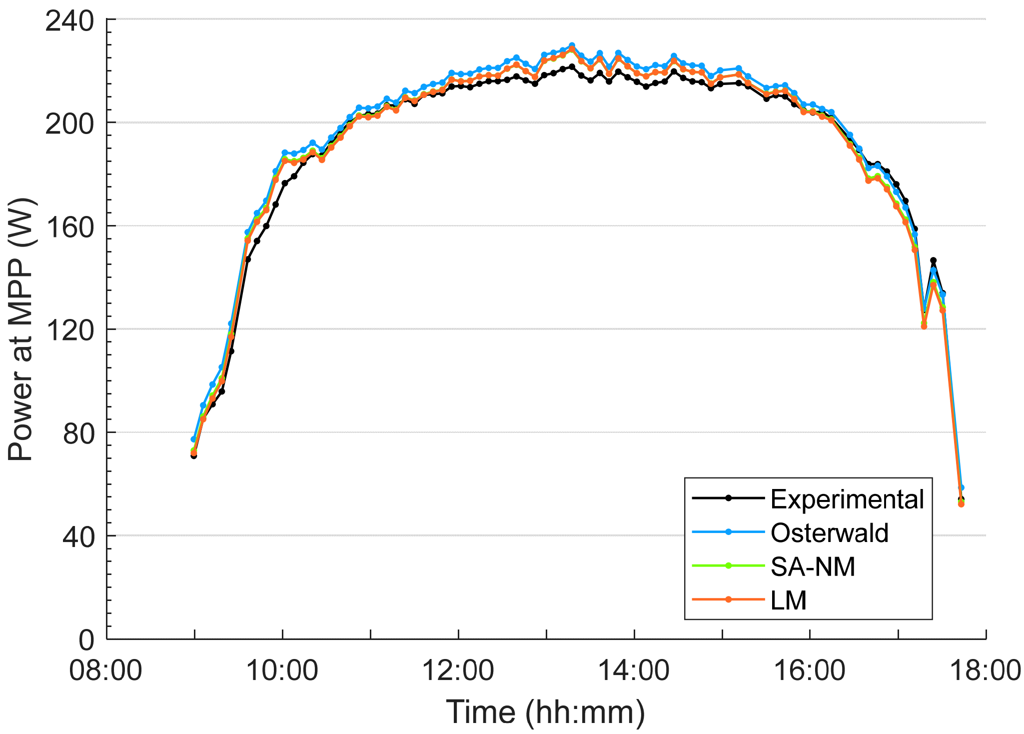

Figure 11.17: Comparison of power estimation for one day.
LM and SA-NM model are overlapped

The second analysis is performed graphically in Figure 11.18. This figure shows how the three models overlap the experimental validation dataset in black. This validation dataset (i.e. 10'360 curves) is extracted from the full dataset (i.e. 14'367 curves) by the application of the mismatch filter with medium tolerance. The Osterwald model presents an overestimation of the power at high irradiance. This behavior agrees with what is widely studied in the literature [38]. The LM and SA-NM models cover better the experimental point at high irradiance, but they also present an overestimation. Besides, the LM and SA-NM estimations show similar results. Moreover, it is important to report that the power is slightly influenced by the module temperature. Therefore, the temperature influence leads to sparse power value for each irradiance.

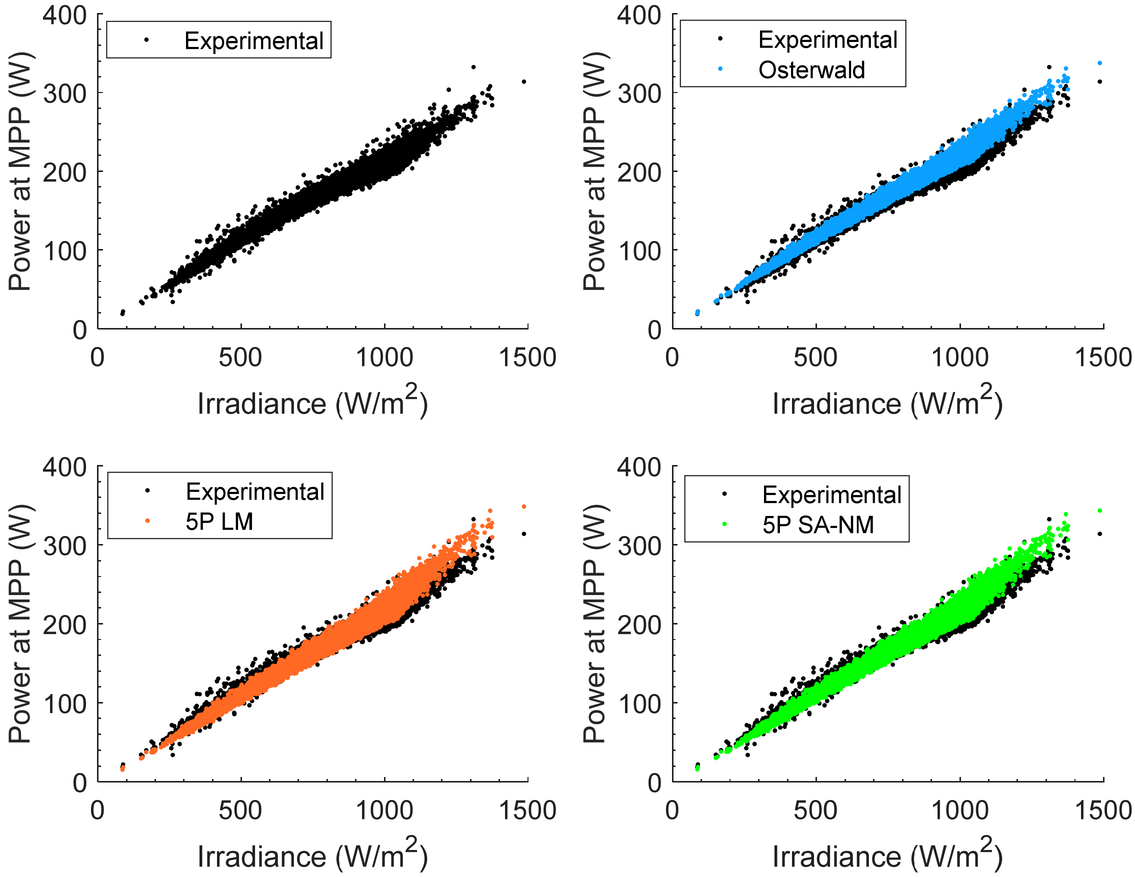

Figure 11.18: Power at different irradiance, experimental value vs the three models (Osterwald in blue, LM in orange, SA-NM in green)

The third analysis consists in the computation of the *NRMSE* between the experimental and estimated power of each model. This analysis is performed on the same validation dataset of the previous analysis. Figure 11.19 shows the *NRMSE* comparison among the three models for all types of days (i.e. global), sunny days, partly cloudy days, and cloudy days (see section 9.2). The SA-NM model is the best in each condition because there is a global error of 5,0%; however, the error increases up to 5,3% on cloudy days and up to 5,1% on partly cloudy days. Besides, the error decreases up to 4,9% on sunny days. The LM model presents a global error of 5,3%, however the error rises up to 5,8% on cloudy days. The Osterwald model shows a global error (5,8%), higher than the ones in the LM and SA-NM models. Besides, the Osterwald model error falls up to 5,4% on cloudy days.

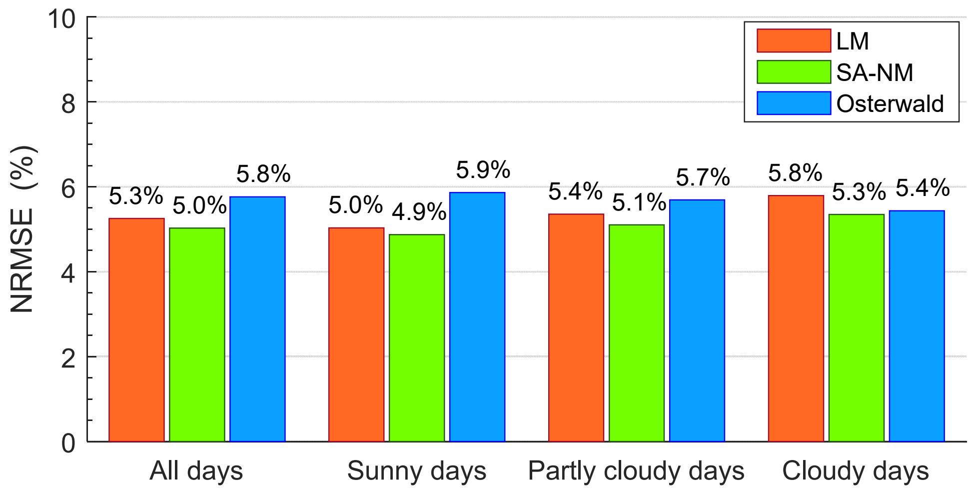

Figure 11.19: *NRMSE* values on estimated power at MPP (division by day type)

Figure 11.20 shows the power *NRMSE* for three different levels of irradiance. In particular, low irradiance indicates $0 \leq G < 400$ W/m², medium irradiance implies 400 W/m² $\leq G < 800$ W/m², and high irradiance means 800 W/m² $\leq G < 1200$ W/m². The LM and SA-NM models works well at high irradiance with a *NRMSE* of 5,0% and 4,8% respectively, while the Osterwald method is the best model at medium and low irradiance with a *NRMSE* of 3,4% and 6,3%. Globally, the LM and SA-NM models perform better results than the Osterwald model. This is due to the fact that the LM and SA-NM models work well at high irradiance conditions where most of the measures are collected.

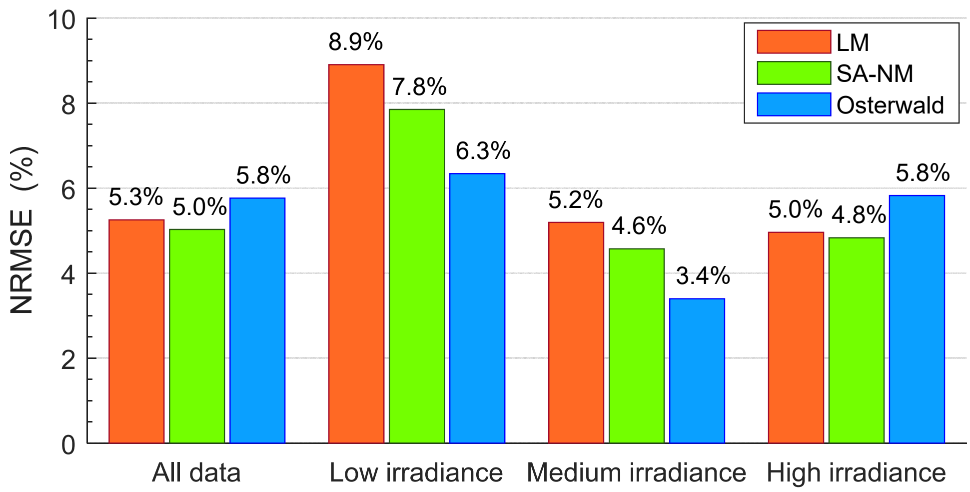

Figure 11.20: *NRMSE* values on estimated power at MPP (division by irradiance)

The last analysis is performed on the error on energy estimation. The global dataset (i.e. 14’367 curves) is used to perform this analysis. Figure 11.21 shows the percentage error on the energy produced during the year. The LM model is the best in terms of energy error in each condition because it has a global error of 3,4%, besides the error decreases up to 3,3% on partly cloudy days and up to 1,4% on cloudy days. Moreover, the error increases up to 3,9% on sunny days.

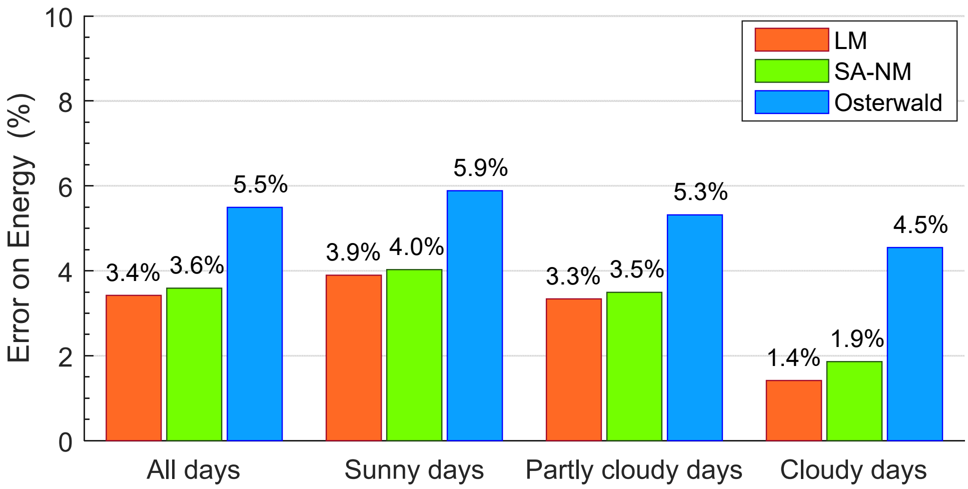

Figure 11.21: Percentage error on estimated energy

Chapter 12

Conclusions

The performance of PhotoVoltaic (PV) generators can be described by an equivalent circuit with a variable number of parameters, which are, generally, assumed constant. However, the knowledge of their dependence with respect to irradiance and cell temperature allows to predict the generated power of photovoltaic arrays in any weather condition. This work is part of a joint activity between Politecnico di Torino and the Universidad de Jaén (Spain): the first part of the thesis has been performed in Politecnico di Torino, while the second activity of the thesis has been developed in Universidad de Jaén.

In the first part of the thesis, an ad hoc Graphical User interface (GUI) is developed in MATLAB ambient to analyze wide experimental datasets of PV generators. In particular, the tool allows to perform four operations: the preprocessing of the dataset; the extraction of the circuit parameters; the identification of equations, aiming to describe the dependence of each parameter with respect to irradiance and cell temperature; and the comparison between experimental energy and the predicted value with several methods. The experimental data may be affected by measurement errors or PV generators may work in mismatch conditions due to shadowing or other issues. Therefore, the preprocessing step removes problematic measurements by applying proper filters. In the parameters extraction step, the parameters are numerically determined starting from the filtered measurements. The GUI allows to identify the circuit parameters using up to two circuit models and three numerical algorithms. The third step of the analysis regards the identification of the dependence of circuit parameters with respect to cell temperature and irradiance. In particular, the most common equations in literature are assumed as the reference and a nonlinear optimization of specific coefficients is performed. Finally, the generated energy during the experimental campaign is compared to the predicted value by several methods. The GUI permits to estimate PV energy using theoretical models and the optimized equations: in fact, starting from the knowledge of the parameters, the current-voltage (I-V) curve can be traced at each time step and the corresponding maximum power is identified.

In the second part of the thesis, the GUI is applied to a high efficiency Heterojunction with Intrinsic Thin layer (HIT) module with rated power of 240 W. For this module, 417 *I-V* curves are selected for the parameters extraction. The remaining data are excluded due to different factors (measurement errors, mismatch conditions, high wind speed). The performance of the photovoltaic module is described by the single diode model, which is an equivalent circuit consisting of five parameters. Then, the extraction procedure is performed using two optimization methods: the Levenberg-Marquardt (LM) and the Simulated Annealing/Nelder-Mead (SA-NM) algorithms. Moreover, two additional filters are applied to the results of the parameters extraction in order to exclude the parameters sets leading to a high error in the Maximum Power Point (MPP). In particular, a set of 357 curves is obtained with the LM algorithm, while the resulting curves of the SA-NM method are 335. The largest error on the MPP with LM dataset is 0,4% while it increases up to 0,5 % with the SA-NM. Starting from these two datasets, the equations describing the dependence of each parameter with respect to irradiance and cell temperature are identified. The correlations show similar results to the analyzed datasets. Regarding the most important parameters, the photogenerated current and the series resistance present, respectively, a Normalized Root Mean Square Error (*NRMSE*) of 1,5% and 3% for both the datasets, while the *NRMSE* of the reverse saturation current ranges between 15% (SA-NM) and 16% (LM). In the last part of the analysis, a comparison between the experimental energy and the predicted value with optimized equations is performed. Moreover, the proposed correlations are compared to the Osterwald Model (OM), which is the simplest and most common theoretical model used in literature to predict PV production. The results show that the LM equations predict PV energy with the lowest error, providing a deviation from experimental data of 3,4%, while the SA-NM and the OM results exhibit, respectively, an error of 3,6% and 5,5%.

Annex A

Technical datasheet of measurement equipment

A.1 Technical datasheet Agilent 34411A Multimeters

Measurement Characteristics

DC Voltage

Measurement Method:
Continuously integrating multi-slope IV A/D converter

Linearity: (10 V range) 0.0002% of reading + 0.0001% of range

Input Resistance:
0.1 V, 1 V, 10 V Ranges: 10 MΩ or > 10 GΩ (Selectable)
100 V, 1000 V Ranges: 10 MΩ ± 1% (Fixed)

Input Bias Current: < 50 pA at 25 °C

Input Protection: 1000 V

DC CMRR: 140 dB[1]

True RMS AC Voltage

Measurement Method:
AC-coupled True RMS measurement. Digital sampling with anti-alias filter.

Crest Factor:
No additional error for crest factors < 10. Limited by peak input and 300 kHz bandwidth.

Peak Input:
300% of range or 1100 V

Overload Ranging:
Will select higher range if peak input overload is detected during auto range. Overload is reported in manual ranging.

AC CMR: 70 dB[2]

Maximum Input: 400 Vdc, 1100 Vpk

Input Impedance:
1 MΩ ± 2% in parallel with < 150 pF

Input Protection: 750 V_{rms} all ranges

Resistance

Measurement Method:
Selectable 2-wire or 4-wire. Current source referenced to LO input.

Offset Compensation:
Selectable on the 100 Ω, 1 kΩ, and 10 kΩ ranges

Max. Lead Resistance (4-wire):
10% of range per lead for 100 Ω, 1 kΩ. 1 kΩ per lead on all other ranges

Input Protection:
1000 V on all ranges

DC Current

Current Shunt:
200 Ω for 100 µA, 1 mA
2 Ω for 10 mA, 100 mA
0.1 Ω for 1 A, 3 A

Input Protection: 3 A, 250 V fuse

True RMS AC Current

Measurement Method:
AC-coupled True RMS measurement. Directly coupled to the fuse and shunt. Digital sampling with anti-alias filter.

Current Shunt:
200 Ω for 100 µA, 1 mA
2 Ω for 10 mA, 100 mA
0.1 Ω for 1 A, 3 A

Maximum Input:
The peak value of the DC + AC current must be < 300% of range. The RMS current must be < 3 A including the DC current content.

Input Protection: 3 A, 250 V fuse

Frequency and Period

Measurement Method:
Reciprocal-counting technique. AC-coupled input using the AC voltage measurement function.

Input Impedance:
1 MΩ ± 2% in parallel with < 150 pF

Input Protection: 750 V_{rms} all ranges

Capacitance

Measurement Method:
Current input with measurement of resulting ramp.

Connection Type: 2-wire

Temperature

Thermistor:
2.2 kΩ, 5 kΩ, and 10 kΩ

RTD: α = 0.00385
R_0 from 49 Ω to 2.1 kΩ

Continuity/Diode Test

Response Time:
300 samples/sec with audible tone

Continuity Threshold: Fixed at 10 Ω

Operating Characteristics Maximum readings/second

	Digits		
Function[3]	4.5	5.5	6.5
DCV	50 k[4]	10 k	1 k
2-wire Ω	50 k[4]	10 k	1 k
DCI	50 k[4]	10 k	1 k
Frequency	500	90	10
Period	500	90	10
Filter setting	fast	med	slow
ACV	500	150	50
ACI	500	150	50

Additional 34411A Specifications

Resolution: See table on page 4

Overall Bandwidth, DCV & DCI:
15 kHz typical @ 20 µs aperture (-3 dB)

Triggering: Pre/Post, Int/Ext, Pos/Neg

Timebase Resolution: 19.9524 µs 0.01% accuracy

Trigger Jitter:
2 µs (p-p), 20 µs (p-p) when pre-triggered

Spurious-Free Dynamic Range & Signal to Noise Distortion Ratio

Function DCV Range	Spur-Free	SNDR
1 V	-75 dB	60 dB
10 V[1]	-70 dB	60 dB
100 V	-75 dB	60 dB

[1]10 V range: 2 V (p-p) < signal < 16 V (p-p)

Triggering and Memory

Reading Hold Sensitivity: 1% of reading

Samples per Trigger:
1 to 50,000 (34410A)
1 to 1,000,000(34411A)

Trigger Delay: 0 to 3600 s (20 µs step size)

External Trigger:
Programmable edge, Low-power TTL compatible
Delay: < 1 µs **Max rate:** 5,000/s
Jitter: < 1 µs **Min Pulsewidth:** 1 µs

Voltmeter Complete: 3 V Logic output, 2 µs pulse with programmable edge

Nonvolatile Memory: 50,000 readings

Volatile Memory:
50,000 readings (34410A)
1,000,000 readings (34411A)

Sample Timer:
Range: 0 to 3600 s (20 µs step sizes)
Jitter: < 100 ns

General Specifications

Power Supply:
100 V/120 V/220 V/240 V ± 10%

Power Line Frequency:
45 Hz to 66 Hz and 360 Hz to 440 Hz, Automatically sensed at power-on

Power Consumption: 25 VA peak (16 W average)

Operating Environment: Full accuracy for 0 °C to 55 °C, 80% R.H. at 40 °C non-condensing

Storage Temperature: -40 °C to 70 °C

Weight: 3.72 kg (8.2 lbs)

Safety: IEC 61010-1, EN 61010-1, UL 61010-1, CAN/CSA-C22.2 No. 61010-1, Refer to Declarations of Conformity for current revisions. Measurement CAT II 300 V, CAT I 1000 V. Pollution Degree 2

EMC: IEC 61326, EN 61326, CISPR 11, ICES-001, AS/NZS 2064.1, Refer to Declaration of Conformity for current revisions.

Vibration & Shock: MIL-T-28800E, Type III, Class 5 (Sine Only)

LXI Compliance: LXI Class C, ver. 1.0

Warranty: 3 year standard

1. For 1 kΩ unbalanced in LO lead, ± 500 V peak maximum
2. For 1 kΩ unbalanced in LO lead and < 60 Hz, ± 500 V peak maximum
3. Maximum rate for DCV, DCI, and resistance functions (using zero settling delay, autozero off, manual range)
4. 34411A only

A-to-D Converter Noise Performance

Integration Time (NPLC)	Resolution (ppm of range)[1]	Normal Mode Rejection (dB)[2]	Readings/Second[4]
0.001[5]	30	0	50,000
0.002[5]	15	0	25,000
0.006	6	0	10,000
0.02	3	0	3,000
0.06	1.5	0	1,000
0.2	0.7	0	300
1	0.3	55	60 (50)
2	0.2	110[3]	30 (25)
10	0.1	110[3]	6 (5)
100	0.03	110[3]	0.6 (0.5)

1. Resolution is defined as the typical DCV 10 V range RMS noise. Auto-zero on for NPLC ≥ 1. See manual for additional noise characteristics.
2. Normal mode rejection for power line frequency ± 0.1%.
3. For power-line frequency ± 1% 75 dB and for ± 3% 55 dB.
4. Maximum rate with auto-zero off for 60 Hz and (50 Hz) operation.
5. Only available for the 34411A.

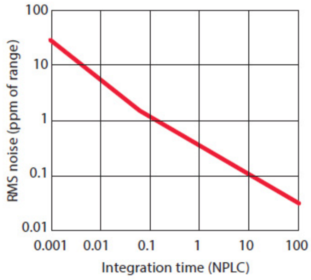

System Reading and Throughput Rates

DMM memory to PC (Maximum reading rate out of memory[6]
Drawing – Path B

Reading Format	GPIB Readings/s	USB 2.0 Readings/s	LAN (VXI-11) Readings/s	LAN (Sockets) Readings/s
ASCII	4,000	8,500	7,000	8,500
32-bit Binary	89,000	265,000	110,000	270,000
64-bit Binary	47,000	154,000	60,000	160,000

System Reading Architecture

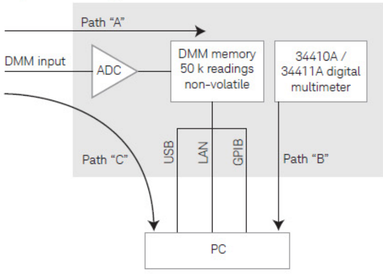

Direct I/O Measurements (Single reading – measure and I/O time)[6]

Drawing - Path C

Function	Resolution (NPLC)	GPIB ms	USB 2.0 ms	LAN (VXI-11) ms	LAN (sockets) ms	Maximum Reading Rate into Memory or to Direct I/O (Readings/s) Drawing – Path A or C
DCV/2-wire Resistance	0.006 (0.001)	2.6	2.9	4.6	3.2	10,000 (50,000)
ACV/ Frequency	Fast Filter 1 ms gate	10.0	10.0	10.0	10.0	500

6. 1/2 scale input signal, immediate trigger, trigger delay 0, auto-zero off, auto-range off, no math, null off, 60 Hz line frequency. Specifications are for 34410A or (34411A). See manual for performance on other functions.

System Performance

	Function Change (ms)[7]	Range Change (ms)[8] LAN/GPIB	Auto-range (ms)[9]	Maximum External Trigger Rate	Maximum Internal Trigger Rate[10]
DCV/2-wire Resistance	22	3.9/2.6	7.5	5,000/s	10,000/s (50,000/s)
ACV/ Frequency	37	6.5/6.4	19	500/s	500/s

7. Time to change from 2-wire Resistance to this specified function, or DCV to 2-wire Resistance using the SCPI "FUNC" command.
8. Time to change from one range to the next higher range, ≤ 10 V, ≤ 10 MΩ.
9. Time to automatically change one range and be ready for the new measurement, ≤ 10 V, ≤ 10 MΩ.
10. Specifications are for 34410A or (34411A).

Accuracy Specifications ± (% of reading + % of range)[1]

Function	Range[3]	Frequency, Test Current or Burden Voltage	24 Hour[2] Tcal ± 1 °C	90 Day Tcal ± 5 °C	1 Year Tcal ± 5 °C	Temperature Coefficient/°C 0 °C to (Tcal -5 °C) (Tcal +5 °C) to 55 °C
DC Voltage	100.0000 mV		0.0030 + 0.0030	0.0040 + 0.0035	0.0050 + 0.0035	0.0005 + 0.0005
	1.000000 V		0.0020 + 0.0006	0.0030 + 0.0007	0.0035 + 0.0007	0.0005 + 0.0001
	10.00000 V		**0.0015 + 0.0004**	**0.0020 + 0.0005**	**0.0030 + 0.0005**	**0.0005 + 0.0001**
	100.0000 V		0.0020 + 0.0006	0.0035 + 0.0006	0.0040 + 0.0006	0.0005 + 0.0001
	1000.000 V[4]		0.0020 + 0.0006	0.0035 + 0.0006	0.0040 + 0.0006	0.0005 + 0.0001
True RMS AC Voltage[5]	100.0000 mV to 750.000 V	3 Hz – 5 Hz	0.50 + 0.02	0.50 + 0.03	0.50 + 0.03	0.010 + 0.003
		5 Hz – 10 Hz	0.10 + 0.02	0.10 + 0.03	0.10 + 0.03	0.008 + 0.003
		10 Hz – 20 kHz	**0.02 + 0.02**	**0.05 + 0.03**	**0.06 + 0.03**	**0.005 + 0.003**
		20 kHz – 50 kHz	0.05 + 0.04	0.09 + 0.05	0.10 + 0.05	0.010 + 0.005
		50 kHz – 100 kHz	0.20 + 0.08	0.30 + 0.08	0.40 + 0.08	0.020 + 0.008
		100 kHz – 300 kHz	1.00 + 0.50	1.20 + 0.50	1.20 + 0.50	0.120 + 0.020
Resistance[6]	100.0000 Ω	1 mA	0.0030 + 0.0030	0.008 + 0.004	0.010 + 0.004	0.0006 + 0.0005
	1.000000 kΩ	1 mA	0.0020 + 0.0005	0.007 + 0.001	0.010 + 0.001	0.0006 + 0.0001
	10.00000 kΩ	**100 µA**	**0.0020 + 0.0005**	**0.007 + 0.001**	**0.010 + 0.001**	**0.0006 + 0.0001**
	100.0000 kΩ	10 µA	0.0020 + 0.0005	0.007 + 0.001	0.010 + 0.001	0.0006 + 0.0001
	1.000000 MΩ	5 µA	0.0020 + 0.0010	0.010 + 0.001	0.012 + 0.001	0.0010 + 0.0002
	10.00000 MΩ	500 nA	0.0100 + 0.0010	0.030 + 0.001	0.040 + 0.001	0.0030 + 0.0004
	100.0000 MΩ	500 nA ‖ 10 MΩ	0.200 + 0.001	0.600 + 0.001	0.800 + 0.001	0.1000 + 0.0001
	1.000000 GΩ	500 nA ‖ 10 MΩ	2.000 + 0.001	6.000 + 0.001	8.000 + 0.001	1.0000 + 0.0001
DC Current	100.0000 µA	< 0.03V	0.010 + 0.020	0.040 + 0.025	0.050 + 0.025	0.0020 + 0.0030
	1.000000 mA	**< 0.3 V**	**0.007 + 0.006**	**0.030 + 0.006**	**0.050 + 0.006**	**0.0020 + 0.0005**
	10.00000 mA	< 0.03V	0.007 + 0.020	0.030 + 0.020	0.050 + 0.020	0.0020 + 0.0020
	100.0000 mA	< 0.3 V	0.010 + 0.004	0.030 + 0.005	0.050 + 0.005	0.0020 + 0.0005
	1.000000 A	< 0.8 V	0.050 + 0.006	0.080 + 0.010	0.100 + 0.010	0.0050 + 0.0010
	3.000000 A	< 2.0 V	0.100 + 0.020	0.120 + 0.020	0.150 + 0.020	0.0050 + 0.0020
True RMS AC Current[7]	100.0000 µA to 3.00000 A	**3 Hz – 5 kHz**	**0.10 + 0.04**	**0.10 + 0.04**	**0.10 + 0.04**	**0.015 + 0.006**
		5 kHz – 10 kHz	0.20 + 0.04	0.20 + 0.04	0.20 + 0.04	0.030 + 0.006
Frequency or Period	100 mV to 750 V	3 Hz – 5 Hz	0.070 + 0.000	0.070 + 0.000	0.070 + 0.000	0.005 + 0.000
		5 Hz – 10 Hz	0.040 + 0.000	0.040 + 0.000	0.040 + 0.000	0.005 + 0.000
		10 Hz – 40 Hz	0.020 + 0.000	0.020 + 0.000	0.020 + 0.000	0.001 + 0.000
		40 Hz – 300 kHz	**0.005 + 0.000**	**0.006 + 0.000**	**0.007 + 0.000**	**0.001 + 0.000**
Capacitance[8]	1.0000 nF	500 nA	0.50 + 0.50	0.50 + 0.50	0.50 + 0.50	0.05 + 0.05
	10.000 nF	1 µA	0.40 + 0.10	0.40 + 0.10	0.40 + 0.10	0.05 + 0.01
	100.00 nF	10 µA	0.40 + 0.10	0.40 + 0.10	0.40 + 0.10	0.01 + 0.01
	1.0000 µF	10 µA	0.40 + 0.10	0.40 + 0.10	0.40 + 0.10	0.01 + 0.01
	10.000 µF	100 µA	0.40 + 0.10	0.40 + 0.10	0.40 + 0.10	0.01 + 0.01
Temperature[9]						
RTD	-200 °C to 600 °C		0.06 °C	0.06 °C	0.06 °C	0.003 °C
Thermistor	-80 °C to 150 °C		0.08 °C	0.08 °C	0.08 °C	0.002 °C
Continuity	1000.0 Ω	1 mA	0.002 + 0.010	0.008 + 0.020	0.010 + 0.020	0.0010 + 0.0020
Diode Test[10]	1.0000 V	1 mA	0.002 + 0.010	0.008 + 0.020	0.010 + 0.020	0.0010 + 0.0020

1. Specifications are for 90 minute warm-up and 100 PLC.
2. Relative to calibration standards.
3. 20% overrange on all ranges, except DCV 1000 V, ACV 750 V, DCI and ACI 3 A ranges.
4. For each additional volt over ± 500 V add 0.02 mV of error.
5. Specifications are for sinewave input > 0.3% of range and > 1 mVrms. Add 30 µV error for frequencies below 1 kHz. 750 VAC range limited to 8 x 107 Volts-Hz. For each additional volt over 300 Vrms add 0.7 mVrms of error.
6. Specifications are for 4-wire resistance measurements, or 2-wire using Math Null. Without Math Null, add 0.2 Ω additional error in 2-wire resistance measurements.
7. Specifications are for sinewave input > 1% of range and > 10 µArms. Frequencies > 5 kHz are typical for all ranges. For the 3 A range (all frequencies) add 0.05% of reading + 0.02% of range to listed specifications.
8. Specifications are for 1-hour warm-up using Math Null. Additional errors may occur for non-film capacitors.
9. For total measurement accuracy, add temperature probe error.
10. Accuracy specifications are for the voltage measured at the input terminals only. 1 mA test current is typical. Variation in the current source will create some variation in the voltage drop across a diode junction.

A.2 Technical datasheet Agilent 34970A Datalogger

34970A/34972A accuracy specifications ±(% of reading + % of range)[1]

Includes measurement error, switching error, and transducer conversion error

	Range [3]	Frequency, etc.	24 hour [2] 23 ±1°C	90 Day 23 ±5°C	1 Year 23 ±5°C	Temperature coefficient 0 – 18°C, 28 - 55°C
DC voltage						
	100.0000 mV		0.0030 + 0.0035	0.0040 + 0.0040	0.0050 + 0.0040	0.0005 + 0.0005
	1.000000 V		0.0020 + 0.0006	0.0030 + 0.0007	0.0040 + 0.0007	0.0005 + 0.0001
	10.00000 V		0.0015 + 0.0004	0.0020 + 0.0005	0.0035 + 0.0005	0.0005 + 0.0001
	100.0000 V		0.0020 + 0.0006	0.0035 + 0.0006	0.0045 + 0.0006	0.0005 + 0.0001
	300.000 V		0.0020 + 0.0020	0.0035 + 0.0030	0.0045 + 0.0030	0.0005 + 0.0003
True RMS AC voltage [4]						
	All ranges from 100.0000 mV to 100.0000 V	3 Hz–5 Hz	1.00 + 0.03	1.00 + 0.04	1.00 + 0.04	0.100 + 0.004
		5 Hz–10 Hz	0.35 + 0.03	0.35 + 0.04	0.35 + 0.04	0.035 + 0.004
		10 Hz–20 kHz	0.04 + 0.03	0.05 + 0.04	0.06 + 0.04	0.005 + 0.004
		20 kHz–50 kHz	0.10 + 0.05	0.11 + 0.05	0.12 + 0.05	0.011 + 0.005
		50 kHz–100 kHz	0.55 + 0.08	0.60 + 0.08	0.60 + 0.08	0.060 + 0.008
		100 kHz–300 kHz [5]	4.00 + 0.50	4.00 + 0.50	4.00 + 0.50	0.20 + 0.02
	300.0000 V	3 Hz–5 Hz	1.00 + 0.05	1.00 + 0.08	1.00 + 0.08	0.100 + 0.008
		5 Hz–10 Hz	0.35 + 0.05	0.35 + 0.08	0.35 + 0.08	0.035 + 0.008
		10 Hz–20 kHz	0.04 + 0.05	0.05 + 0.08	0.06 + 0.08	0.005 + 0.008
		20 kHz–50 kHz	0.10 + 0.10	0.11 + 0.12	0.12 + 0.12	0.011 + 0.012
		50 kHz–100 kHz	0.55 + 0.20	0.60 + 0.20	0.60 + 0.20	0.060 + 0.020
		100 kHz–300 kHz [5]	4.00 + 1.25	4.00 + 1.25	4.00 + 1.25	0.20 + 0.05
Resistance [6]						
	100.0000 Ω	1 mA current source	0.0030 + 0.0035	0.008 + 0.004	0.010 + 0.004	0.0006 + 0.0005
	1.000000 kΩ	1 mA	0.0020 + 0.0006	0.008 + 0.001	0.010 + 0.001	0.0006 + 0.0001
	10.00000 kΩ	100 µA	0.0020 + 0.0005	0.008 + 0.001	0.010 + 0.001	0.0006 + 0.0001
	100.0000 kΩ	10 µA	0.0020 + 0.0005	0.008 + 0.001	0.010 + 0.001	0.0006 + 0.0001
	1.000000 MΩ	5.0 µA	0.002 + 0.001	0.008 + 0.001	0.010 + 0.001	0.0010 + 0.0002
	10.00000 MΩ	500 nA	0.015 + 0.001	0.020 + 0.001	0.040 + 0.001	0.0030 + 0.0004
	100.0000 MΩ	500 nA || 10 MΩ	0.300 + 0.010	0.800 + 0.010	0.800 + 0.010	0.1500 + 0.0002
Frequency and period [7]						
	100 mV to 300V	3 Hz–5 Hz	0.10	0.10	0.10	0.005
		5 Hz–10 Hz	0.05	0.05	0.05	0.005
		10 Hz–40 Hz	0.03	0.03	0.03	0.001
		40 Hz–300 kHz	0.006	0.01	0.01	0.001
DC current (34901A only)						
	10.00000 mA	<0.1 V burden	0.005 + 0.010	0.030 + 0.020	0.050 + 0.020	0.002+ 0.0020
	100.0000 mA	<0.6 V	0.010 + 0.004	0.030 + 0.005	0.050 + 0.005	0.002 + 0.0005
	1.000000 A	<2 V	0.050 + 0.006	0.080 + 0.010	0.100 + 0.010	0.005 + 0.0010
True RMS AC current (34901A only)						
	10.00000 mA and [4] 1.000000 A	3 Hz–5 Hz	1.00 + 0.04	1.00 + 0.04	1.00 + 0.04	0.100 + 0.006
		5 Hz–10 Hz	0.30 + 0.04	0.30 + 0.04	0.30 + 0.04	0.035 + 0.006
		10 Hz–5 kHz	0.10 + 0.04	0.10 + 0.04	0.10 + 0.04	0.015 + 0.006
	100.0000 mA [8]	3 Hz–5 Hz	1.00 + 0.5	1.00 + 0.5	1.00 + 0.5	0.100 + 0.06
		5 Hz–10 Hz	0.30 + 0.5	0.30 + 0.5	0.30 + 0.5	0.035 + 0.06
		10 Hz–5 kHz	0.10 + 0.5	0.10 + 0.5	0.10 + 0.5	0.015 + 0.06
Temperature	**Type**	**1-year accuracy [9]**		**Extended range 1-year accuracy [9]**		**Temp coefficient/°C**
Thermocouple [10]	B	1100 to 1820°C	1.2°C	400 to 1100°C	1.8°C	0.03°C
	E	–150 to 1000°C	1.0°C	-200 to -150°C	1.5°C	
	J	–150 to 1200°C	1.0°C	-210 to -150°C	1.2°C	
	K	–100 to 1200°C	1.0°C	-200 to -100°C	1.5°C	
	N	–100 to 1300°C	1.0°C	-200 to -100°C	1.5°C	
	R	300 to 1760°C	1.2°C	-50 to 300°C	1.8°C	
	S	400 to 1760°C	1.2°C	-50 to 400°C	1.8°C	
	T	–100 to 400°C	1.0°C	-200 to -100°C	1.5°C	
RTD	R0 from 49 Ω to 2.1 kΩ	–200 to 600°C	0.06°C			0.003°C
Thermistor	2.2 k, 5 k, 10 k	–80 to 150°C	0.08°C			0.002°C

[1] Specifications are for 1 hr warm-up and 6½ digits, Slow ac filter
[2] Relative to calibration standards
[3] 20% over range on all ranges except 300 Vdc and ac ranges and 1 Adc and ac current ranges
[4] For sinewave input > 5% of range. For inputs from 1% to 5% of range and < 50 kHz, add 0.1% of range additional error
[5] Typically 30% of reading error at 1 MHz, limited to 1 x 108 V Hz
[6] Specifications are for 4- wire ohms function or 2-wire ohms using scaling to remove the offset. Without scaling, add 4 Ω additional error in 2-wire Ohms function
[7] Input > 100 mV. For 10 mV to 100 mV inputs multiply % of reading error x 10
[8] Specified only for inputs >10 mA
[9] For total measurement accuracy, add temperature probe error
[10] Thermocouple specifications not guaranteed when 34907A module is present. For < 1°C accuracy, a precision external reference is required.

Find us at www.keysight.com Page 16

Measurement characteristics[7]

DC voltage

Measurement Method	Continuously Integrating Multi-slope III A-D converter
A/D linearity	0.0002% of reading + 0.0001 % of range
Input resistance	
100 mV, 1 V, 10 V ranges	Selectable 10 MΩ or > 10,000 MΩ
100 V, 300 V ranges	10 MΩ ±1%
Input bias current	< 30 pA at 25°C
Input protection	300 V all ranges

True RMS AC voltage

Measurement method	AC coupled True RMS – measures the AC component of the input with up to 300 Vdc of bias on any range	
Crest factor	Maximum of 5:1 at Full Scale	
Additional crest factor errors (non-sinewave)	Crest Factor 1-2	0.05 % of reading
	Crest Factor 2-3	0.15 % of reading
	Crest Factor 3-4	0.30 % of reading
	Crest Factor 4-5	0.40 % of reading
Input impedance	1 MΩ ±2% in parallel with 150 pF	
Input protection	300 Vrms all ranges	

Resistance

Measurement method	Selectable 4-wire or 2-wire Ohms Current source referenced to LO input
Offset compensation	Selectable on 100 Ω, 1 kΩ, 10 kΩ ranges
Maximum lead resistance	10% of range per lead for 100 Ω and 1 kΩ ranges. 1 kΩ on all other ranges
Input protection	300 V on all ranges

Frequency and period

Measurement method	Reciprocal counting technique
Voltage ranges	Same as AC Voltage function
Gate time	1s, 100 ms, or 10 ms
Measurement timeout	Selectable 3 Hz, 20 Hz, 200 Hz LF limit

DC current

Shunt resistance	5Ω for 10 mA, 100 mA; 0.1 Ω for 1 A
Input protection	1 A 250 V fuse on 34901A module

True RMS AC current

Measurement method	Direct coupled to the fuse and shunt. AC coupled True RMS measurement (measures the ac component only)
Shunt resistance	5 Ω for 10 mA; 0.1 Ω for 100 mA, 1 A
Input protection	1 A 250 V fuse on 34901A module

Thermocouple

Conversion	ITS-90 software compensation
Reference junction type	Internal, Fixed, or External
Open thermocouple check	Selectable per channel. Open > 5 kΩ

Thermistor	44004, 44007, 44006 series
RTD	α = 0.00385 (DIN) and α = 0.00391

Measurement noise rejection 60 (50) Hz [1]

dc CMRR	140 dB
ac CMRR	70 dB
Integration time	**Normal mode rejection**[2]
200 plc/3.33s (4s)	110 dB [3]
100 plc/1.67s (2s)	105 dB [3]
20 plc/333 ms (400 ms)	100 dB [3]
10 plc/167 ms (200 ms)	95 dB [3]
2 plc/33.3 ms (40 ms)	90 dB
1 plc/16.7 ms (20 ms)	60 dB
< 1 plc	0 dB

Operating characteristics [4]

Single channel measurement rates [5]

Function	Resolution [8]	34970A/34972A readings/sec
dcV, 2-wire resistance	6½ digits (10 plc)	6 (5)
	5½ digits (1 plc)	54 (47)
	4½ digits (0.02 plc)	500
Thermocouple	0.1 °C (10 plc)	6 (5)
	0.1 °C (1 plc)	52 (47)
	(0.02 plc)	280
RTD, thermistor	0.01 °C (10 plc)	6 (5)
	0.1 °C (1 plc)	49 (47)
	1 °C (0.02 plc)	200
acV	6½ Slow (3 Hz)	0.14
	6½ Med (20 Hz)	1
	6½ Fast (200 Hz)	8
	6½ [6]	100
Frequency, period	6½ digits (1 s gate)	1
	5½ digits (100 ms)	9
	4½ digits (10 ms)	70

[1] For 1 KΩ unbalance in LO lead
[2] For power line frequency ±0.1%
[3] For power line frequency ±1% use 80 dB or ±3% use 60 dB
[4] Reading speeds for 60 Hz and (50 Hz) operation
[5] For fixed function and range, readings to memory, scaling and alarms off, AZERO OFF, USB datalogging OFF
[6] Maximum limit with de fault settling delays defeated
[7] Isolation voltage (ch-ch, ch-earth) 300 Vdc, ac rms
[8] 6½ digits = 22 bits, 5½ digits = 18 bits, 4½ digits = 15 bits

Find us at www.keysight.com Page 17

A.3 Technical datasheet Agilent 34901A 20-Channel General Purpose Multiplexer

Multiplexer selection guide

Choose between the broad functionality of the 34901A, the high speed scanning of the 34902A, or the single-ended density of the 34908A. These three modules are the only way to connect to the 34970A/34972A internal DMM. They can be used to scan with external instruments as well.

All multiplexer modules employ break-before-make scanning, ensuring only one closed channel (or channel pair) at a time. Multiple channel closures are allowed on the 34901A and 34902A modules when not configured for scanning.

The 34908A does not allow multiple channel closures at any time.

	34901A	34902A	34908A
Number of channels	20 + 2	16	40
Max scan speed	60 ch/s	250 ch/s	60 ch/s
Number of contacts	2 or 4	2 or 4	1
Temperature			
Thermocouple	●	●	●
2-wire RTD	●	●	●
4-wire RTD	●	●	
Thermistor	●	●	●
dc Volts	●	●	●
ac Volts	●	●	●
2-wire Ohms	●	●	●
4-wire Ohms	●	●	
Frequency	●	●	●
Period	●	●	●
dc current	●		
ac current	●		

34901A

20-Channel General Purpose Multiplexer

- 60 ch/s scanning
- Two- and four-wire scanning
- Built-in thermocouple reference junction
- 300 V switching

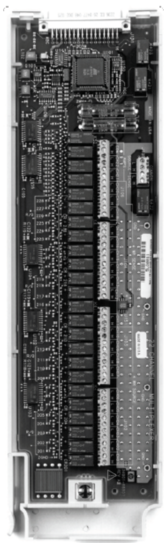

The Keysight 34901A is the most versatile multiplexer for general purpose scanning. It combines dense, multifunction switching with 60-channel/second scan rates to address a broad spectrum of data acquisition applications.

Two- and four-wire channels can be mixed on the same module. Two additional fused inputs (22 channels total) route up to 1 A of current to the internal DMM, allowing ac and dc current measurements without the need for external shunt resistors.

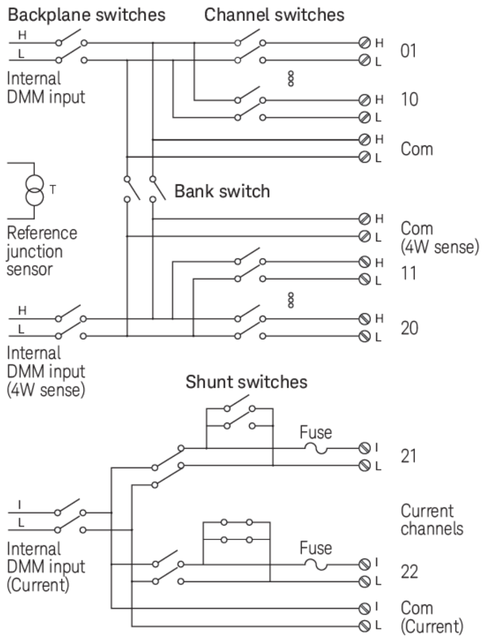

A.4 Technical datasheet Agilent 34907A Digital Multifunction Module

34907A

Multifunction Module

- 16 bits of digital input and output
- 100 kHz totalizer input
- Two ±12 V analog outputs

The Keysight 34907A allows great flexibility for a variety of sense and control applications. It combines two 8-bit ports of digital input and output, a 100 kHz gated totalizer, and two ±12 V analog outputs—all on a single earth-referenced module. The digital inputs and totalizer input may be included in a scan. Alarm limits for the digital and event counter inputs are evaluated continuously, capturing and logging alarm conditions even between scans.

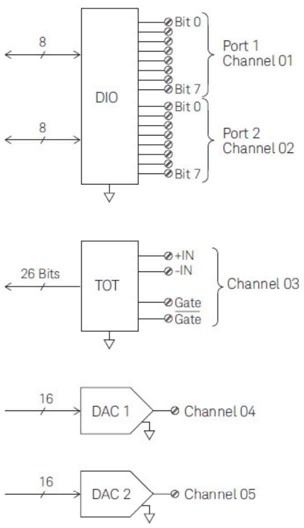

Digital input/ouput

Use the digital outputs with an external power supply to control microwave switches and attenuators, solenoids, power relays, indicators, and more. Use the digital inputs to sense limit switch and digital bus status. There are no complex handshake modes; reads and writes are initiated either from the front panel or the bus.

Port 1, 2	8 bit, input or output, nonisolated
Vin(L)	< 0.8 V (TTL)
Vin(H)	> 2.0 V (TTL)
Vout(L)	< 0.8 V @ Iout = –400 mA
Vout(H)	> 2.4 V @ Iout = 1 mA
Vin(H) max	< 42 V with external open drain pull-up
Alarming	Maskable pattern match or state change
Speed	4 ms (max) alarm sampling
Latency	5 ms (typical) to 34970A alarm output
Read/write speed	95/s

Totalize input

Count events from devices like photo interrupters, limit switches, and Hall-effect sensors.

It keeps an updated total which can be read via the front panel or programmatically at any time. With 26 bits of resolution, it can count events at full speed for nearly 11 minutes without an overflow.

Max count	2^{26} - 1
Totalize input	100 kHz (max) Rising or falling edge, programmable
Signal level	1 Vp-p (min) 42 Vpk (max)
Threshold	0 V or TTL, jumper selectable
Gate Input	TTL-Hi, TTL-Lo, or none
Count reset	Manual or Read + Reset
Read speed	85/s

Analog output

Use the two electronically calibrated analog outputs to source bias voltages to your device under test, to control your analog programmable power supplies, or use the outputs as setpoints for your control systems. The outputs are programmed directly in volts, either from the front panel or from the bus.

DAC 1, 2	±12 V, nonisolated
Resolution	1 mV
IOUT	10 mA max
Settling time	1 ms to 0.01% of output
Accuracy	±(% of output + mV)
1 year ±5°C	0.25% + 20 mV
Temp. coefficient	±(0.015% + 1 mV)/°C

A.5 Technical datasheet Kipp and Zonnen CMP11 Pyranometer

Technical Specifications

	CMP10 | CMP11	SMP10 | SMP11
Classification to ISO 9060:2018	Spectrally Flat Class A	Spectrally Flat Class A
Sensitivity	7 to 14 μV/W/m²	-
Impedance	10 to 100 Ω	-
Expected output range (0 to 1500 W/m²)	0 to 20 mV	-
Maximum operational irradiance	4000 W/m²	-
Analog output • V-version	-	0 to 1 V
Analog output range*	-	-200 to 2000 W/m²
Analog output • A-version	-	4 to 20 mA
Analog output range*	-	0 to 1600 W/m²
Serial output	-	RS-485 Modbus®
Serial output range	-	-400 to 4000 W/m²
Response time (63 %)	< 1.7 s	< 0.7 s
Response time (95 %)	< 5 s	< 2 s
Spectral range (20 % points)	270 to 3000 nm	270 to 3000 nm
Spectral range (50 % points)	285 to 2800 nm	285 to 2800 nm
Zero offsets (unventilated) (a) thermal radiation (at 200 W/m²) (b) temperature change (5 K/h)	 < 7 W/m² < 2 W/m²	 < 7 W/m² < 2 W/m²
Non-stability (change/year)	< 0.5 %	< 0.5 %
Non-linearity (100 to 1000 W/m²)	< 0.2 %	< 0.2 %
Directional response (up to 80 ° with 1000 W/m² beam)	< 10 W/m²	< 10 W/m²
Spectral selectivity (350 to 1500 nm)	< 3 %	< 3 %
Tilt response (0 ° to 90 ° at 1000 W/m²)	< 0.2 %	< 0.2 %
Temperature response	< 1 % (-10 °C to +40 °C)	< 1 % (-20°C to +50 °C) < 2 % (-40 °C to +70 °C)
Field of view	180 °	180 °
Accuracy of bubble level	< 0.1 °	< 0.1 °
Power consumption (at 12 VDC)	-	V-version: 55 mW A-version: 100 mW
Supply voltage	-	5 to 30 VDC
Software, Windows™	-	SmartExplorer Software, for configuration, test and data logging
Detector type	Thermopile	Thermopile
Operating and storage temperature range	-40 °C to +80 °C	-40 °C to +80 °C
Humidity range	0 to 100 %	0 to 100 %
MTBF (Mean Time Between Failures)	> 10 years	> 10 years **
Ingress Protection (IP) rating	67	67
Recommended applications	Meteorological networks, PV panel and thermal collector testing, materials testing	High performance for PV panel and thermal collector testing, solar energy research, solar prospecting, materials testing, advanced meteorology and climate networks

Note: **The performance specifications quoted are worst-case and/or maximum values.**
*** adjustable with SmartExplorer Software | ** extrapolated after introduction in January 2012**

Dimensions

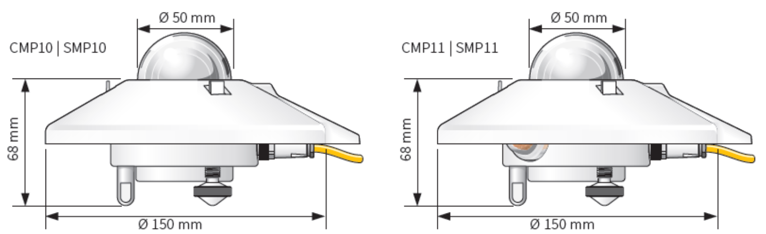

A.6 Technical datasheet Kipp and Zonnen CHP1 Pyrheliometer

Specifications	CHP 1	SHP1
ISO 9060:1990 CLASSIFICATION	First Class	First Class
Response time (63 %)	< 0.7 s → < 1.7 s	< 0.7 s
Response time (95 %)	< 5 s	< 2 s
Zero offsets due to temperature change (5 K/hr)	< 1 W/m²	< 1 W/m²
Non-stability (change/year)	< 0.5 %	< 0.5 %
Non-linearity (0 to 1000 W/m²)	< 0.2 %	< 0.2 %
Temperature dependence of sensitivity	< 0.5 % (-20 °C to +50 °C)	< 0.5 % (-30 °C to +60 °C)
Sensitivity	7 to 14 µV/W/m²	NA
Other specifications		
Analogue output	10 to 20 mV for 1400 W/m²	-V version: 0 to 1 V -A version: 4 to 20 mA
Analogue output range	0 to 4000 W/m²	-V version: -200 to 2000 W/m² (1) -A version: 0 to 1600 W/m²
Digital output	NA	2-wire RS-485, Modbus® protocol
Operating temperature	-40 °C to +80 °C	-40 °C to +80 °C
Full viewing angle	5° ±0.2°	5° ±0.2°
Maximum irradiance	4000 W/m²	4000 W/m²
Humidity	0 to 100% RH	0 to 100% RH
Spectral range (50 % points)	200 to 4000 nm	200 to 4000 nm
Required sun tracker accuracy	< 0.5° from ideal	< 0.5° from ideal
Weight (excluding cable)	0.9 kg	0.9 kg
Slope angle	1° ±0.2°	1° ±0.2°
Temperature sensor	Both Pt-100 and 10k thermistor as standard (2)	Internal (3)
Supply voltage	NA	5 to 30 VDC
Power consumption (at 12 VDC)	NA	-V version: 55 mW -A version: 100 mW
Expected daily uncertainty	< 1 %	< 1 %
Documentation	Calibration certificate traceable to WRR, multi-language instruction sheet, manual on CD-ROM	
Recommended applications	High performance direct radiation monitoring for meteorological stations or concentrated solar energy applications	

(1) The analogue output range of SHP1 can be rescaled by the user to a maximum of -200 to 4000 W/m²

(2) Supplied with individual temperature dependence test data

(3) Output data individually temperature corrected for each SHP1 over -40°C to +70°C

Pyheliometers have a standard cable length of 10 m. Optional cable lengths 25 m and 50 m

Note: The performance specifications quoted are worst-case and/or maximum values

KIPP & ZONEN
SINCE 1830

Go to www.kippzonen.com for your local distributor

A.7 Technical datasheet Eko MS-700 Spectroradiometer

EKO MS-700 Specifications *(Typical)*		
Sensor head	**MS-700**	**MS-700 DNI**
Wavelength range	350 to 1050 nm	
Wavelength interval	3.3 nm	
Spectral resolution FWHM	10 nm	
Wavelength accuracy	<0.3 nm	
Exposure time	10 ms to 5 s	
Temp. dependency (–20° to 50°C)	< ± 1 %	
Temperature control	25 ± 5ºC	
Cosine response (0º to 80º)	<7%	–
Aperture	180°	5°
Slope angle	–	1°
Stray light	0.15%	
Window material	Optical glass	Quartz glass
Communication	RS-422 (Between head and power supply)	
Cable length	10 m (Optional max. 30 m)	
Power requirements	12 Vdc, 50 VA (power supply)	
Operating temperature range (°C)	–20 to +50	
Dimensions (sensor)	200(φ)×175(H) mm (With sun screen: 240(φ)×175(H) mm)	200(φ)×300(H) mm
Weight (sensor)	4 kg	4.5 kg
Power supply		
AC supply voltage	AC100-240V, 50/60 Hz, 50 VA	
DC supply voltage	DC 12 V	
Operating environment	Temperature: 0º to 40ºC, Relative Humidity: 0 to 90%, non-condensing	
Dimensions	200 (W) x 140 (D) x 80 (H) mm	
Weight	1 kg	

A.8 Technical datasheet Tri-band Spectro-Heliometer IES-UPM ICU-3J24

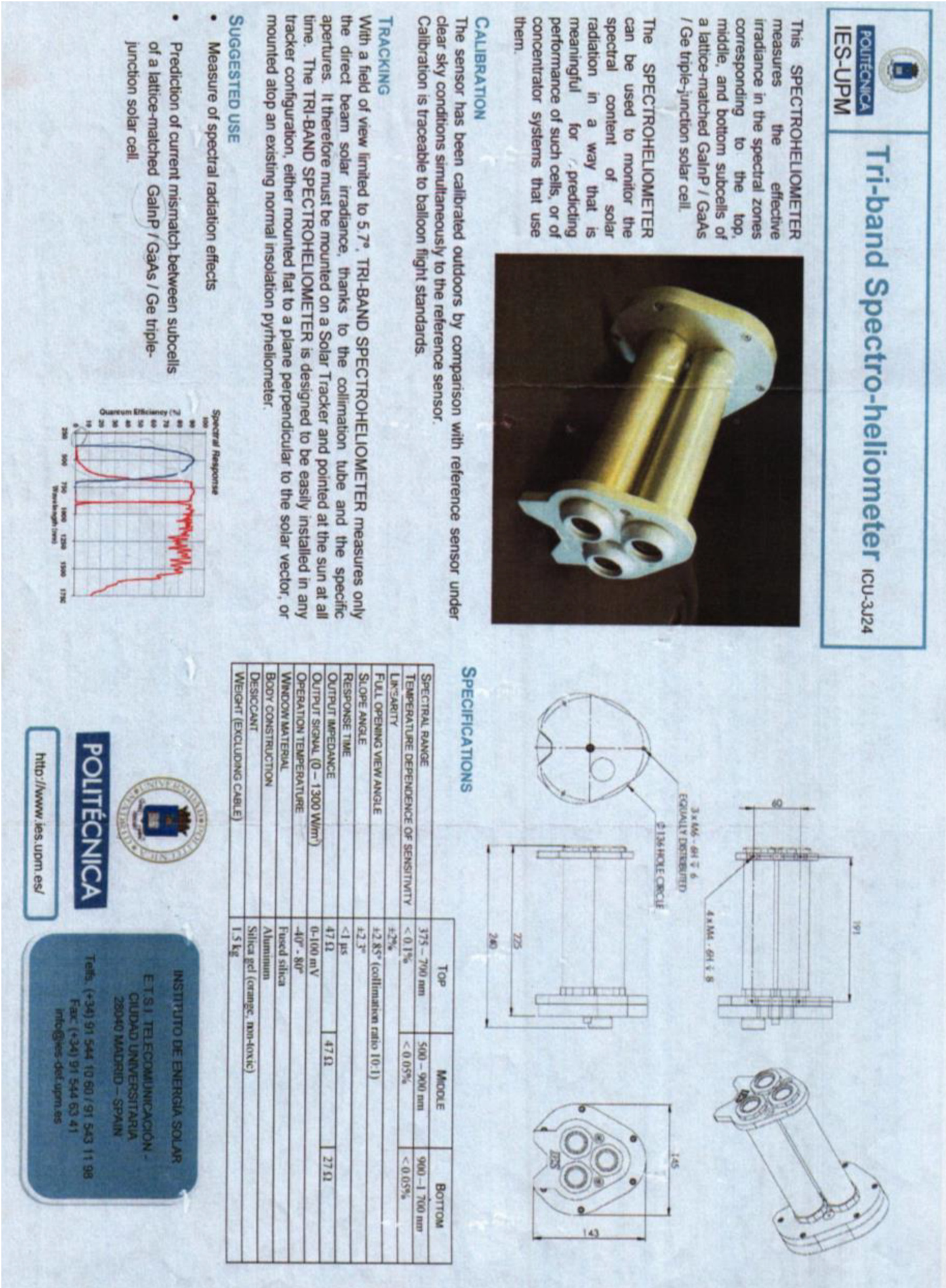

POLITÉCNICA IES-UPM

Tri-band Spectro-heliometer ICU-3J24

This SPECTROHELIOMETER measures the effective irradiance in the spectral zones corresponding to the top, middle, and bottom subcells of a lattice-matched GaInP / GaAs / Ge triple-junction solar cell.

The SPECTROHELIOMETER can be used to monitor the spectral content of solar radiation in a way that is meaningful for predicting performance of such cells, or of concentrator systems that use them.

CALIBRATION

The sensor has been calibrated outdoors by comparison with reference sensor under clear sky conditions simultaneously to the reference sensor. Calibration is traceable to balloon flight standards.

TRACKING

With a field of view limited to 5.7°, TRI-BAND SPECTROHELIOMETER measures only the direct beam solar irradiance, thanks to the collimation tube and the specific apertures. It therefore must be mounted on a Solar Tracker and pointed at the sun at all time. The TRI-BAND SPECTROHELIOMETER is designed to be easily installed in any tracker configuration, either mounted flat to a plane perpendicular to the solar vector, or mounted atop an existing normal insolation pyrheliometer.

SUGGESTED USE

- Measure of spectral radiation effects
- Prediction of current mismatch between subcells of a lattice-matched GaInP / GaAs / Ge triple-junction solar cell.

SPECIFICATIONS

	TOP	MIDDLE	BOTTOM
SPECTRAL RANGE	375 – 700 nm	500 – 900 nm	900 – 1 700 nm
TEMPERATURE DEPENDENCE OF SENSITIVITY	< 0.1%	< 0.05%	< 0.05%
LINEARITY	±2%		
FULL OPENING VIEW ANGLE	±2.85° (collimation ratio 10:1)		
SLOPE ANGLE	±2.3°		
RESPONSE TIME	<1 μs		
OUTPUT IMPEDANCE	47 Ω	47 Ω	27 Ω
OUTPUT SIGNAL (0 – 1300 W/m²)	0-100 mV		
OPERATION TEMPERATURE	-40° - 80°		
WINDOW MATERIAL	Fused silica		
BODY CONSTRUCTION	Aluminum		
DESICCANT	Silica gel (orange, non-toxic)		
WEIGHT (EXCLUDING CABLE)	1.5 kg		

POLITÉCNICA

http://www.ies.upm.es/

INSTITUTO DE ENERGÍA SOLAR
E.T.S.I. TELECOMUNICACIÓN - CIUDAD UNIVERSITARIA
28040 MADRID – SPAIN
Telfs. (+34) 91 544 10 60 / 91 543 11 98
Fax: (+34) 91 544 63 41
info@ies-def.upm.es

A.9 Technical datasheet Young 05305VM anemometer

MODEL 05305V
WIND MONITOR-AQ
with VOLTAGE OUTPUTS

WIND SPEED SPECIFICATION SUMMARY

Range	0 to 40 m/s (90 mph), gust survival 100 m/s (220 mph)
Sensor	20 cm diameter 4-blade helicoid carbon fiber thermoplastic propeller, 30.7 cm air passage per revolution
Distance Constant	2.1 m (6.9 ft.) for 63% recovery
Threshold Sensitivity	0.4 m/s (0.9 mph)
Transducer	Centrally mounted stationary coil, 2K Ohm nominal DC resistance
Output Signal	0 to 1.00 VDC over specified range

Model No. Suffix	Range
M	0 to 50 M/S
P	0 to 100 MPH
N	0 to 100 KNOTS
K	0 to 200 KILOMETERS/HOUR

WIND DIRECTION (AZIMUTH) SPECIFICATION SUMMARY

Range	360° mechanical, 355° electrical (5° open)
Sensor	Balanced vane, 48.3 cm (19 in) turning radius.
Damping Ratio	0.45
Delay Distance	1.2 m (3.9 ft) for 50% recovery
Threshold Sensitivity	0.5 m/s (1.0 mph) at 10° displacement
Damped Natural Wavelength	4.9 m (16.1 ft)
Undamped Natural Wavelength	4.4 m (14.4 ft)
Transducer	Precision conductive plastic potentiometer, 10K ohm resistance (±20%), 0.25% linearity, life expectancy 50 million revolutions, rated 1 watt at 40°C, 0 watts AT 125°C
Output Signal	0 to 1.00 VDC for 0 to 360°

GENERAL

Power Requirement: 8 - 24 VDC (5mA @ 12 VDC)
Operating Temperature: -50 to 50°C (-58 to 122°F)

INTRODUCTION

The Wind Monitor measures horizontal wind speed and direction. Developed for air quality applications, it is accurate, sensitive, and corrosion resistant. The main housing, nose cone, propeller, and other internal parts are injection molded U.V. stabilized plastic. The tail section is lightweight expanded polystyrene. Both the propeller and vertical shafts use stainless steel precision grade ball bearings. Bearings have shields to help exclude contamination and moisture.

Propeller rotation produces an AC sine wave signal with frequency proportional to wind speed. Internal circuitry converts the raw signal to a linear voltage output.

Vane position is sensed by a 10K ohm precision conductive plastic potentiometer. This signal is also converted to voltage output.

The instrument mounts directly on standard one inch pipe, outside diameter 34 mm (1.34"). An orientation ring is provided so the instrument can be removed for maintenance and re-installed without loss of wind direction reference. Both the sensor and the orientation ring are secured to the mounting pipe by stainless steel band clamps. Electrical connections are made in a junction box at the base.

INITIAL CHECKOUT

When the Wind Monitor is unpacked it should be checked carefully for any signs of shipping damage.

Remove the plastic nut on the propeller shaft. Install the propeller on the shaft with the serial number of the propeller facing forward (into the wind). The instrument is aligned, balanced and fully calibrated before shipment; however, it should be checked both mechanically and electrically before installation. The vane and propeller should easily rotate 360° without friction. Check vane balance by holding the instrument base so the vane surface is horizontal. It should have near neutral torque without any particular tendency to rotate. A slight imbalance will not degrade performance.

INSTALLATION

Proper placement of the instrument is very important. Eddies from trees, buildings, or other structures can greatly influence wind speed and wind direction observations. To get meaningful data for most applications, locate the instrument well above or upwind from obstructions. As a general rule, the air flow around a structure is disturbed to twice the height of the structure upwind, six times the height downwind, and up to twice the height of the structure above ground. For some applications it may not be practical or necessary to meet these requirements.

FAILURE TO PROPERLY GROUND THE WIND MONITOR MAY RESULT IN ERRONEOUS SIGNALS OR TRANSDUCER DAMAGE.

Grounding the Wind Monitor is vitally important. Without proper grounding, static electrical charge can build up during certain atmospheric conditions and discharge through the transducers. This discharge may cause erroneous signals or transducer failure.

A.10 Technical datasheet Young 41382VC Relative Humidity and Temperature Probe

MODEL 41382VC
RELATIVE HUMIDITY / TEMPERATURE PROBE
with VOLTAGE OUTPUT

YOUNG

INSTRUCTION SHEET 41382VC-90
REV E102613

INTRODUCTION

The Model 41382VC Relative Humidity/Temperature Probe combines high accuracy humidity and temperature sensors in a single probe. The output signal is 0-1 V (standard) or 0-5 V (user selected option) for both relative humidity and temperature. RH range is 0-100%. Temperature range is -50 to +50°C.

INSTALLATION

Install the probe in a naturally ventilated or fan aspirated radiation shield. Mount probe and shield in a location with good air circulation clear of large thermal masses (buildings, pavement, solar panels, etc.), exhaust vents, electrical machinery and motors, water fountains and sprinklers.

Set 0-1 V or 0-5 V output with jumpers as shown in diagram. These jumpers are located below the terminals in the junction box.

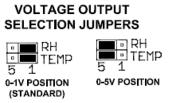

MAINTENANCE

The probe provides years of service with minimal maintenance. Humidity calibration, which may drift slightly with time, can be checked or restored at the factory.

Periodically clean the humidity sensor filter when used in areas of high dust or contamination (smokestacks, seawater, etc.) Soak in clean water or use a mild soap solution. DO NOT USE SOLVENTS.

CE COMPLIANCE

This product complies with the European CE directive on EMC compatibility. Shielded cable must be used.

WARRANTY

This product is warranted to be free of defects in materials and construction for a period of 12 months from date of initial purchase. Liability is limited to repair or replacement of defective item. A copy of the warranty policy may be obtained from R. M. Young Company.

SPECIFICATIONS

RELATIVE HUMIDITY:	
Measuring range:	0-100% RH
Accuracy at 23°C:	±1%
Stability:	Better than ±1%RH per year
Response Time:	10 seconds (Without Filter)
Sensor type:	Rotronic Hygromer
TEMPERATURE:	
Measuring Range:	-50 to +50°C
Accuracy at 23°C:	±0.3°C
Response Time:	10 seconds (Without Filter)
Sensor type:	Platinum RTD
Output signal:	0-1 or 0-5 VDC (jumper option)
Power Required:	8-30 VDC at 7 mA
Recommended Cable:	5 conductor shielded, Young 18446

Recommended Shields:
Young Model 43502 Aspirated Radiation Shield
Young Model 41003P Multi-Plate Radiation Shield

Declaration of Conformity

R. M. Young Company
2801 Aero Park Drive
Traverse City, MI 49686 USA

Model 41382VC RH/Temp Probe
The undersigned hereby declares on behalf of R. M. Young Company that the above-referenced product, to which this declaration relates, is in conformity with the provisions of:

Council Directive 2004/108/EC (December 15, 2004)
on Electromagnetic Compatibility

David Poinsett
R&D Manager

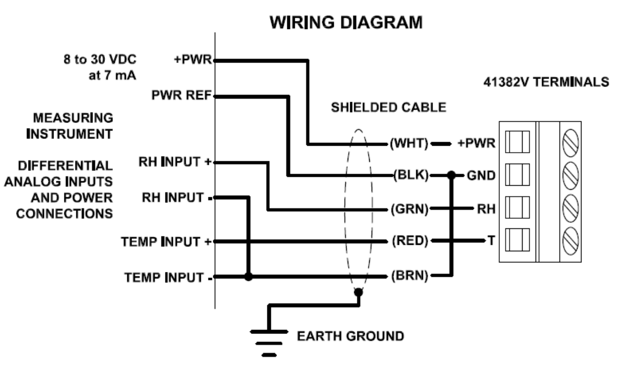

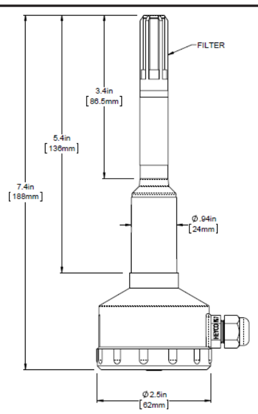

R. M. YOUNG COMPANY 2801 Aero Park Drive , Traverse City, Michigan 49686 USA
TEL (231) 946-3980 FAX (231) 946-4772

A.11 Technical datasheet Vaisala BAROCAP PTB110 barometer

Technical Data

Measurement Performance

Pressure range (1 hPa = 1 mbar)	500 ... 1 100 hPa 600 ... 1100 hPa 800 ... 1100 hPa 800 ... 1060 hPa 600 ... 1060 hPa
Resolution	0.1 hPa
Load resistance	10 000 Ω minimum
Load capacitance	47 nF maximum
Settling time to full accuracy after startup	1 s
Response time to full accuracy after a pressure step	500 ms
Acceleration sensitivity	Negligible
Accuracy	
Linearity [1]	±0.25 hPa
Hysteresis [1]	±0.03 hPa
Repeatability [1]	±0.03 hPa
Pressure calibration uncertainty [2]	±0.15 hPa
Voltage calibration uncertainty	± 0.7 mV
Frequency calibration uncertainty	± 0.3 Hz
Accuracy at +20 °C (+68 °F) [3]	±0.3 hPa
Total Accuracy at	
+15 ... +25 °C (+59 ... +77 °F)	±0.3 hPa
0 ... +40 °C (+32 ... +104 °F)	±0.6 hPa
−20 ... +45 °C (−4 ... +113 °F)	±1.0 hPa
−40 ... +60 °C (−40 ... +140 °F)	±1.5 hPa
Long-term stability	±0.1 hPa / year

1) *Defined as ±2 standard deviation limits of end-point non-linearity, hysteresis error, or repeatability error.*
2) *Defined as ±2 standard deviation limits of inaccuracy of the working standard including traceability to international standards.*
3) *Defined as the root sum of the squares (RSS) of end-point non-linearity, hysteresis error, repeatability error, and calibration uncertainty at room temperature.*

Operating Environment

Operating temperature	−40 ... +60 °C (−40 ... +140 °F)
Storage temperature	−40 ... +60 °C (−40 ... +140 °F)
Operating humidity	Non-condensing
EMC compliance	EN/IEC 61326-1, Electrical equipment for measurement, control and laboratory use - industrial environment

Mechanical Specifications

IP rating	IP32
Dimensions (H × W × D)	97.3 × 68.4 × 28.1 mm (3.83 × 2.69 × 1.10 in)
Weight	90 g (3.2 oz)
Materials	
Housing cover	Plastic ABS/PC blend
Mounting plate	Aluminum

Inputs and Outputs

Supply voltage	10 ... 30 VDC
Supply voltage control	With TTL-level (Transistor-Transistor Logic) trigger
Supply voltage sensitivity	Negligible
Average power consumption	0.10 W at 12 V
Output voltage	0 ... 2.5 VDC 0 ... 5 VDC
Output frequency	500 ... 1100 Hz
Pressure connector	M5 (10 ... 32) internal thread
Pressure fitting	Barbed fitting for ⅛ in
Minimum pressure limit	0 hPa abs
Maximum pressure limit	2000 hPa abs
Electrical connector	A removable connector for 5 wires (AWG 28 ... 16)
Terminals	Pin 1: External triggering Pin 2: Signal ground Pin 3: Supply ground Pin 4: Supply voltage Pin 5: Voltage/Frequency output

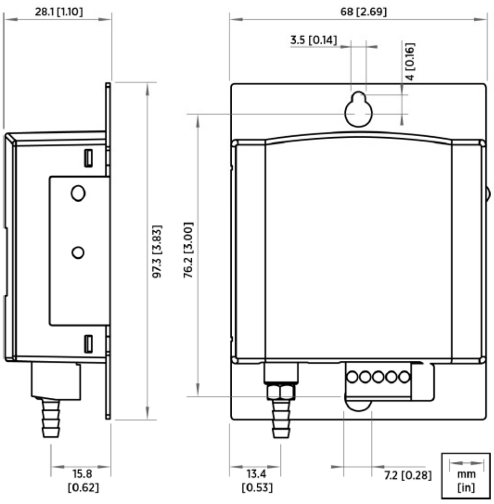

Published by Vaisala | B210681EN-E © Vaisala 2018

www.vaisala.com

A.12 Technical datasheet BSQ D150/6 Solar 2-axes tracker

Specifications

Tracking accuracy *Position resolution* *Solar ephemeris mean accuracy* *Internal clock mean accuracy*	*<0,5˚ (1)* *0,018˚ (2)* *0,01˚ (2)* *±2 min/yr. (0˚C to 50˚C)*
Input power required *Resting consumption* *DC Motor Voltage* *Max. Motor DC current*	*100-240 Vac (60/50Hz)* *0,12 Aac (3)* *24 Vdc* *10 Adc (4)*
Temperature range (operation) *Temperature range (storage)* *Humidity (operation & storage)* *Ingress protection*	*0˚C to 50˚C (5)* *-20˚C to 75˚C* *90% to 100% RH @ 40˚C* *IP65*
Weight (main unit) *Dimensions (main unit)*	*18.5 Kg* *50(h)x40(w)x22(d) cm*
Communication	∞ *RS-232 port: 57.600 baud* ∞ *Ethernet port: 10BASE-T/100BASE-TX compliant*
Electrical features	∞ *Automatic fuse restart* ∞ *Automatic fuses that avoid high motor current in case of accidental collision* ∞ *EMC/EMI compliant* ∞ *Overvoltage protection*

(1) From the mechanical point of view, tracking accuracy is limited on the one hand by the drive employed in the mechanical tracker, basically depending on its backlash and positioning resolution, and on the other by the tolerances in the manufacturing, assembly, and installation of the tracker and occasionally the concentrating optics or tracking modules mounted on its aperture. With tracking drives specially designed or properly chosen for concentration applications, the BSQ Sun Tracking Controller can easily achieve the 0,5˚ accuracy and even get into the 0,1˚ range.

(2) The resolution in the position sensing along with the ephemeris equations accuracy determine the ultimate limit to the tracking accuracy which might be achieved. Position resolution will depend on the sensors employed to determine axes orientation. The value here refers to a main axis mount of the optical incremental encoders usually supplied with the BSQ Sun Trcaking Controller which permit upt to 20.000 pulses/rev. Ephemeris equations internally computed by Sun Tracking Controller have mean accuracies always better than 0,01˚.

(3) Alternate current consumption in resting conditions i.e. with no tracking axis motor being operated, which in most trackers represents most of the time, and using optical encoders as axes position sensors. Consumption in the motor actuation periods will depend on the specific axes drive block employed.

(4) Presently the BSQ Sun Tracking Controller includes a drive board able to control DC motors of up to 24Vdc and a joint current consumption of no more than 10 Adc. This capacity should comply with most applications integrating DC motors, however it can be customized to an specific application on demand.

(5) Case ambient operating temperatures below 0˚C are frequent an enclosure internal heating kit can be supplied to maintain the inner operating temperature above 0˚C

Annex B

Evaluation of tolerance on measure

An evaluation on measurement uncertainty is proposed in this section, according to [39].

B.1 Uncertainty on voltage measure

Voltage of the I-V curve is measured directly with an Agilent 34411A multimeter. The uncertainty on voltage measure can be calculated as equation (12.1).

$$U_V = 2\sqrt{\left(\frac{R_V}{2^n \cdot \sqrt{12}}\right)^2 + \left(\frac{e_V}{\sqrt{3}}\right)^2 + \left(\frac{U_{CV}}{2}\right)^2} \qquad (12.1)$$

Where:

- V_{read} is the reading voltage
- R_V is the multimeter range ($R_V = 100\ V$)
- n is the number of bits of the analog-to-digital converter:

Integration Time (NPLC)	**Number of bits (n)**
0,02	15
0,2	18
1	20
2	21
10	24
100	26

- e_V is the accuracy of the instruments:

$$e_V = 0{,}000040 \cdot V_{read} + (0{,}000006 + A) \cdot R_V \qquad (12.2)$$

A is obtained from this table:

Integration Time (NPLC)	**Resolution (A)**
0,0015	$30 \cdot 10^{-6}$
0,0025	$15 \cdot 10^{-6}$
0,006	$6 \cdot 10^{-6}$
0,02	$3 \cdot 10^{-6}$
0,06	$1{,}5 \cdot 10^{-6}$
0,2	$0{,}7 \cdot 10^{-6}$
1	$0{,}3 \cdot 10^{-6}$
2	$0{,}2 \cdot 10^{-6}$
10	$0{,}1 \cdot 10^{-6}$
100	$0{,}03 \cdot 10^{-6}$

- U_{CV} came from the calibration certificate

B.2 Uncertainty on current intensity measure

Current intensity of the I-V curve is measured indirectly through the measure of the voltage drop across shunt calibrated resistor. The shunt resistor is 10 A – 150 mV ($R_{shunt} = 15\ m\Omega$) of class 0,5. The uncertainty on current measure can be calculated as equation (12.3).

$$U_I = 2\sqrt{\left(\frac{1}{R_{shunt}}\right)^2 \cdot {U_I^V}^2 + \left(\frac{-V_{read}}{R_{shunt}^2}\right)^2 \cdot {U_I^R}^2} \tag{12.3}$$

with:

$$U_I^V = 2\sqrt{\left(\frac{R_V}{2^n \cdot \sqrt{12}}\right)^2 + \left(\frac{e_V}{\sqrt{3}}\right)^2 + \left(\frac{U_{CV}}{2}\right)^2} \tag{12.4}$$

$$U_I^R = \frac{class}{100} \cdot R_{shunt} = \frac{0{,}5}{100} \cdot 0{,}015 = 0{,}000075\ \Omega$$

Where:

- V_{read} is the reading voltage
- R_V is the multimeter range ($R_V = 1\ V$)

- n is number of bits of the analog-to-digital converter:

Integration Time (NPLC)	Number of bits (n)
0,02	15
0,2	18
1	20
2	21
10	24
100	26

- e_V is the accuracy of the instruments:

$$e_V = 0{,}000040 \cdot V_{read} + (0{,}000006 + A) \cdot R_V \tag{12.5}$$

A is obtained from this table:

Integration Time (NPLC)	Resolution (A)
0,0015	$30 \cdot 10^{-6}$
0,0025	$15 \cdot 10^{-6}$
0,006	$6 \cdot 10^{-6}$
0,02	$3 \cdot 10^{-6}$
0,06	$1{,}5 \cdot 10^{-6}$
0,2	$0{,}7 \cdot 10^{-6}$
1	$0{,}3 \cdot 10^{-6}$
2	$0{,}2 \cdot 10^{-6}$
10	$0{,}1 \cdot 10^{-6}$
100	$0{,}03 \cdot 10^{-6}$

- U_{CV} came from the calibration certificate

B.3 Uncertainty on irradiance measure

Irradiance is measured with pyranometer that provides as output a voltage linearly proportional to the measured irradiance. The calibration constant is provided in the calibration certificate. The uncertainty on irradiance measure can be calculated as equation (12.6).

$$U_G = 2 \cdot \sqrt{\begin{aligned}&\left(\frac{U_{V_{FP}}}{2 \cdot S}\right)^2 + \left(\frac{U_C \cdot G}{2 \cdot S_C}\right)^2 + \left(\frac{U_{DR} \cdot G}{\sqrt{3}}\right)^2 + \left(\frac{U_{SS} \cdot G}{\sqrt{3}}\right)^2 + \left(\frac{U_{TD} \cdot G}{\sqrt{3}}\right)^2 + \\ &+ \left(\frac{U_{NL} \cdot G}{\sqrt{3}}\right)^2 + \left(\frac{U_{TR} \cdot G}{\sqrt{3}}\right)^2 + \left(\frac{U_{NS} \cdot G}{\sqrt{3}}\right)^2 + \left(\frac{U_{TC}}{\sqrt{3}}\right)^2 + \left(\frac{U_{RT}}{\sqrt{3}}\right)^2\end{aligned}} \tag{12.6}$$

Where:

- G is the value of the measured irradiance ($G = \frac{V_{FP}}{S}$)
- V_{FP} is the voltage value measured by the instrument (Datalogger)
- $U_{V_{FP}}$ is the uncertainty on the V_{FP} ($U_{V_{FP}} =$)
- S is the sensitivity of the pyranometer from calibration certificate

  ($S = \frac{1}{95246} = 0{,}00001049912 \frac{V}{\frac{W}{m^2}}$)
- U_C is the uncertainty on the calibration pyranometer sensitivity
- S_C is the sensitivity of the calibration pyranometer from calibration certificate
- U_{DR} is the directional response error from the calibration certificate (as a tabular function of the angle of incidence (AOI)
- AOI is the angle of incidence and it could be calculated from the latitude, date and tilt
- U_{SS} is the Spectral selectivity from manufacturer datasheet ($U_{SS} = 0{,}03$)
- U_{TD} is the maximum temperature dependence from manufacturer datasheet ($U_{TD} = 0{,}01$)
- U_{NL} is the non-linearity of the pyranometer from manufacturer datasheet ($U_{NL} = 0{,}002$)
- U_{TR} is the tilt response of the pyranometer from manufacturer datasheet ($U_{TR} = 0{,}002$)
- U_{NS} is the non-stability of the pyranometer from manufacturer datasheet ($U_{NS} = 0{,}005$)
- U_{TC} is the uncertainty due to the change in temperature from manufacturer datasheet

  ($U_{TC} = 7 \frac{W}{m^2}$)
- U_{RT} is the uncertainty due to the radiative transfer to the atmosphere from manufacturer datasheet ($U_{RT} = 2 \frac{W}{m^2}$)

B.4 Uncertainty on module temperature measure

The module temperature is measured with a resistance temperature detector (RTD). The RTDs are composed of pure material, typically platinum, nickel, or copper. Each material has an accurate resistance/temperature relationship which is used to provide an indication of temperature. In this case a Pt100 sensor is used (TCR 0,00385 Ω/Ω/°C). The uncertainty on temperature measure can be calculated as equation (12.7).

$$U_T = 2 \cdot \sqrt{\left(\frac{T_{max} - T_{min}}{2^n \cdot \sqrt{12}}\right)^2 + u_A^2 + \left(\frac{u_A}{4}\right)^2 + \left(\frac{U_{Pt100}}{\sqrt{3}}\right)^2 + \left(\frac{U_{COT}}{\sqrt{3}}\right)^2} \tag{12.7}$$

Where:

- T_{max} and T_{min} are the temperature range extreme of the ADC ($T_{max} = {}^\circ C \mid T_{min} = {}^\circ C$)
- n is the number of bits of the ADC
- u_A is the temperature accuracy of the ADC
- U_{Pt100} is the tolerance of the Pt100 sensor, in our case of class B Pt100, is given by this expression:

$$U_{Pt100} = 5{,}0 \cdot 10^{-3} \cdot |T_M| + 3{,}0 \cdot 10^{-1} \tag{12.8}$$

- U_{COT} is the uncertainty connected to the cell-to-backskin temperature drop systematic error and the relative correction

Annex C

Datasheet of Sanyo HIT-240HDE4 module

Think GAIA
For Life and the Earth

SANYO

HIT® photovoltaic module

HIT-240HDE4
HIT-235HDE4

The SANYO HIT® (Heterojunction with Intrinsic Thin layer) solar cell is made of a thin mono crystalline silicon wafer surrounded by ultra-thin amorphous silicon layers. This product provides the industry's leading performance and value using state-of-the-art manufacturing techniques.

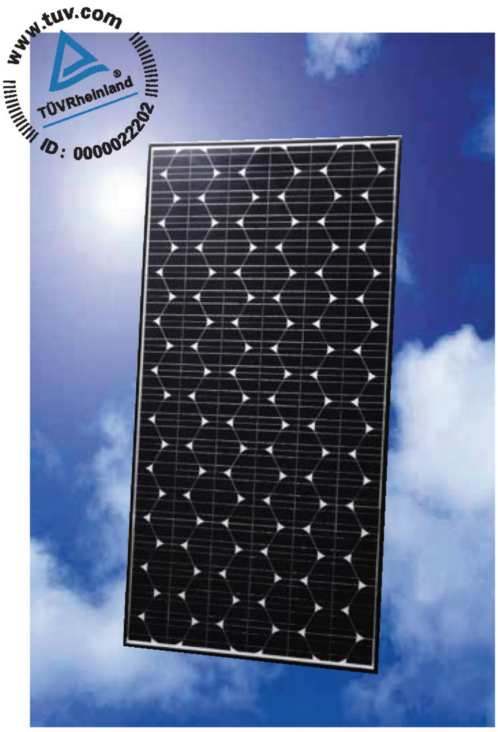

HIT® Solar Cell Structure

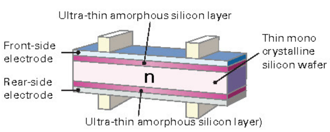

Development of HIT® solar cell was supported in part by the New Energy and Industrial Technology Development Organization (NEDO).

Benefit in Terms of Performance

The HIT® cell and module have very high conversion efficiency in mass production.

Model	Cell Efficiency	Module Efficiency
HIT-240HDE4	20.0%	17.3%
HIT-235HDE4	19.6%	16.9%

High performance at high temperatures
Even at high temperatures, the HIT® solar cell can maintain higher efficiency than a conventional crystalline silicon solar cell.

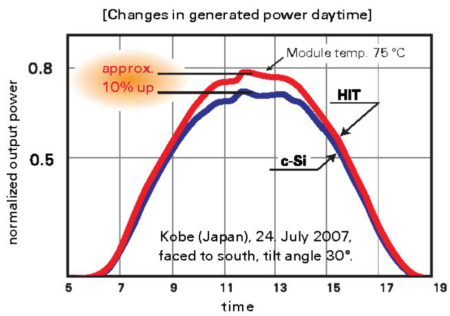

Environmentally-Friendly Solar Cell

More Clean Energy
HIT® can generate more clean Energy than other conventional crystalline solar cells.

A module that uses silicon resources effectively

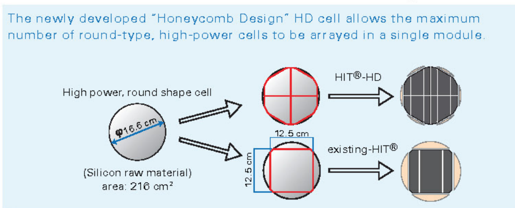

HIT HD
Photovoltaic Module

HIT
Photovoltaic Module

Electrical and Mechanical Characteristics HIT-240HDE4, HIT-235HDE4

Technical data	Models HIT-xxxHDE4 240	235
Maximum power (Pmax) [W]	240	235
Max. power voltage (Vpm) [V]	35.5	35.1
Max. power current (Ipm) [A]	6.77	6.70
Open circuit voltage (Voc) [V]	43.6	43.4
Short circuit current (Isc) [A]	7.37	7.33
Warranted min. power (Pmin) [W]	228.0	223.3
Maximum over current rating [A]	15	
Output power tolerance [%]	+10/-5	
Max. system voltage [Vdc]	1000	
Temperature coeff. of Pmax [%/°C]	-0.30	
Temperature coeff. of Voc [V/°C]	-0.109	-0.109
Temperature coeff. of Isc [mA/°C]	2.21	2.20

Note 1: Standard test conditions: Air mass 1.5, Irradiance = 1000 W/m², Cell temperature = 25°C.
Note 2: The values in the above table are nominal.

Reference data for model HIT-240HDE4

Dependence on irradiance

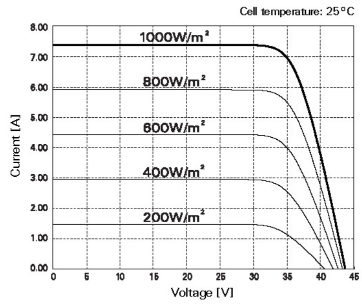

Dimensions and weight

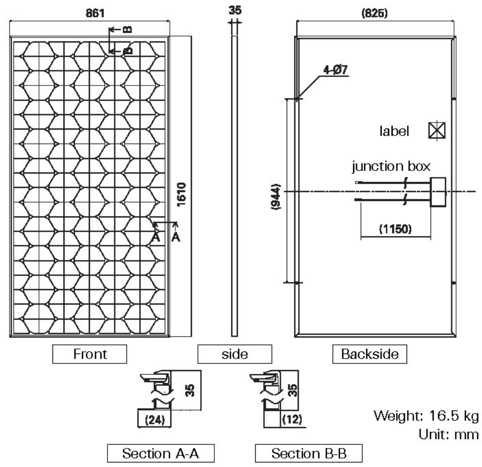

Weight: 16.5 kg
Unit: mm

Dependence on temperature

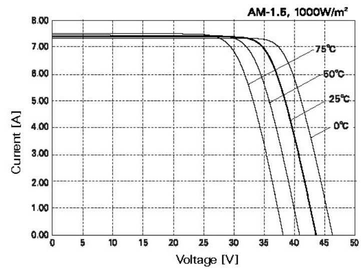

Certificates

IEC 61730 IEC 61215

Electrical Protection Class II

Please consult your local dealer for more information.

Guarantee

Product: 5 years
Power output: 10 years (90% of Pmin), 20 years (80% of Pmin)
Full conditions are available on our website.

⚠ **CAUTION!** Please read the operating instructions carefully before using the products.

Due to our policy of continual improvement the products covered by this brochure may be changed without notice.

SANYO Component Europe GmbH
Solar Division

Stahlgruberring 4
81829 Munich, Germany
Tel.+49-(0)89-460095-0
Fax.+49-(0)89-460095-170
http://www.sanyo-solar.eu
email: info.solar@sanyo-solar.eu

SANYO Electric Co., Ltd.
Solar Division

http://www.sanyo.com/solar
email: homepage_solar@sanyo.com

09/09

Annex D

Additional 3D plot of the parameters correlations results

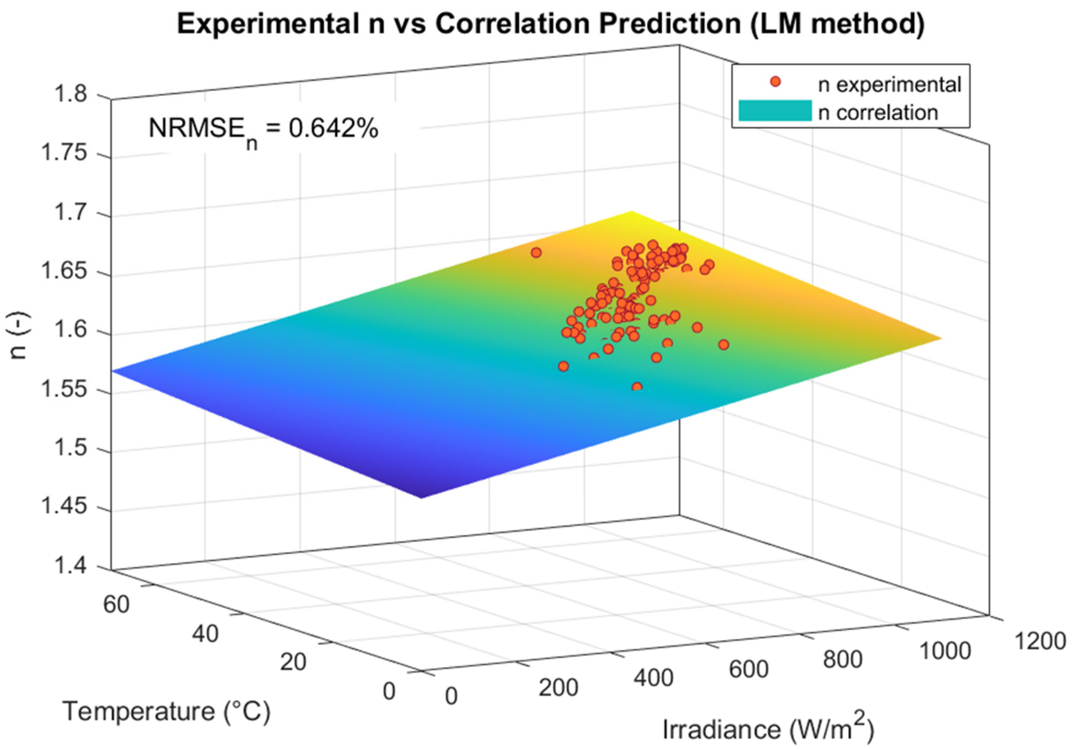
Experimental n vs Correlation Prediction (LM method)
n experimental
n correlation
NRMSE$_n$ = 0.642%
1.8
1.75
1.7
1.65
1.6
1.55
1.5
1.45
1.4
n (-)
60
40
20
0
Temperature (°C)
0
200
400
600
800
1000
1200
Irradiance (W/m^2)

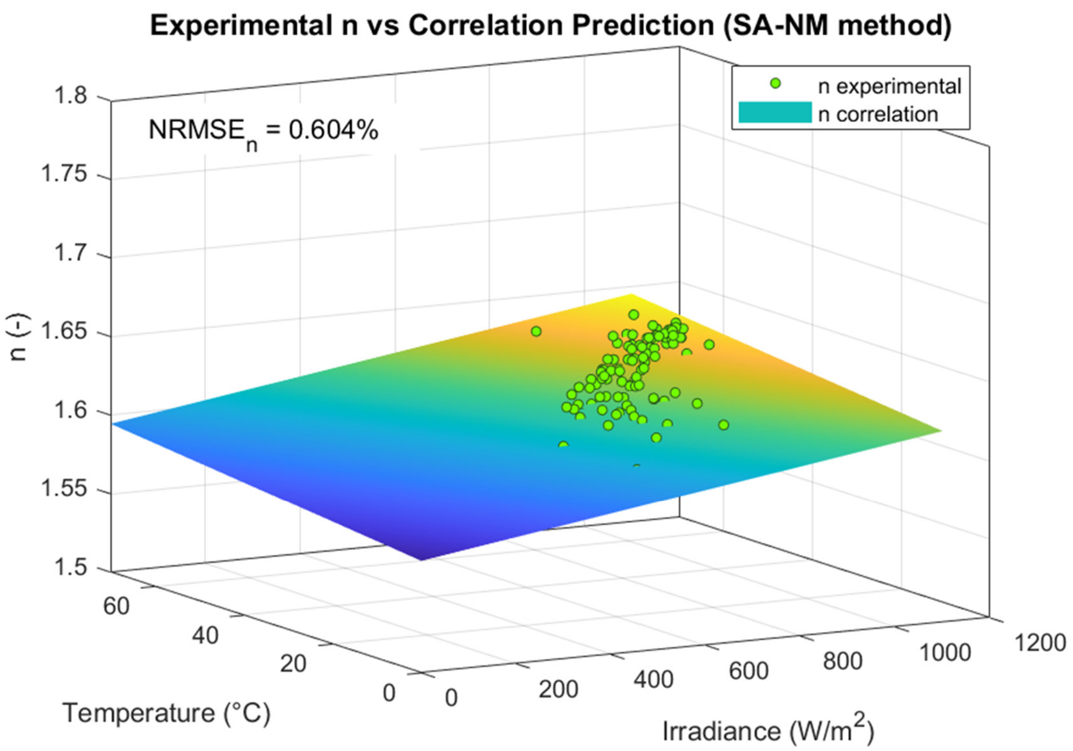
Experimental n vs Correlation Prediction (SA-NM method)
n experimental
n correlation
NRMSE$_n$ = 0.604%
1.8
1.75
1.7
1.65
1.6
1.55
1.5
n (-)
60
40
20
0
Temperature (°C)
0
200
400
600
800
1000
1200
Irradiance (W/m^2)

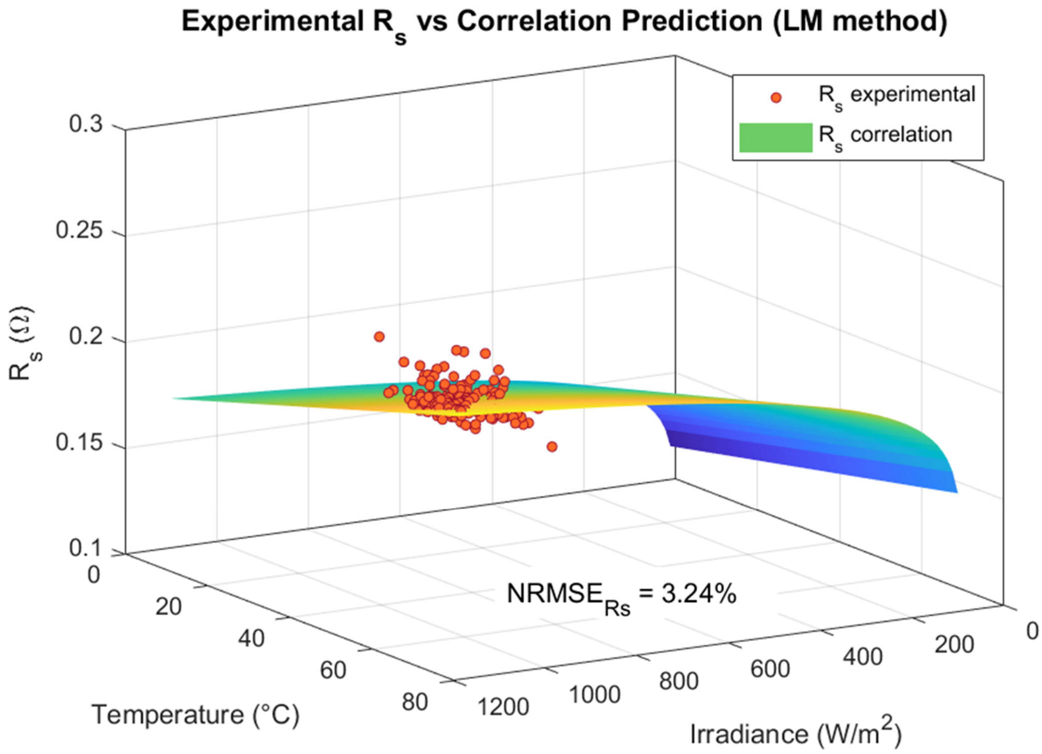

Experimental R_s vs Correlation Prediction (LM method)
R_s experimental
R_s correlation
R_s (Ω)
0.3
0.25
0.2
0.15
0.1
$NRMSE_{Rs}$ = 3.24%
Temperature (°C)
0
20
40
60
80
Irradiance (W/m^2)
1200
1000
800
600
400
200
0

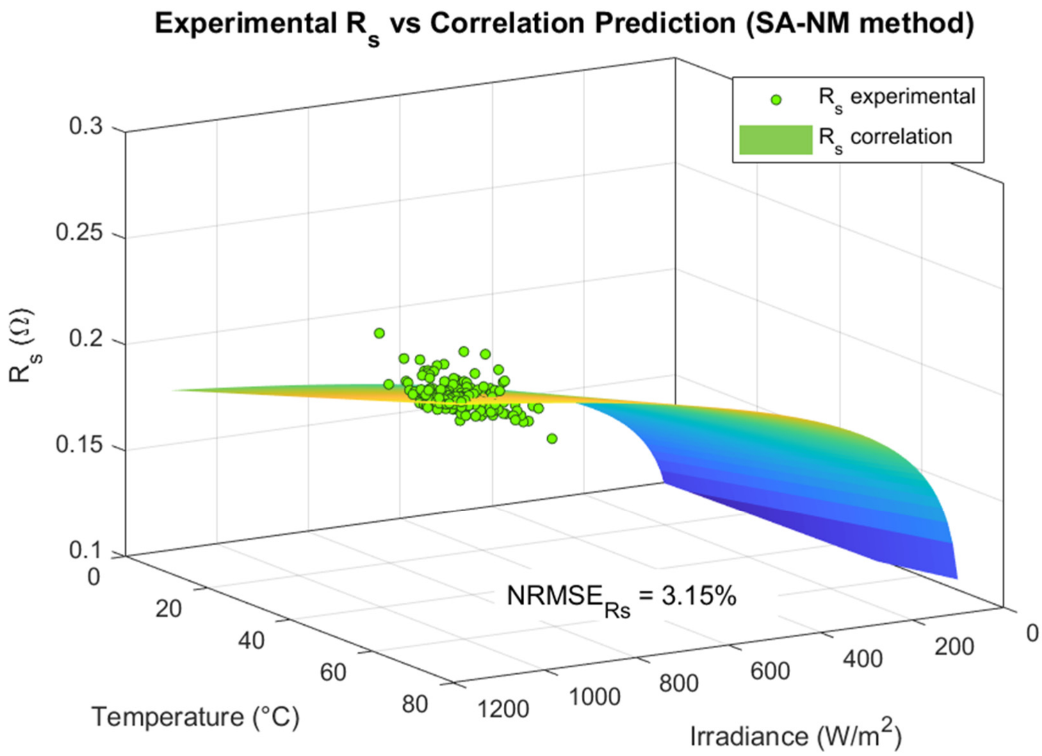

Experimental R_s vs Correlation Prediction (SA-NM method)
R_s experimental
R_s correlation
R_s (Ω)
0.3
0.25
0.2
0.15
0.1
$NRMSE_{Rs}$ = 3.15%
Temperature (°C)
0
20
40
60
80
Irradiance (W/m^2)
1200
1000
800
600
400
200
0

References

[1] European Commission, "A Clean Planet for all. A European strategic long-term vision for a prosperous, modern, competitive and climate neutral economy," European Commission, Brussels, 2018.

[2] EurObserv'ER, «Photovoltaic Barometer 2020,» EurObserv'ER, 2020.

[3] M. Alonso Abella, Sistemas fotovoltaicos: introducción al diseño y dimensionado de instalaciones solares fotovoltaicas, Madrid: SAPT Publicaciones Técnicas S.L., 2005.

[4] D. Murgia, «Tecniche per l'identificazione dei difetti e per l'analisi delle performance nei moduli fotovoltaici,» Politecnico di Torino, Tesi di Laurea Magistrale, 2018.

[5] A. Scaiola, «Innovative technique to estimate the performance of a photovoltaic generator using the parameters of the single diode model equivalent circuit,» Politecnico di Torino, Tesi di Laurea Magistrale, 2019.

[6] National Renewable Energy Laboratory (NREL), «Champion Photovoltaic Module Efficiency Chart,» NREL, 2019.

[7] [Online]. Available: https://www.futurasun.com/wp-content/uploads/2018/04/pannello-monocristallino_dettaglio.jpg.

[8] [Online]. Available: http://www.fotovoltaicosulweb.it/immagini/upload/guida/policristalline_panels1.jpg.

[9] SANYO Component Europe GmbH Solar Division, «HIT-240HDE4 HIT-235HDE4 datasheet,» SANYO Component Europe GmbH, 2009.

[10] [Online]. Available: https://www.vpsolar.com/wp-content/uploads/2018/04/tecnologia-perc-funzionamento.jpg.

[11] [Online]. Available: https://zeroemission.eu/wp-content/uploads/2020/02/Thin-film-Solar-Cell-425x405.jpg.

[12] [Online]. Available: https://solarconsultant.ca/wp-content/uploads/2017/05/Silicon-Solar-Cell-Construction.png.

[13] [Online]. Available: https://opentextbc.ca/chemistry/wp-content/uploads/sites/150/2016/05/CNX_Chem_08_04_Band.jpg.

[14] National Renewable Energy Laboratory (NREL), "Best Research-Cell Efficiency Chart," NREL, 2020.

[15] S. Mishra e D. Sharma, «Control of photovoltaic technology,» in *Electric Renewable Energy Systems*, Elsevier, 2016, pp. 457-486.

[16] A. Haque, «Solar energy,» in *Electric Renewable Energy Systems*, Elsevier, 2016, pp. 40-59.

[17] [Online]. Available: https://jerseyfirstis.com/wp-content/uploads/2018/06/solar-panel-inspection.jpg.

[18] [Online]. Available: https://www.etechnog.com/2019/05/diode-used-solar-panel-relay.html.

[19] K. LEVENBERG, «A METHOD FOR THE SOLUTION OF CERTAIN NON-LINEAR PROBLEMS IN LEAST SQUARES,» *Quarterly of Applied Mathematics,* vol. 2, n. 2, pp. 164-168, 1944.

[20] D. W. Marquardt, «An Algorithm for Least-Squares Estimation of Nonlinear Parameters,» *Journal of the Society for Industrial and Applied Mathematics,* vol. 11, n. 2, pp. 431-441, 1963.

[21] G. Chicco, «Note sull'analisi e sull'ottimizzazione dei sistemi elettrici di distribuzione,» Politecnico di Torino, 2004.

[22] J. A. Nelder e R. Mead, «A simplex method for function minimization,» *The Computer Journal,* vol. 7, n. 4, pp. 308-313, 1965.

[23] G. Blaesser and D. Munro, “Guidelines for the Assessment of Photovoltaic Plants, Document C, Initial and Periodic Tests on PV Plants,” Office for Official Publications of the European Communities, Ispra, Italia, 1995.

[24] E. Durán, M. Piliougine, M. Sidrach-de-Cardona, J. Galán e J. Andújar, «Different methods to obtain the I–V curve of PV modules: A review,» in *2008 33rd IEEE Photovoltaic Specialists Conference*, San Diego, CA, USA, 2008.

[25] F. Spertino, J. Ahmad, A. Ciocia, P. Di Leo, A. F. Murtaza e M. Chiaberge, «Capacitor charging method for I–V curve tracer and MPPT in photovoltaic systems,» *Solar Energy,* vol. 119, pp. 461-473, 2015.

[26] B. García Domingo, «Análisis, caracterización y modelado del comportamiento en exterior de módulos de concentración fotovoltaica,» Universidad de Jaén, Tesis Doctoral, 2014.

[27] R. Núñez, C. Domínguez, S. Askins, M. Victoria, R. Herrero, I. Antón e G. Sala, «Determination of spectral variations by means of component cells useful for CPV rating and design,» *Progress in Photovoltaics,* vol. 24, n. 5, pp. 663-679, May 2016.

[28] Z. Stokes e A. Kaknevicius, «Reverse Current Protection in Load Switches,» Texas Instruments Inc., May 2016.

[29] S. Gulkowski, J. V. Muñoz Diez, J. Aguilera Tejero e G. Nofuentes, «Computational modeling and experimental analysis of heterojunction with intrinsic thin-layer photovoltaic module under different environmental conditions,» *Energy,* vol. 172, pp. 380-390, 2019.

[30] M. Norton, A. M. Gracia Amillo e R. Galleano, «Comparison of solar spectral irradiance measurements using the average photon energy parameter,» *Solar Energy,* vol. 120, pp. 337-344, 2015.

[31] F. Spertino, A. Ciocia, P. Di Leo, S. Fichera, G. Malgaroli e . A. Ratclif, «Toward the Complete Self-Sufficiency of an nZEBs Microgrid by Photovoltaic Generators and Heat Pumps: Methods and Applications,» *IEEE Transactions On Industry Applications,* vol. 55, n. 6, pp. 7028-7040, Nov.-Dec. 2019.

[32] F. Ghani, M. Duke e J. Carson, «Numerical calculation of series and shunt resistance of a photovoltaic cell using the Lambert W-function: Experimental evaluation,» *Solar Energy,* vol. 87, pp. 246-253, January 2013.

[33] R. Abbassi, A. Abbassi, M. Jemli e S. Chebbi, «Identification of unknown parameters of solar cell models: A comprehensive overview of available

approaches,» *Renewable and Sustainable Energy Reviews,* vol. 90, pp. 453-474, July 2018.

[34] R. Majdoul, E. Abdelmounim, M. Aboulfatah, A. w. Touati, A. Moutabir e A. Abouloifa, «Combined analytical and numerical approach to determine the four parameters of the photovoltaic cells models,» in *2015 International Conference on Electrical and Information Technologies (ICEIT)*, Marrakech, 2015.

[35] A. K. Tossa, Y. Soro, Y. Azoumah e D. Yamegueu, «A new approach to estimate the performance and energy productivity of photovoltaic modules in real operating conditions,» *Solar Energy,* vol. 110, pp. 543-560, 2014.

[36] M. Wolf e H. Rauschenbach, «Series resistance effects on solar cell measurements,» *Advanced Energy Conversion,* vol. 3, n. 2, pp. 455-479, 1963.

[37] C. R. Osterwald, «Translation of device performance measurements to reference conditions,» *Solar Cells,* vol. 18, n. 3-4, pp. 269-279, September–October 1985.

[38] M. Torres-Ramírez, G. Nofuentes, J. Silva, S. Silvestre e J. Muñoz, «Study on analytical modelling approaches to the performance of thin film PV modules in sunny inland climates,» *Energy,* vol. 73, pp. 731-740, 2014.

[39] M. Piliougine, J. Carretero, L. Mora-López e M. Sidrach-de-Cardona, «Experimental system for current–voltage curvemeasurement of photovoltaic modules underoutdoor conditions,» *Prog. Photovolt: Res. Appl.,* vol. 19, pp. 591-602, 2011.

[40] D. Fébba, R. Rubinger, A. Oliveira e E. Bortoni, «Impacts of temperature and irradiance on polycrystalline silicon solar cells parameters,» *Solar Energy,* vol. 174, pp. 628-639, 2018.